Metal-clad waveguide sensors

Skivesen, Nina

Publication date:
2005

Document Version
Publisher's PDF, also known as Version of record

Risø-PhD-15(EN)

Metal-Clad Waveguide Sensors

Nina Skivesen

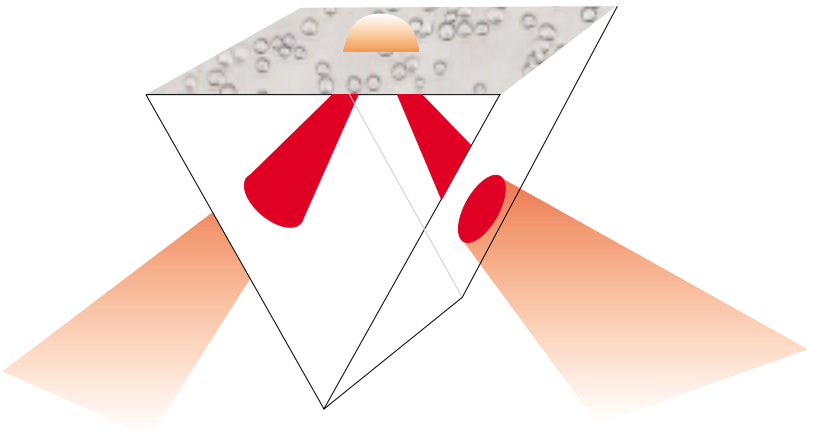

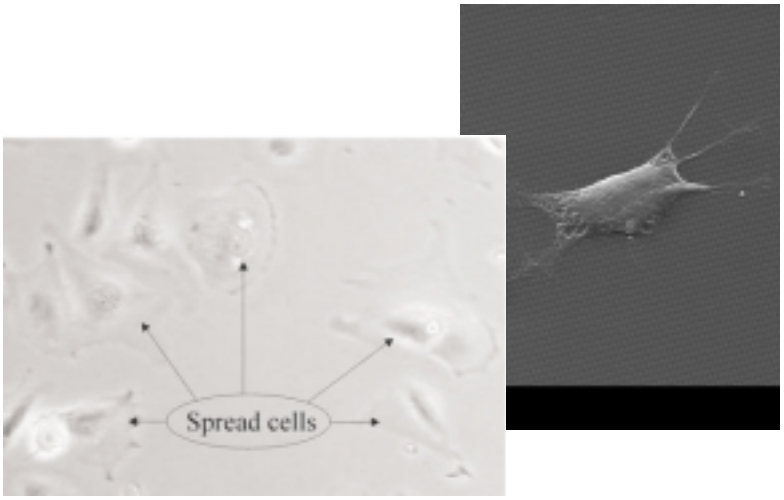

Risø National Laboratory
Roskilde
Denmark
September 2005

Author: Nina Skivesen
Title: Metal-Clad Waveguide Sensors
Department: OPL

This thesis is submitted in partial fulfillment of the requirements for the Ph.D. degree at Faculty of Science, University of Copenhagen.

Abstract (max. 2000 char.):
This work concerns planar optical waveguide sensors for biosensing applications, with the focus on deep-probe sensing for micron-scale biological objects like bacteria and whole cells. In the last two decades planar metal-clad waveguides have been briefly introduced in the literature applied for various biosensing applications, however a thorough study of the sensor configurations has not been presented, but is the main subject of this thesis.

Optical sensors are generally well suited for bio-sensing as they show high sensitivity and give an immediate response for minute changes in the refractive index of a sample. Due to the high sensitivity of optical bio-sensors direct detection of biological objects is possible. The majority of optical sensors presented in the literature and commercially available optical sensors are based on evanescent wave sensing, however most of these sensors can only detect substances in the close vicinity to the sensor surface limited to below 200 nm. Bacteria and whole cells with sizes of micron-scale exceed that range and thus sensors suitable for deep-probe sensing are important.

The present thesis deals with optical, planar waveguide sensors for deep-probe evanescent wave sensing with emphasis on detection of micron-scale biological objects. I have demonstrated reverse-symmetry operation using the simplest possible configuration, a freestanding glass plate acting as a multimode sensor [N. Skivesen et al, *Opt. Lett.* **28,** 2003]. Such a sensor has only been realized by Qi et al [Zm Qi et al, *Sens. Actuators B* **81**, 2002] before, however the sensing principle we present results in a broad detection range from gases to solid materials and is different from the principle suggested by Qi et al with a highly limited detection range.

Metal-clad waveguide sensors are suitable for deep-probe sensing and can be operated in two different modes. I have made a thorough optimization of the waveguide parameters of both MCWG-types in terms of sensitivity [N. Skivesen et al, *Sens. Actuators B* **106**, 2005] and [N. Skivesen et al, *Opt. Lett.* **30**, 2005]. Each of the sensor types have previously been realized by Salamon et al [Z. Salamon et al, *Biophys. J.* **73**, 1997] and Zourob et al [M. Zourob et al, *Sens. Actuators B* **90**, 2003] and presented for biosensing in connection with experiments, however no thorough study of the impact of the various parameters involved in the sensor configurations have been presented.

The studied sensor configurations have been fabricated and applied for refractive index measurements and cell-detection, thus this thesis also includes presentation and analysis of experimental setups, descriptions of fabrication processes and measurements with all three sensors, where single cell detection is shown by use of the metal-clad waveguide sensors.

Risø-PhD-15 (EN)
September 2005

ISBN 87-550-3467-5

Print: Pitney Bowes Management Services Denmark A/S, 2005

Contract no.:

Group's own reg. no.:
1705074-3

Sponsorship:
BIOP Graduate School,
Grant #643-01-0092.
Danish Technical Research council,
Grants #26-01-0211 and
#26-03-0272.

Cover :
Illustration of a metal-clad waveguide with incident and reflected light. A microscope picture of dead Hacat cells on a metal-clad waveguide is shown on the prism surface, the microscope image is also shown in Fig. 7.9(c).
Below: Microscope image of spreading fibroblast cells on a polystyrene surface with courtesy from Róbert Horváth and microscope image of a cell spreading on a nanostructured polymer surface with courtesy from the polymer department, Risø National Laboratory.

Pages: 109
Figures: 69
Tables: 2
References: 77

Risø National Laboratory
Information Service Department
P.O.Box 49
DK-4000 Roskilde
Denmark
Telephone +45 46774004
bibl@risoe.dk
Fax +45 46774013
www.risoe.dk

Dansk resume

Denne afhandling omhandler planare optiske sensorer til måling på prøver indeholdende biologiske objekter. Fokus er lagt på detecton af objekter med en størrelseorden af mikrometer indbefattende celler og bacterier. Indenfor de seneste 20 år er planare metal-belagte bølgeledere (metal-clad waveguides (MCWGs)) blevet introduceret i forbindelse med praktisk anvendelse af disse som sensorer til biologisk detection. Der er i den forbindelse ikke tidligere blevet præsenteret en dybgående analyse af konfigurationen af MCWGs. Hoved-formålet med denne afhandling er netop en dybgående analyse af denne sensorkonfiguration.

Generelt er optiske sensorer meget følsomme overfor en ændring af brydningsindekset af den prøve, der måles på, og det er muligt at måle selv små ændringer online. Den høje følsomhed gør netop, at optiske sensorer er anvendelige til detektion af biologiske objekter. Mange af de optiske sensorer, der løbende præsenteres i litteraturen og hvoraf nogle allerede findes på det kommercielle marked i dag, er baseret på at måle brydningsindekset af en prøve på sensorens overflade ved hjælp af et "evanescent" felt. Dette felt er begrænset i udbredelse i prøven til under 200 nm fra overfladen af sensoren. Idet celler og bakterier er i størrelsesorden af mikrometer, er de gængse evanescentfelt sensorer begrænset mht. detektion af disse, og derfor er sensorer, der kan detektere objekter som celler og bakterier interessante.

Undersøgelsen af MCWG sensorer tager udgangspunkt i en beskrivelse af planare dielektriske bølgeleder-sensorer omfattende sensorer med den gængse symmetri, hvor brydningsindekset af substratet for bølgeleder-filmen er højere end brydningindekset af prøven, der måles. Den nylig introducerede konfiguration af dielektrisk bølgeleder med omvendt symmetry, hvor brydningsindekset af substratet i bølgelederkonfigurationen er mindre end brydningsindekset af prøven præsenteres ligeledes. Denne sensor er netop udviklet med henblik på detection of objekter af størrelsen mikrometer. I forbindelse med beskrivelsen af dielectriske bølgeleder-sensorer har jeg undersøgt en multimode bølgeleder-sensor. Den består af en simpel glasplade og er anvendt til målinger af væskers brydningindeks. Både fabrikationen og den eksperimentelle opstilling til denne sensor er præsenteret.

Analysen af MCWG-sensorer omfatter to forskellige typer sensorer, en peak-type og en dip-type, hvor analysen er fokuseret på optimering af sensorerne til detektion af biologiske objekter af mikrometer-størrelse. Yderligere beskrives fabrikation af og målinger med begge sensorer, herunder er en simpel eksperiment opstilling, kaldet "retro-reflector"-princippet, blevet afprøvet og analyseret. Til vurdering af disse sensorers følsomhed er SPR-sensorer sideløbende blevet analyseret til sammenligning, da SPR-sensoren idag anvendes bredt indenfor biologisk detection.

Målinger udført med MCWG-sensorer har vist, at det er muligt at detektere en enkelt celle på sensorens overflade.

Fabrikationen af optiske sensorer er også et interessant emne, da en del sensor-konfigurationer involverer omfattende processer, hvilket kan være problematisk i forbindelse med kommerciel anvendelse. Fabrikationen af MCWG-sensorerne er forholdsvis simpel og en beskrivelse af fabrikationen er også inkluderet i denne afhandling.

Preface and acknowledgements

The study for the present thesis has been carried out at the Optics and Plasma Research Department (OPL) at Risø National Laboratory, Denmark in the period September 2002 to September 2005. During the study I was enrolled as a Ph.D. student at the Niels Bohr Institute (NBI) at Copenhagen University (KU), Denmark. The Ph.D. project was financed partly by the BIOP graduate school, Denmark, grant #643-01-0092 and the Danish Technical Research Council, grants #26-01-0211 and #26-03-0272.

The work was supervised by:

Dr. Henrik C. Pedersen, OPL, Risø National Laboratory, Dk.

Dr. Jan W. Thomsen, NBI, Copenhagen University, Dk.

It has been a pleasure to work in the group with Henrik C. Pedersen and dr. Róbert Horváth. I am very greatful for their invaluable help, guidance and their enthusiasm.

I would also like to express my gratitude to Jørgen Stubager and Bjarne Sass at Risø National Laboratory for their invaluable technical support in connection with my work in the clean room and for performing continuously changes in my experimental setup.

Six months of my Ph.D. period I spent in Spain at the biosensor group at IMM, CSIC, Tres Cantos, Madrid. I would like to thank everybody at IMM in Tres Cantos and especially the people in the biosensor group for their help in the laboratories but also for they kind and warm welcome both at work and in the spare time - besos por los todos. In that connection a very great thank to Laura Lechuga for giving me the opportunity to work at IMM and for arranging everything for my arrival.

My time at Risø has offered daily contact to helpful collegues in my own department but also to people in the polymer department, where I would like to thank Sidse Thinggård Pedersen for providing cells for my experiments. Especially I would like to thank Henrik Schiøtt Sørensen, who has been great company at the office and a guy with great patience - we have actually been able to share an office for three years - thanks for the talks, laughs and your eminent jokes.

Also I would like to thank friends and family for helping in the extend possible showing interest and encouragement.

Nina Skivesen
September 2005

List of publications

Refereed journal papers

Optical waveguide sensor for on-line monitoring of bacteria
R. Horváth, H.C. Pedersen, N. Skivesen, D. Selmeczi & N.B. Larsen
Opt. Lett. **28** (2003), pp. 1233-1235

Multimode reverse-symmetry waveguide sensor for broad-range refractometry
N. Skivesen, R. Horváth & H.C. Pedersen
Opt. Lett. **28** (2003), pp. 2473-2475

Measurement of guided light-mode intensity: An alternative waveguide sensing principle
R. Horváth, N. Skivesen & H.C. Pedersen
Appl. Phys. Lett. **84** (2004), pp. 4044-4046

Optimization of metal-clad waveguide sensors
N. Skivesen, R Horváth & H.C. Pedersen
Sens. Actuators B **106** (2005), pp. 668-676

Fabrication of reverse symmetry polymer waveguide sensor chips on nanoporous substrates using dip-floating
R. Horváth, H.C. Pedersen, N. Skivesen, C. Svanberg & N.B. Larsen
J. Micromech. adn Microeng. **15** (2005), pp.1260-1264

Peak-type and dip-type metal-clad waveguide sensing
N. Skivesen, R. Horváth & H.C. Pedersen
Opt. Lett. **30** (2005), pp. 1659-1661

Analytical and numerical study on grating depth effects in grating coupled waveguide sensors
R. Horváth, L.C. Wilcox, H.C. Pedersen, N. Skivesen, J.S. Hesthaven & P.M. Johansen
Appl. Phys. B **81** (2005), pp.65-73

Monitoring of living cell attachment and spreading using reverse symmetry waveguide sensing
R. Horváth, H.C. Pedersen, N. Skivesen, D. Selmeczi & N.B. Larsen
Appl. Phys. lett. **86** (2005), Art. No. 071101

Submitted paper

Deep-probe metal-clad waveguide sensing: Theory and experiments
N. Skivesen, R. Horváth, H.C. Pedersen, S. Thinggaard and N.B. Larsen
Sens. Actuators, October 2005

Bookchapter

Reverse Symmetry Waveguide for Optical Biosensing
Springer Ser Chem Sens Biosens
R. Horváth,N. Skivesen N, N.B. Larsen & H.C. Pedersen
Springer-Verlag, Berlin, Heidelberg (2005)

Conference contributions

Reverse-symmetry multimode waveguide sensor - for broad-range refractometry (oral)
Biomedical Optics '03, Lyngby, Denmark (September 2003)

Reverse-symmetry multimode waveguide sensor (poster)
Northern Optics, Espoo, Finland (June 2004)

Optimization of metal-clad waveguides (MCWGs) - for sensing purposes (oral)
Biomedical Optics '04, Lyngby, Denmark (November 2004)

Deep-probe biosensing using metal-clad waveguides (oral)
Cleo, Munich, Germany (June 2005)

Deep-probe biosensing using metal-clad waveguides (poster)
The 2nd International Graduate Summerschool Biophotonics '05, Ven, Sweden (June 2005)

Contents

Chapter 1

Introduction

Biosensor is a general term for a wide range of devices that measure the presence or concentration of biological molecules, biological structures, microorganisms, etc., by translating a biochemical interaction at the probe surface into a quantifiable physical signal.

The possible fields of application of biosensing are extensive, involving areas such as the medical industry for development of drugs, diagnostics at the local doctor and home medical tests. Online screening of water quality for both household and industrial use are other fields of applications of biosensing and environmental monitoring of both air and water measuring on waste water, the conditions in storage facilities (humidity) and other indoor facilities amongst a lot of other fields of application.

Today, infectious diseases cause 40% of all deaths worldwide (approximately 20 million deaths a year). Especially in many developing countries microbial diseases constitute the major causes of death.[1] Bacterial pathogens cause up to 91% of estimated 81 million food borne illnesses in the USA, especially bacterial pathogens (e.g. Escherichia coli (E.coli), Salmonella, Staphylococcus aureus, Campylobacter jejuni, Campylobacter coli and Bacillus cereus) are the cause of food borne illnesses and can easily contaminate both food and water. Unfortunately the occurrence of infections due to these pathogens do not seem to decrease.[2] Salmonella and E. coli O157:H7 are especially dangerous for humans and can cause death. Even a very low amount of bacterial pathogens can cause an infection e.g. a dose of no more than 10 E. coli O157:H7 or Salmonella bacteria can cause infections.[2]

Common bacterial infections like tonsillitis (inflammation of the throat) and inflammation of the urinary system result in more than 25 million calls at medical doctors every year in the USA alone.[3]

Bacterial pathogens can be food, water and air borne and thus careful control of bacterial pathogens is extremely important to both minimize the spreading of infectious diseases and rapid diagnostics of infections for better and faster treatment. Thus the important demands for a sensor for bacterial detection are high sensitivity and a fast response on the scale of minutes.

Currently, the most used technique for bacteria detection is still colony counts, where a sample is placed in optimal growth conditions in an agar-coated petri dish and is subsequently observed for bacterial growth. This method is very sensitive as a single cell will spread into a colony of cells, however the method is very slow as it typically takes 24 hours or more to obtain a result.

For medical diagnostics of inflammatory diseases a number of tests exist for indirect measurements of the presence of bacteria. These tests detect traces left in the sample due to bacterial activity. However these tests have limited sensitivity, no specificity for which bacteria are present in the sample and can only be used for infections where traces are present.

One principle for specific bacterial detection is gene based sensors where the best known principle is the polymerase chain reaction (PCR). Here, a specific gene sequence in the DNA molecule is recognized to determine the type and strain of the bacteria with high sensitivity however the sample processing time is lengthy (4 - 6 hours)[4] and the processing of the samples demands expertise in molecular biology.[5, 6]

Intensive research in developing biosensors for fast and sensitive detection has been conducted over several decades and has resulted in various techniques. Especially optical techniques have proven interesting for biosensing due to the possibility of rapid, direct (unlabeled) detection. The research in optical biosensors has resulted in a number of sensor devices which have been applied for biosensing and reported for detection of bacterial pathogens including monomode dielectric waveguide sensors,[7] surface plasmon resonance sensors,[8] the resonant mirror sensor[9] and various interferometers.[10] These sensors give rapid and sensitive detection, however some of the sensors are only suitable for sensitive measurements of objects on a size scale up to 100 nm like DNA, proteins and viruses while others require complicated and delicate fabrication steps, such as coating procedures, baking steps, etching, and various chemical or physical deposition steps.[11]–[17]

The aim of this thesis is to optimize optical, planar sensors for high sensitivity for biological objects of micron meter size for unlabelled detection and fast response and with potential to be implementable in a portable sensor system for fast, precise measurements. A sensor system for commercial use should furthermore be possible to be operated without extensive training in the use of the system or specific knowledge of molecular biology and be operated with sensors, which can be fabricated by a rather simple process. The emphasis of this work has been to conduct a systematic study of the sensors in order to optimize the sensor sensitivity and thus the aim has not been to fully develop a ready-to-use biosensor system. Potential sensors fulfilling these requirements are the *reverse-symmetry waveguide sensors* and *metal-clad waveguide sensors*.

The thesis is divided into 6 chapters starting in chapter 2 with a basic introduction to optical waveguides, biosensing and optical biosensor techniques. Based on this general introduction of optical biosensing the focus is aimed at optical sensors for deep-probe sensing.

In chapter 3 the reverse symmetry dielectric waveguide sensor is presented. Single mode operation of this sensor has been studied for optimization of various biosensor applications and the sensor has proven well suited for deep-probe sensing. Experiments with this sensor includes detection of both bacteria and whole cells with good results. However, the reverse symmetry waveguide can also be used in multimode operation for deep-probe sensing and this is the main subject of chapter 3, where I demonstrate reverse symmetry operation of the most simple waveguide configuration, a simple, free standing glass plate acting as a waveguide. A simple sensing principle is proposed for the sensor and demonstrated for RI measurements. The fabrication of the sensor is presented along with the experimental setup. Using the presented sensing principle results in that the sensor can be used as a refractometer for broad range absolute refractive index measurements.

Another interesting sensor configuration for deep-probe sensing is the metal-clad waveguide (MCWG). MCWGs can be operated in two modes and can be divided into dip-type MCWGs and peak-type MCWGs. In chapter 4 and 5 I present a thorough study of the two MCWGs for optimization of the waveguide parameters of both MCWG-types in terms of sensitivity. The dip-type MCWG is presented in chapter 4 and the peak-type MCWG in chapter 5. The MCWG sensors are evanescent wave sensors and for both sensors the sensing principle will be described and the influence of the various parameters in the waveguide configurations will be discussed in connection with optimum sensitivity and detection ranges of the sensors. A theoretical comparison with the SPR sensor is given as the SPR sensor is closely related to the MCWG sensors as they are all optical metal-clad sensors. Also, the implementation of the MCWG sensors in an experimental setup is discussed in chapter 5.

Experiments with the MCWGs have been performed and will be presented in chapter 6, where a simple experimental setup , the retro-reflector setup, is presented and analysed for the ability of precise measurements. The fabrication of the sensors is also presented and the sensors are applied for both RI measurements and cell-detection.

Concluding remarks on the sensors are given in chapter 7.

Chapter 2

Waveguide bio-sensors

In this chapter planar waveguides are introduced giving a detailed description of the basic properties of planar waveguides for later reference and an introduction to biosensing is given leading to a presentation of the use of planar waveguides for bio-sensing. Furthermore, a short description is given of the term biosensing and of a few commonly used optical biosensors in the literature.

2.1 Planar waveguides

Basically, a planar waveguide constitutes a three-layer dielectric structure of a substrate S, a waveguide film F and a cover medium C, see Fig. 2.1 for the basic waveguide configuration.

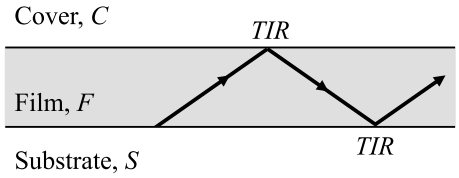

Figure 2.1. Basic waveguide structure with illustration of light guided in the waveguide film by total internal reflection (TIR) at the film boundaries.

The basic configuration consists of dielectric media with refractive indices (RIs), n_S, n_F and n_C for the substrate, film and cover medium, where $n_F > \{n_S, n_C\}$. The important feature of the dielectric waveguide is the possibility of light being guided in the film layer of the structure, illustrated in Fig. 2.1.

How is light guided in a planar waveguide?

In a planar dielectric waveguide light is guided in the waveguide film by total internal reflection (TIR) at the film/cover- and the film/substrate-boundary, respectively, see Fig. 2.2 for illustration of reflection at the film/cover-boundary.

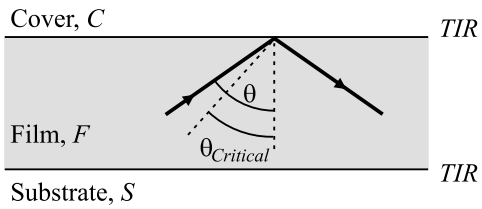

Figure 2.2. Light reflected by TIR at the film/cover-boundary when the propagation angle of the light, θ is above the critical angle, $\theta_{Critical}$.

Total internal reflection can only be achieved for light propagating in a medium with a RI higher than the RI of the adjacent medium and when the incident angle of the light on the boundary of the two media is higher than the critical angle, $\theta_{Critical}$, which is the angle where the light changes from being a normal propagating wave across the boundary to being totally internal reflected.

Thus, to achieve TIR in the waveguide film at both boundaries the waveguide film's RI should be higher than the RIs of the substrate and the cover and the propagation angle of the light θ should be above the highest critical angle of the two:

$$\begin{aligned} n_F &> \max\{ n_C, n_S\}, \\ \theta_{Critical} &= \sin^{-1}\left(\tfrac{\max\{ n_C, n_S\}}{n_F}\right). \end{aligned} \tag{2.1}$$

For the dielectric waveguide it is possible to excite a so-called waveguide mode at a given value of θ, the so-called waveguide mode angle or resonant angle θ_m, for which the light in the waveguide film is guided without loss.

When does a waveguide mode appear in the waveguide?

A waveguide mode arises when the reflected beams in the film achieve constructive interference upon experiencing both reflections. This condition may be derived by considering the guided light

as beams that zig-zag in the film, see Fig. 2.3 for illustration. The wave fronts with phase ϕ are illustrated with the lines orthogonal to the light path and are separated by 2π.

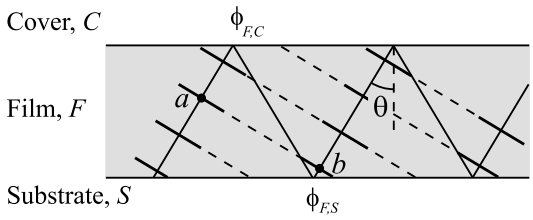

Figure 2.3. Constructive interference of the reflected beams in the waveguide film appears if the wave fronts at points a and b are in phase. The phase change of the reflected beams at the film boundaries are $\phi_{F,S}$ and $\phi_{F,C}$ and θ the angle of propagation.

Constructive interference between the guided beams exists if the wave fronts are in phase after reflection at the two boundaries, which is illustrated for the two wave fronts in points a and b in Fig. 2.3 and thus the total phase shift between point a and b should be an integral multiple of 2π to obtain a waveguide mode. The total phase shift between the two points comprises the change in phase due to the optical path difference between point a and b, $\phi_{\Delta S}$, and the phase shifts, $\phi_{F,S}$ and $\phi_{F,C}$ due to the reflections at the film boundaries. The criteria for a waveguide mode can thus be written as:

$$2\pi m = \phi_{\Delta S} + \phi_{F,S} + \phi_{F,C}, \tag{2.2}$$

where $m = 0, 1, 2...$ is the mode order.

The phase shift due to the travelled distance from point a to b depends primarily on the RI of the waveguide film and the film thickness d_F and is given by:[18]

$$\phi_{\Delta S} = 2d_F k\sqrt{n_F^2 - N^2}, \tag{2.3}$$

where $k = 2\pi/\lambda$ is the wave number in vacuum and N is the effective refractive index given by $n_F \sin\theta$. The phase shifts due to TIR at the two boundaries are given by:[18, 19]

$$\phi_{F,S} = -2\arctan\left[\left(\frac{n_F}{n_S}\right)^{2\rho}\sqrt{\frac{N^2 - n_S^2}{n_F^2 - N^2}}\right], \tag{2.4}$$

$$\phi_{F,C} = -2\arctan\left[\left(\frac{n_F}{n_C}\right)^{2\rho}\sqrt{\frac{N^2 - n_C^2}{n_F^2 - N^2}}\right], \tag{2.5}$$

where $\rho = 0, 1$ represents the TE and TM polarized case, respectively.

Of the parameters in the mode equation only N is unknown, which is a normalized wave vector component along x given by k_x/k (see Fig. 2.5 for axis defintion). The term effective refractive index arises because the phase velocity along x in the waveguide is $v = c/N$. From the mode equation Eq. (2.2) the solutions N_m can now be calculated for a given waveguide configuration. In Fig. 2.4 N_m is calculated vs. film thickness for a waveguide structure comprising a glass substrate, a polystyrene waveguide film and water for the cover medium using both TE and TM polarized light and for $m = 0 - 3$.

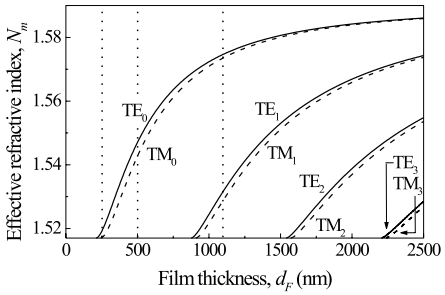

Figure 2.4. Calculated N_m vs. film thickness for $m = 0 - 3$ for TE and TM polarized light. The used RIs are: n_S = 1.517, n_F = 1.59 and n_C = 1.33. The dotted lines represent d_F = 250 nm, 500 nm and 1100 nm for later reference.

From Fig. 2.4 it is seen that N_m for this waveguide configuration has a value in the range n_S to n_F starting at n_S and increasing towards n_F for increasing film thickness. Generally, the film thickness at which N_m = max$\{n_C, n_S\}$ is the cutoff film thickness for the various modes.

For a given waveguide configuration the film has to have a certain thickness for a waveguide mode to exist and, depending on the polarization of the light, this thickness at which the waveguide mode starts to exist is referred to as the cutoff film thickness. Gradually increasing the film thickness from the cutoff film thickness results in one to more supported waveguide modes of the same polarization of the light, thus a single mode waveguide describes a waveguide in which one waveguide mode exists and for two or more supported waveguide modes of the same polarization the waveguide is a multimode waveguide. For a multimode waveguide several cutoff thicknesses exists - one for each waveguide mode, these thicknesses are referred to as the cutoff film thickness for the waveguide mode of mode order m. For the examples in in Fig. 2.4 these cutoff thicknesses are approximately 250 nm, 800 nm and 1600 nm for the 0$^{\text{th}}$, 1$^{\text{st}}$ and 2$^{\text{nd}}$ order modes, respectively.

Can the cutoff film thickness be calculated?

Based on the findings above, the cutoff film thickness for a given mode m can be calculated from Eqs. (2.2 - 2.5) by setting N = max$\{n_C, n_S\}$:

$$d_{Cutoff} = \frac{1}{k\left(n_F^2 - n_{max}^2\right)^{0.5}} \left(\tan^{-1} \left[\left(\frac{n_F}{n_{min}} \right)^{2\rho} \left(\frac{n_{max}^2 - n_{min}^2}{n_F^2 - n_{max}^2} \right)^{0.5} \right] + m\pi \right), \qquad (2.6)$$

where n_{min} = min$\{n_C, n_S\}$ and n_{max} = max$\{n_C, n_S\}$.

Can the profile of the electromagnetic field of the different mode orders be calculated?

The mode order of a waveguide mode determines the electromagnetic field in the waveguide. The profile of the electromagnetic field in the waveguide can be calculated from Maxwell's equations and the boundary conditions.

In Fig. 2.5 the electromagnetic fields in the waveguide layers are represented by plane waves, where A_I and B_I, (I = S, F, C) are the amplitudes of the up- and down-going waves, respectively in the individual media.

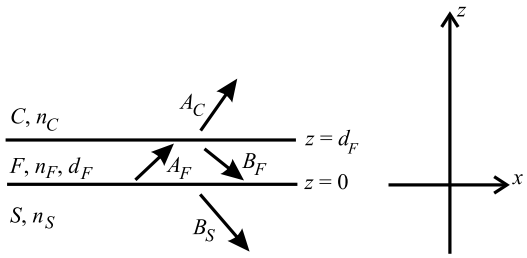

Figure 2.5. The electromagnetic field in a three-layered structure with a waveguide film of thickness d_F.

The eigenmodes of the three-layer (substrate-film-cover) structure can be obtained by solving Maxwell's equations for the structure initially assuming that the waveguide structure is left alone without any field incident from the outside, which is a usual procedure to identify the eigenmodes of a system. The solutions are obtained by using the solution ansatz Ω for the electromagnetic field based on the fields illustrated in Fig. 2.5:

$$\Omega = \left[\begin{array}{ll} B_S \exp[-ik_{z,S}z] \exp[ik_x x - i\omega t)] & \text{(in the substrate)} \\ (A_F \exp[ik_{z,F}z] + B_F \exp[-ik_{z,F}z]) \exp[ik_x x - i\omega t)] & \text{(in the film)} \\ A_C \exp[ik_{z,C}z] \exp[ik_x x - i\omega t)] & \text{(in the cover)} \end{array} \right], \qquad (2.7)$$

$$k_{z,I} = k\sqrt{n_I^2 - N^2},$$

where Ω represents the E-field for TE-polarized light and the H-field for TM-polarized light, k_x is the x-component of the wave vector and $k_{z,I}$ is the wave vector component along z in medium I.

Now, assuming non-magnetic media with permeability $\mu = 1$ and applying the boundary conditions stating that, (i) Ω and $\partial_z\Omega$ are continuous across the two boundaries for TE polarized light and (ii) Ω and $(n^{-2})\partial_z\Omega$ are continuous across the two boundaries for TM polarized light, it is possible for each polarization to obtain four equations relating the four amplitudes in Eq. (2.7). These four equations can be written in the form:

$$\mathbf{A}_\rho \psi = \mathbf{0}, \tag{2.8}$$

where ψ = (B_S, A_F, B_F, A_C) and $\mathbf{A}_\rho$ is given by:

$$\mathbf{A}_\rho = \begin{bmatrix} 1 & -1 & -1 & 0 \\ 0 & -\exp[ik_{z,F}d_F] & -\exp[-ik_{z,F}d_F] & \exp[ik_{z,C}d_F] \\ \frac{k_{z,S}}{n_S^{2\rho}} & \frac{k_{z,F}}{n_F^{2\rho}} & -\frac{k_{z,F}}{n_F^{2\rho}} & 0 \\ 0 & -\frac{k_{z,F}}{n_F^{2\rho}}\exp[ik_{z,F}d_F] & \frac{k_{z,F}}{n_F^{2\rho}}\exp[-ik_{z,F}d_F] & \frac{k_{z,C}}{n_C^{2\rho}}\exp[ik_{z,C}d_F] \end{bmatrix}, \tag{2.9}$$

In order to get non-trivial solutions the determinant of $\mathbf{A}_\rho$ needs to be zero, which leads to an equation exactly identical to the mode equation found from the ray-tracing approach, Eqs. (2.2-2.5).

The mode profile of a waveguide mode for a waveguide structure with a given d_F and the corresponding N_m calculated from Eq. (2.2) (shown in Fig. 2.4) can now be calculated from Eq. (2.8) by assuming one of the field amplitudes known, e.g. $A_F = 1$:

$$\begin{bmatrix} 1 & -1 & 0 \\ 0 & -\exp[-ik_{z,F}d_F] & \exp[ik_{z,C}d_F] \\ \frac{k_{z,S}}{n_S^{2\rho}} & -\frac{k_{z,F}}{n_F^{2\rho}} & 0 \end{bmatrix} \begin{bmatrix} B_S \\ B_F \\ A_C \end{bmatrix} = \begin{bmatrix} 1 \\ \exp[ik_{z,F}d_F] \\ -\frac{k_{z,F}}{n_F^{2\rho}} \end{bmatrix} \rightarrow$$

$$\begin{bmatrix} B_S \\ B_F \\ A_C \end{bmatrix} = \begin{bmatrix} \frac{k_{z,F}n_S^{2\rho}}{k_{z,F}n_S^{2\rho} - k_{z,S}n_F^{2\rho}} & 0 & \frac{n_F^{2\rho}n_S^{2\rho}}{k_{z,S}n_F^{2\rho} - k_{z,F}n_S^{2\rho}} \\ \frac{k_{z,S}n_F^{2\rho}}{k_{z,F}n_S^{2\rho} - k_{z,S}n_F^{2\rho}} & 0 & \frac{n_F^{2\rho}n_S^{2\rho}}{k_{z,S}n_F^{2\rho} - k_{z,F}n_S^{2\rho}} \\ -\frac{k_{z,S}n_F^{2\rho}\exp[-id_F(k_{z,C}+k_{z,F})]}{k_{z,S}n_F^{2\rho} - k_{z,F}n_S^{2\rho}} & \exp[-id_F k_{z,C}] & \frac{n_F^{2\rho}n_S^{2\rho}\exp[-id_F(k_{z,C}+k_{z,F})]}{k_{z,S}n_F^{2\rho} - k_{z,F}n_S^{2\rho}} \end{bmatrix} \times$$

$$\begin{bmatrix} 1 \\ \exp[-ik_{z,F}d_F] \\ -\frac{k_{z,F}}{n_F^{2\rho}} \end{bmatrix}. \tag{2.10}$$

In Fig. 2.6 the mode profiles for TM-polarized light with λ = 632.8 nm are calculated for waveguides with the following film thicknesses d_F and mode orders m: (a) d_F = 250 nm, $m = 0$, (b) d_F = 500 nm, $m = 0$ and (c) d_F = 1100 nm, m = {0, 1} for N_m calculated from Eq. (2.2).

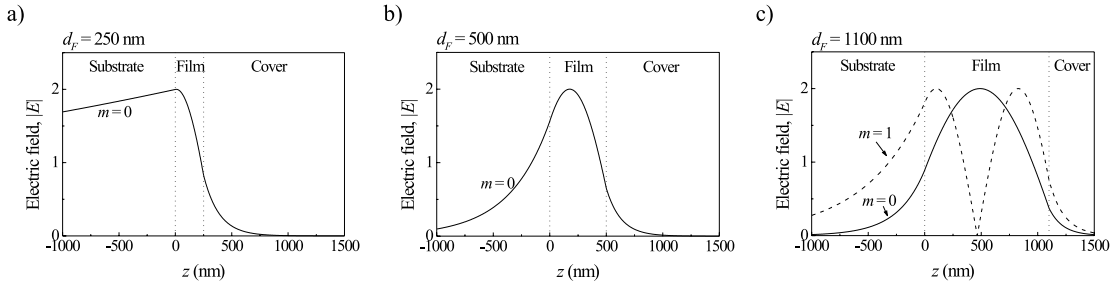

Figure 2.6. Calculated mode profiles of the electromagnetic field in a waveguide. The mode profiles are shown for three different film thicknesses, d_F = 250 nm (a), d_F = 500 nm (b) and d_F = 1100 nm (c) and are calculated for TM-polarized light with a wavelength λ = 632.8 nm. The used RIs are: n_S = 1.517, n_F = 1.59, n_C = 1.33.

From Figs. 2.6(a)-(c) it is seen that the mode profiles for all three configurations are asymmetric with evanescent fields extending into the cover and substrate of which the evanescent field in the substrate is larger than the evanescent field in the cover medium. This is due to the normal symmetry configuration of the waveguide configuration i.e. $n_S > n_C$.

The asymmetry is pronounced for mode profiles for waveguide configurations with a film thickness just above d_{Cutoff} (d_F = 250, $m = 0$ and d_F = 1100, $m = 1$) for which $N_m \simeq n_S$. For increasing film thickness for a given mode the asymmetry of the mode profile becomes less pronounced and the penetration depth of the evanescent field in both the cover and substrate is decreased. The mode profiles for the TE-polarized case show the same features.

From Eq. (2.2) the penetration depths of the evanescent field in the cover, $d_{P,C} = Im[k_{z,C}^{-1}]$ and in the substrate $d_{P,S} = Im[k_{z,S}^{-1}]$ are calculated in Fig. 2.7 for different mode orders vs. film thickness.

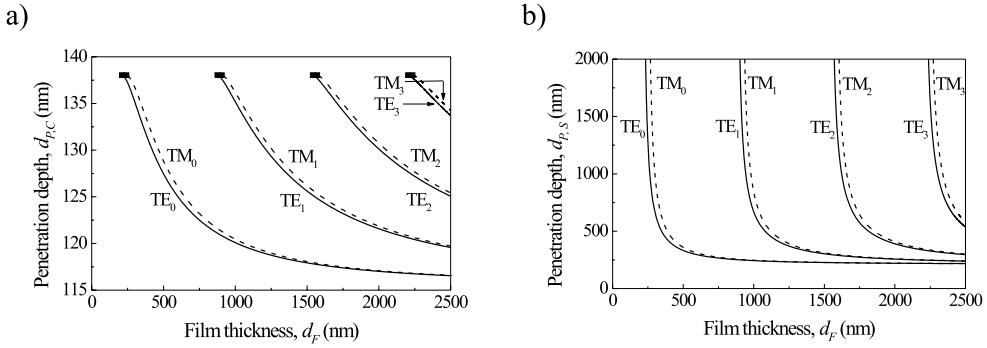

Figure 2.7. Calculated penetration depths in (a) the cover $d_{P,C}$ and (b) the substrate $d_{P,S}$ vs. film thickness for $m = 0 - 3$ for TE and TM polarized light. The used RIs are: n_S = 1.517, n_F = 1.59 and n_C = 1.33. The cutoff film thicknesses for the waveguide modes are illustrated by the squares.

From Fig. 2.7 it is seen that the penetration depths $d_{P,C}$ and $d_{P,S}$ for a given waveguide mode decreases with increasing film thickness, which is also seen from the mode profiles in Fig. 2.6. The penetration depth in the cover is limited to a finite value at cutoff film thickness (squares) with the same maximum penetration depth of 138 nm for all modes. Contrary to $d_{P,C}$, the substrate penetration depth $d_{P,S}$ is infinite at cutoff film thickness but decreases fast to a few hundred nm with increasing d_F and $d_{P,S}$ approaces the value of $d_{P,C}$. However, $d_{P,S}$ will always be higher than $d_{P,C}$ when $n_S > n_C$.

When does the evanescent field exist?

An evanescent field arises when light is guided by TIR which can only be obtained in a medium surrounded by lower RI media. The evanescent field arises in the media with the low RI, hence for the dielectric waveguide an evanescent field arises in both the cover medium and in the substrate, as seen from Figs. 2.6 and 2.7. The evanescent field is exponentially decreasing away from the boundary at which it arises, and the greatest penetration depth is obtained at the critical angle of TIR, as this is the angle at which the light transforms from a normally propagating wave in the adjacent medium to an evanescent field. The critical angle is determined by the adjacent medium to the waveguide film with the highest RI and thus the greatest penetration depth is obtained in that medium.

The fact that the guided electromagnetic field extends into the cover and substrate of the waveguide structure makes the waveguide useful for sensing purposes which we will see in the next section.

2.2 Waveguide sensors

The planar waveguide sensor is basically a refractometer measuring the RI of a medium. In its basic form the sensor constitutes a dielectric three layer planar waveguide, illustrated in Fig. 2.1, where it is possible to change the cover medium for example from one aqueous solution to another.

A basic planar waveguide was introduced for the first time for sensing purposes by Tiefenthaler and Lukosz[20] who applied it as a humidity and gas sensor by detecting a change in the RI of the cover medium. The waveguide sensor is along with other optical sensors referred to as evanescent field sensors due to the evanescent wave extending into the medium whose RI is to be measured.

From the calculated mode profiles in Fig. 2.6 it is seen that the evanescent field extends into the cover medium and from the mode equation, Eq. (2.2) the basic mechanism of the sensing can be explained. Considering Eq. (2.5) for the phase shift of the reflected light at the film/cover interface it is seen, that a given value of n_C influences the phase shift, thus, for a change in n_C the phase shift of the optical path length $\phi_{\Delta S}$ has to change in order to compensate for the change in $\phi_{F,C}$ and thereby maintain a waveguide mode. Hence, the angle of incidence for which a waveguide mode is excited, θ_m, will change. However, the evanescent field in the cover medium is limited to a given penetration depth and thus only changes in the cover medium occuring within the evanescent field influences $\phi_{F,C}$. In the case of an inhomogenous cover, where several thin layers are stacked on the sensor surface, only the layers in the vicinity of the sensor surface are sensed by the evanescent field and thus contributes to the RI of the cover medium and influences $\phi_{F,C}$.

What is the sensing principle?

The basic sensing principle of the planar dielectric waveguide sensor is to measure changes in N_m due to changes in n_C and the principle is illustrated in Fig. 2.8. Light can be coupled into the waveguide at the end facet of the waveguide film over a range of angles, α, and be guided in the film by TIR at the film/cover- and the film/substrate-boundaries at a range of angles θ, illustrated in Fig. 2.8(a). The light is coupled out of the waveguide at the other end facet of the film where the intensity is measured by a detector. The measured spectrum of intensity vs. angle is referred

to as a sensorgram. The sensorgram can either be shown as intensity vs. angle or N as these are related by $N = n_F \sin\theta$.

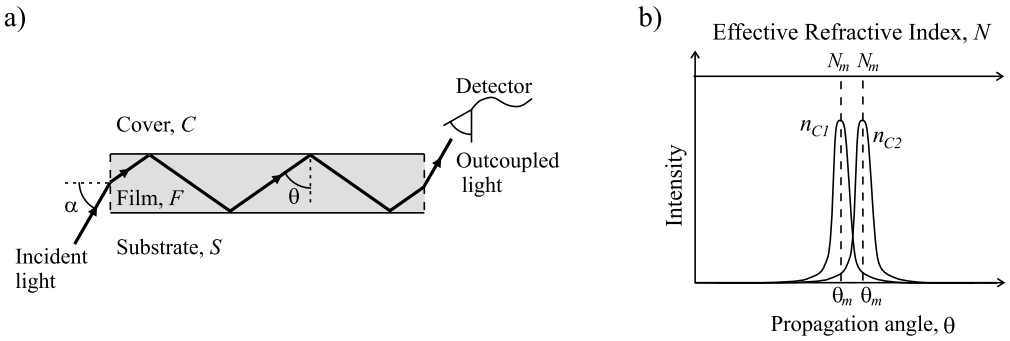

Figure 2.8. Basic sensing principle. Operation of the waveguide sensor (a) where light incident on the film end-face at the angle α is guided in the waveguide by TIR at the film/cover and film/substrate-boundaries at the propagation angle of the light θ and the intensity of the guided light is measured by a detector. Illustration of sensorgrams (b) for cover RIs n_{C1} and n_{C2}.

At the waveguide mode angle θ_m corresponding to N_m a waveguide mode is excited in the waveguide which gives rise to a peak in intensity in the measured sensorgram and a change in n_C results in a change of N_m and thus in the waveguide mode angle. The basic sensing principle is to measure the change in the position of the peak in intensity, illustrated in Fig. 2.8(b) for a change in cover RI from n_{C1} to n_{C2}.

How sensitive is the waveguide sensor?

From the mode equation Eq. (2.2) the sensitivity for changes in the RI of the cover medium, $\partial N_m/\partial n_C$ can be derived as:[19]

$$\frac{\partial N_m}{\partial n_C} = \left[\frac{n_C}{N}\frac{n_F^2 - N_m^2}{n_F^2 - n_C^2}\frac{d_C}{d_S + d_F + d_C}\left(2\frac{N_m^2}{n_C^2} - 1\right)\right], \tag{2.11}$$

where d_S and d_C are referred to as the so-called effective thicknesses of the substrate and the cover, respectively.[21] and are given by:

$$d_S = \frac{1-\rho}{k(N_m^2 - n_S^2)^{1/2}} + \frac{\rho}{\left(\left(\frac{N_m}{n_F}\right)^2 + \left(\frac{N_m}{n_S}\right)^2 - 1\right)\left(k(N_m^2 - n_S^2)^{1/2}\right)}, \tag{2.12}$$

$$d_C = \frac{1-\rho}{k(N_m^2 - n_C^2)^{1/2}} + \frac{\rho}{\left(\left(\frac{N_m}{n_F}\right)^2 + \left(\frac{N_m}{n_C}\right)^2 - 1\right)\left(k(N_m^2 - n_C^2)^{1/2}\right)}. \tag{2.13}$$

The terms d_S and d_C express the equivalent optical path length in cover and substrate, respectively that would have resulted in phase shifts equal to $\phi_{F,S}$ and $\phi_{F,C}$. Thus, alternatively the mode equation could be described by the phase shift of the total optical path length: $2m\pi = \phi_{\Delta S} + \phi_{d_S} + \phi_{d_C}$, where ϕ_{d_S} and ϕ_{d_C} are the phase shifts due to the optical path lengths d_S and d_C.

The cover RI sensitivity is calculated vs. film thickness in Fig. 2.9 for $m = 0 - 3$ for both TE and TM polarized light.

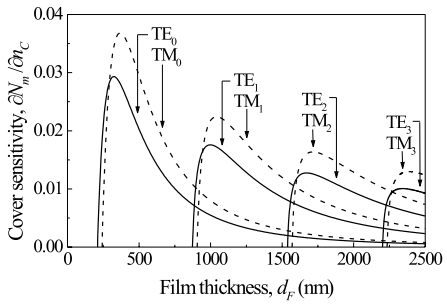

Figure 2.9. Calculated $\partial N_m/\partial n_C$ vs. film thickness for $m = 0 - 3$ for TE and TM polarized light. The used RIs are: n_S = 1.517, n_F = 1.59, n_C = 1.33.

It is seen in Fig. 2.9 that an optimum film thickness exists for the optimum cover RI sensitivity obtained with the lowest order waveguide mode and for TM polarized light for a film thickness just above cutoff film thickness. From the modeprofiles in Fig. 2.6 it is seen that in the case of a film thickness just above cutoff the evanescent field in the substrate is very large compared to the field on the cover, resulting in a very low influence of n_C on N_m and thus the cover RI sensitivity is low at cutoff film thickness. Increasing the film thickness results in a more symmetric mode profile of the electromagnetic field resulting in an increased influence of n_C on N_m and thus an increase in the cover RI sensitivity. However, it is also seen that for increased film thickness the field becomes more confined in the film and the evanescent fields in both the cover and substrate decrease with a decreased influence of both n_C and n_S on N_m and thus a decrease in the cover RI sensitivity. Thus, the optimum cover RI sensitivity is found at a film thickness where the mode profile of the field becomes more symmetric but for a film thickness for which, a relatively large part of the field still extends into the cover medium.

What is bio-sensing?

The term bio-sensing describes the process of detecting the presence or the concentration of biological objects ranging in size from nanometers to micrometers such as DNA, proteins, lipid bilayers, viruses, bacteria and whole cells. Also, bio-sensing can include measurements on the interactions of biological objects with a surface or other analytes.

For bio-sensing the detection of an analyte should preferably be conducted as specific and labelfree detection. Specific detection means that for a given sample it should be possible to measure one specific analyte, e.g. a water or urine sample contains a number of bacterial pathogens of different types and stains of which some are harmless and not interesting to detect.

For biosensing the analytes to be detected are often contained in an aqueous solution e.g. water, urine or blood. The sample is injected into a cuvette ensuring contact with the sensor surface either as still or flow measurements. For specific detection the surface is coated with a biological affinity layer to which the biological object to be measured (sample analyte) binds, see Fig. 2.10 for illustration. The cuvette is subsequently flushed with a sterile solution to rinse the sensor surface to ensure that only the analyte to be detected is present. This process adds a layer to the structure of the sensor, an adlayer. The affinity can be antibodies, antigens, a dextran layer etc. depending on which analytes are to be detected.

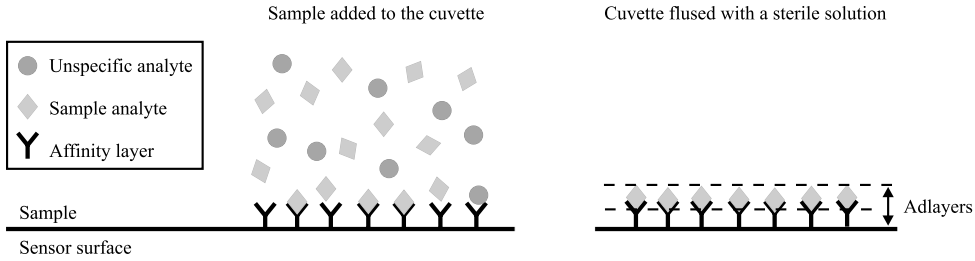

Figure 2.10. Formation of an adlayer on a sensor surface. The surface is coated with a specific affinity layer to which the sample analytes bind. The sample is applied to the cuvette and subsequently rinsed leaving an adlayer of specific analytes on the sensor surface.

Labelling of the sample analyte is a method for enhancing the signal from the analyte to ensure specific measurements or to ensure both specific detection and amplification of the signal from the specific analyte. The basic method for labelling is to bind a nanoparticle to a capture agent, which is similar to the agents of the affinity layer and thus, binds to the sample analyte. A solution containing the labelled capture agents is either mixed into the sample before applying the sample to the sensor or after the sample analytes have bound to the surface resulting in a sandwich-structure of the affinity layer, sample analytes and labelled capture agents on the sensor surface, see Fig. 2.11.

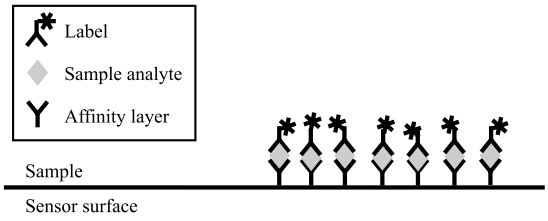

Figure 2.11. Formation of an adlayer on a sensor surface with labelled sample analytes.

The nanoparticles used as labels can for example be fluorescent and by exciting the particles an enhanced signal from the bound analytes cen be obtained. However, labelling requires an additional step in the detection procedure and adds time and additional costs to the measurements, thus label-free detection are advantageous if the sensing technique is sufficiently sensitive.

In general, optical bio-sensors have proven useful for label-free detection and for more than two decades several optical bio-sensors exploiting an evanescent field for sensing have appeared in the literature[20, 22]–[29] as they are able to detect minute changes in the RI close to the sensor surface caused by a change in the solution RI or by biological objects immobilized on the sensor surface as an adlayer.

The evanescent field bio-sensors introduced in the literature have proven to be a highly sensitive tool for interactions in the close vicinity of the sensor surface, but they generally have a limited penetration depth of the evanescent field in the cover of 100-150 nm and thus are mostly suitable for detection of interactions of small substances like viruses (10-100 nm), proteins (1-10 nm) and DNA at the sensor surface. For detection of interactions involving larger substances like bacterial cells ($0.5 - 5\mu$m) and eukaryotic cells ($5 - 50\mu$m) or interactions taking place at a given distance from the sensor surface the conventional evanescent field sensors reach a limit in sensitivity due to the limited penetration depth. In Fig. 2.12 adlayers of proteins, bacteria and eukaryotic cells on the sensor surface are illustrated with an evanescent field of (a) 100 nm and (b) 1 μm, respectively.

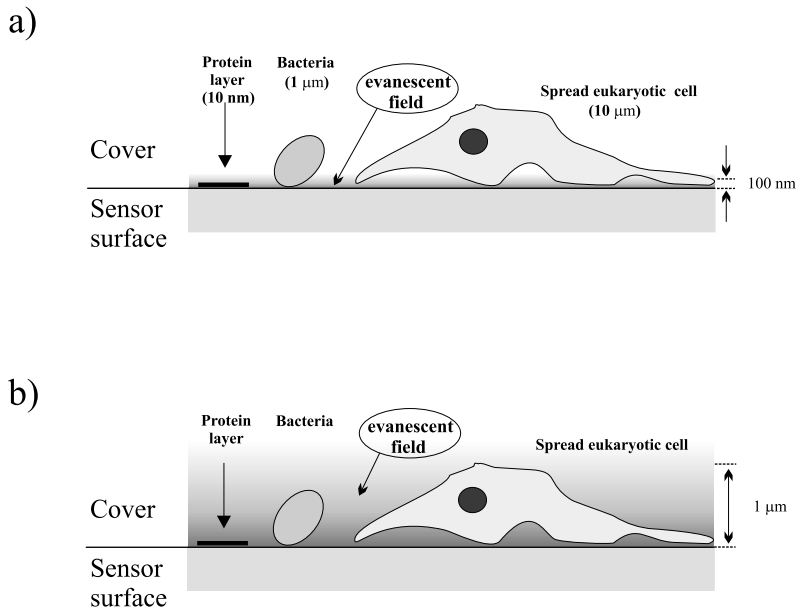

Figure 2.12. Illustration of the problem with a limited evanescent field of the conventional evanescent field sensors of 100 nm (a) and evanescent field that would increase the sensitivity for micronscale biological objects (b).

An increase of the evanescent field in the cover would expand the field of application of the bio-sensors to include sensitive detection of bacteria and eukaryotic cells. Especially detection of eukaryotic cells is currently limited with evanescent field sensors not only due to their size but also because they typically leave an aqueous gap between the cell membrane and the sensor surface,[30] and this gap thus does not contribute to a change in the sensed RI.

What is an optical bio-sensor?

In general, optical biosensors include all sensors for biosensing that uses light for probing of a biologial interaction and returns a quantifiable optical signal. A few well-proven techniques for label-free detection are briefly described here.

The waveguide sensor described in this chapter was first introduced for sensing by W. Lukosz and K. Tiefenthaler[20, 31] and since then a variety of designs have been presented in the literature for optimization of the sensitivity and in- and outcoupling of the light.[11, 15, 19, 25, 26, 32, 33] But the basic sensing principle is the same for all these sensors; the RI of the cover medium is sensed by the evanescent field extending into the cover medium contributing to the effective RI of the waveguide which is the parameter to be returned as the optical signal from the sensor.

A commercial system, the *OWLs 110 sensor system* based on waveguide sensors, has been developed by MicroVacuum.Ltd (Hungary)[34]. The sensor system is based on grating coupled dielectric waveguides and can be applied as an immunosensor where the surface has a monomolecular chemoresponsive coating, which consists of immobilized antibody molecules, that bind the corresponding antigen molecules. The sensor also exists as a chemosensor where the sensor surface is coated with a typically 0.1-1 mm thick chemoresponsive layer whose refractive index is changed by binding the analyte molecules.

The SPR sensor[35] comprises a three layer planar structure a substrate, a metal cladding and a cover medium whose RI is to be measured. This sensor is also an evanescent field sensor that measures the RI of the cover medium. The sensor is operated by illuminating the structure through the substrate over a range of angles and measuring the reflected light. At a given angle the incident light can excite a surface plasmon at the metal/cover interface resulting in an evanescent electromagnetic field that extends into the metal and the cover medium from the interface. The sensorgram from the SPR sensor shows the reflectance vs. angle and a dip appears in the reflectance at the angle for which the surface plasmon is excited. The SPR sensor is widely used and has been applied as a gas, humidity and chemical sensor,[36, 37] used for surface characterization,[38] and for sensing of biological adlayers.[39, 40]

The *Biacore* sensor system is a commercial system based on the SPR-sensor developed for characterization of proteins in terms of their specificity of interaction with other molecules, the rates at which they interact (binding and dissociation), and their affinity (how tightly they bind to another molecule).[41]

The resonant mirror sensor[22, 23] is yet another evanescent field sensor and comprises a planar structure on top of a prism. A low RI material ~ 1 μm thick is deposited onto the prism and on top of this another but thinner layer of high RI dielectric material is deposited $\sim$ 100 nm thick, this layer interfaces a cover medium, whose RI is to be measured. The structure is illuminated through the prism over a range of angles and the phase of the reflected light is measured. At certain angles light is coupled into the high RI material film where it undergoes multiple total internal reflections at the film/cover interface resulting in an evanescent field arising at this interface extending up to a few hundred nanometers into the cover medium. The total internal reflections at the film/cover interface adds a phase shift to the reflected light at the resonant angle, which changes with the cover mediums RI. Thus the sensing principle of the resonant mirror sensor resembles that of the waveguide sensor. However, instead of measuring the intensity peak the measured sensorgram from this sensor is the phase of the reflected light vs. angle. The resonant mirror sensor was applied for bacterial detection by Watts et al[9] for detection of S. aureus cells and for detection of other biological objects by Goddard et al.[42]

The anti-resonant reflecting optical waveguide (arrow)[43] is a planar layered structure where the sample RI is measured by light propagating in the sample. The structure of the arrow sensor varies according to the different groups working on this structure[44] but generally includes more layers than both the waveguide sensor, the resonant mirror sensor and the SPR sensor with five to seven layers, a substrate, 2nd and 1st cladding layer, a core layer which comprises a channel for the sample to be measured. On top of the core layer another three layers are deposited comprising 2 cladding layers and a thick superstrate layer[45]. All layers are formed from dielectric materials and the RIs of the claddings adjacent to the sample or core region are higher than the RI of the sample. The 2 cladding layers on either side of the core form a Fabry-Perot antiresonant cavity and thus light is confined inside the core region by this cavity. The intensity of the confined light changes due to a change in the RI of the sample medium in the core channel.

A variety of interferometer setups have been suggested for biosensing.[11, 15, 26, 46, 47, 48] However, they typically involve a waveguide for evanescent sensing of a cover medium's RI or a channel containing the sample in which the light propagates for measuring the RI of the sample. The phase of the light interacting with the sample is then compared to the phase of light that has propagated through a channel containing a reference medium or in a waveguide covered with a reference medium, respectively. Thus, the interferometer setups merely provide a way to increase the sensitivity of a given sensor by adding a reference signal. One example is the commercially available biosensing system *Analight® Bio200*[49], which is based on interferometric sensing using a dual waveguide interferometer.

In general, the planar structured sensors are the most simple to fabricate avoiding fabrication steps like etching. The evanescent field sensors have shown high sensitivity to RI changes in the close vicinity of the sensor surface approximately within 100 nm due to the limited penetration depth

of the evanescent field in the cover and are very suitable for adlayer changes and RI changes of uniform sample media.

How sensitive is the waveguide sensor to an adlayer?

The adlayer sensitivity $\partial N_m/\partial d_A$ can be derived from the mode equation Eq. (2.2) as:[19]

$$\frac{\partial N_m}{\partial d_A} = \left[\frac{n_F^2 - N_m^2}{N_m(d_S + d_F + d_C)} \frac{n_A^2 - n_C^2}{n_F^2 - n_C^2} \left(\frac{(N_m/n_C)^2 + (N_m/n_A)^2 - 1}{(N_m/n_C)^2 + (N_m/n_F)^2 - 1} \right)^{\rho} \right]. \qquad (2.14)$$

The calculated adlayer sensitivity is shown in Fig. 2.13 vs. film thickness for TE and TM polarized light and mode orders $m = 0 - 3$.

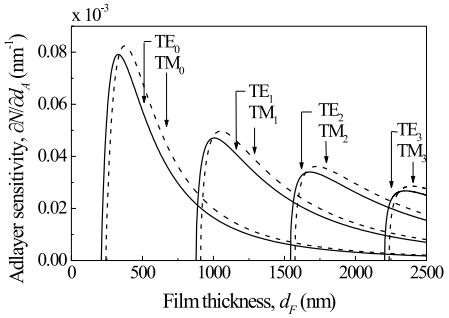

Figure 2.13. Calculated $\partial N_m/\partial d_A$ vs. film thickness for $m = 0 - 3$ for TE and TM polarized light. The used RIs are: n_S = 1.517, n_F = 1.59, n_C = 1.33, n_A = 1.5 and the thickness d_A = 1 nm.

It is seen that an optimum adlayer sensitivity is obtained for a film thickness just above cutoff film thickness for each of the modes with the maximum adlayer sensitivity obtained for the lowest order waveguide mode and for TM polarized light. Comparing the adlayer sensitivity with the cover RI sensitivity calculated in Fig. 2.9 for the same waveguide configuration shows a similar shape of the curves for the two sensitivities and the change in adlayer sensitivity vs. film thickness is caused by the change in the penetration depth of the evanescent field in the cover and substrate which decreases at different rates for a given change in film thickness.

However, it is possible to increase both sensitivities by increasing n_F. Also the sensitivities can be increased by lowering n_S towards n_C as the critical angle at the two film boundaries becomes less separated in value and thus the mode profile becomes more symmetrical. Thus summarizing, the optimum sensitivity of the waveguide sensor is achieved by choosing n_S and n_F for a given n_C according to: $(n_S - n_C)$ as low as possible and $(n_F - n_C)$ as high as possible.

Using a dielectric waveguide sensor, it has been shown by Horvath et al[50] that it is possible to measure a change in adlayer thickness below 0.5 nm. The measurement were on lipid bilayers and the thickness of the adlayer was measured vs. temperature changes.

2.3 Discussion

A waveguide sensor is an evanescent field sensor for which the waveguide mode is the sensing feature. The guided electromagnetic field of the waveguide mode extends as an evanescent field into the cover and substrate media and senses an effective refractive index N_m of the waveguide. Due to the part of the electromagnetic field that extends into the cover medium a change in RI of the cover medium results in a change in N_m.

Waveguide modes are only excited in the waveguide when d_F is above the cutoff film thickness and the number of waveguide modes excited in the waveguide increases with film thickness, where the waveguide mode order, m describes the profile of the electromagnetic field in the waveguide.

For the waveguide sensor the sensitivities can be calculated from Eqs. 2.11 and 2.14 and the optimum sensitivity can be changed by adjusting the RIs of the substrate and the film as the sensitivity of the sensor depends on the penetration depth of the evanescent field in the cover. Both a maximum adlayer sensitivity and a maximum cover RI sensitivity is obtained for the waveguide mode for the 0^{th} order TM mode and a film thickness just above cutoff film thickness.

The penetration depth of the evanescent field in the cover is the important parameter for detection of micron-scale objects. Especially for cells, the evanescent field should be large enough to extend across the aqueous gap that may occur between a cell settling on a sensor surface and the actual sensor surface, when the cell is contained in an aqueous medium.

For the dielectric planar waveguide the penetration depth is limited to a few hundred nanometers which makes the sensor suitable for detection of the presence of an adlayer or for measuring changes in thin adlayers on the sensor surface. The sensor also has a high sensitivity for measurements of RIs of uniform aqueous solutions.

Specific detection of biological objects can be performed by coating the sensor surface with a specific recognition agent and the signal from the specific detection can be amplified by labelling the objects to be measured. However, a bio-sensor should preferably be sensitive enough to detect unlabelled objects as this simplifies the sample preparation and reduces the costs for each sample to be analyzed.

In the following chapters the reverse symmetry waveguide sensor and two metal-clad waveguide (MCWG) sensors, the dip- and the peak-type MCWG, will be presented. The reverse symmetry waveguide sensor has a similar configuration to the conventional waveguide sensor presented in this chapter, however with a reversed symmetry i.e. $n_C > n_S$. The application of the reverse symmetry waveguide as a sensor is based on the ability of exciting waveguide modes in the waveguide film. The dip-type MCWG comprises a waveguide structure with thin metal-layer and thus comprises an additional layer compared to the dielectric waveguide sensors. However, similar to the dielectric waveguide sensors, the application of the dip-type MCWG as a sensor is based on the ability of exciting waveguide modes in a dielectric layer of the structure. The peak-type MCWG

also utilizes the ability to excited waveguide modes in a dielectric layer of the structure, which is similar to that of the dip-type MCWG. Contrary to the other sensors the peak-type MCWG is operated off-resonance of the waveguide mode as another interesting feature in the sensorgram of this configuration can be applied for sensing purposes. The common features for the sensors to be presented in the next chapters are that they are all evanescent wave sensors and that they all have a large penetration depth of the evanescent field in the cover medium and hence, they are all deep-probe sensors.

Chapter 3

Reverse symmetry waveguide sensors

In this chapter the reverse symmetry waveguide sensor is introduced which is closely related to the dielectric, planar waveguide sensor in the previous chapter. Hence, the basic properties of the dielectric waveguide presented in chapter 2 also applies for the reverse symmetry waveguide sensor and frequent references to the previous chapter will occur.

What is a reverse symmetry waveguide?

The reverse symmetry waveguide is a planar dielectric waveguide with a configuration similar to the configuration of the waveguide shown in Fig. 2.1 comprising a substrate, a waveguide film and a cover medium. However, for the reverse symmetry waveguide the substrate RI is *lower* than the cover RI, i.e. $n_S < n_C$. As for the dielectric waveguide $n_F > \{n_S, n_C\}$ thus, the light in the reverse symmetry waveguide is also guided by TIR resulting in excitation of waveguide modes when constructive interference between the light beams in the waveguide film occurs.

Why is the reverse symmetry configuration interesting?

The interesting feature of the reverse symmetry waveguide sensor is that a high penetration depth of the evanescent field in the cover medium can be achieved and moreover a penetration depth in the cover medium that is higher than the substrate penetration depth, thus resulting in a higher influence of n_C on the sensed N_m for the reverse symmetry waveguide than for the dielectric waveguide. This is seen from the mode profiles calculated in Fig. 2.6 for the dielectric waveguide where a large penetration depth is achieved in the substrate or in general terms in the adjacent medium of the waveguide film with the highest RI.

For a waveguide comprising a substrate of air, a polystyrene film and a cover of water the cover and substrate penetration depths $d_{P,C}$ and $d_{P,S}$ given by Im[$k_{z,C}^{-1}$] and Im[$k_{z,S}^{-1}$], respectively, are

calculated in Fig. 3.1 vs. film thickness for the mode orders $m = 0 - 3$ for TE and TM polarized light.

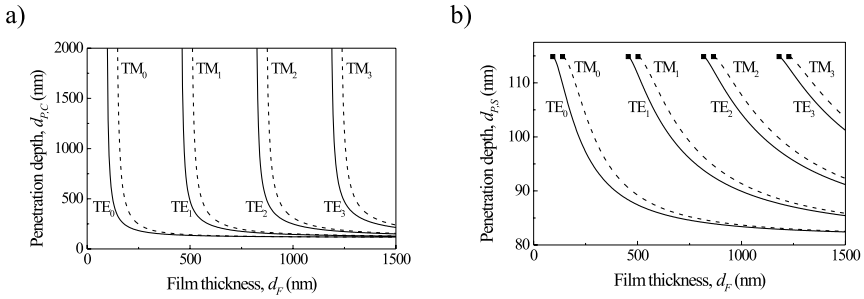

Figure 3.1. Calculated penetration depths for $m = 0 - 3$ of the evanescent field in the cover $d_{P,C}$ (a) and in the substrate $d_{P,S}$ (b) vs. film thickness for TE and TM polarization. The RIs used are: n_S = 1, n_F = 1.59 and n_C = 1.33.

The cover penetration depth $d_{P,C}$ for the reverse symmetry waveguide goes to infinity at the cutoff film thickness for the different mode orders m and decreases fast to a few hundred nanometers for an increase in film thickness of $\sim$ 100 nm from the cutoff film thickness. A further increase in film thickness decreases the penetration depth further but at a much slower rate.

The substrate penetration depth $d_{P,S}$ also decreases with increasing film thickness but at a slower and more even rate. At cutoff film thickness (squares) $d_{P,S}$ reaches a limited depth of 115 nm, which is equal for all modes. Logically, the penetration depths for the reverse symmetry waveguide configuration shows the opposite situation of that for the normal symmetry waveguide in Fig. 2.7.

The infinite penetration depth of $d_{P,C}$ at cutoff film thickness occurs because N_m approaches n_C for this film thickness, see Fig. 3.2 where N_m vs. film thickness is calculated for the same waveguide configuration as used for the calculated penetration depths above. At N_m = n_C the

waveguide mode angle θ_m is given by the critical angle $\theta_{Critical}$, see Fig. 2.2 at which the light changes from being normal propagating waves to an evanescent field.

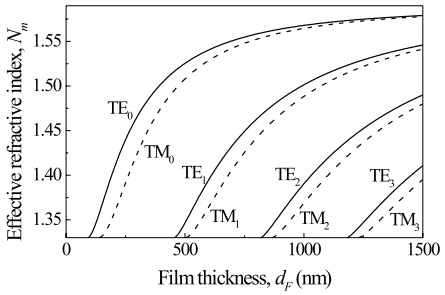

Figure 3.2. N_m calculated vs. film thickness for mode orders $m = 0 - 3$ for both TE and TM polarized light. The RIs of the configuration are: n_S = 1, n_F = 1.59 and n_C = 1.33.

From Fig. 3.2 it is seen that N_m for the reverse symmetry waveguide has a value in the range n_C to n_F starting at n_C for a film thickness given by the cutoff film thickness and increases to n_F as the film thickness is increased. For a planar three-layer dielectric waveguide configuration N_m has a value ranging from $\max\{n_S, n_C\}$ to n_F in agreement with N_m calculated for the normal symmetry waveguide in Fig. 2.4 with $n_S < N_m < n_F$.

How sensitive is this sensor configuration?

The cover RI and adlayer sensitivities of the reverse symmetry configuration are calculated using Eqs. (2.11) and (2.14) and are shown in Fig. 3.3 vs. film thickness for $m = 0 - 3$ for TE and TM polarized light.

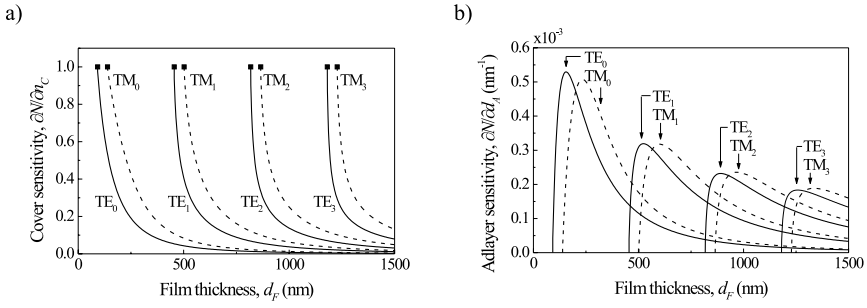

Figure 3.3. Calculated cover RI sensitivity $\partial N_m/\partial n_C$ (a) and adlayer sensitivity $\partial N_m/\partial d_A$ (b) vs. film thickness for TE (solid lines) and TM (dotted lines) polarized light. The parameters used are: n_S = 1, n_F = 1.59 and n_C = 1.33.

The cover RI sensitivity calculated in Fig. 3.3(a) equals 1 at the cutoff film thickness and decreases for increasing film thickness. From the calculated penetration depth in the cover medium in Fig.

3.1 the infinite penetration depth at cutoff thickness has the result that the sensed N_m mainly depends on n_C. The adlayer sensitivity $\partial N_m/\partial d_A$ in Fig. 3.3(b) shows that the optimum sensitivity is obtained for a film thickness slightly thicker than the cutoff film thickness. This is due to a reduced penetration depth in the cover for which the evanescent field in the cover senses the given adlayer with optimum effect and not a large part of the cover medium.

The optimum sensitivity calculated in Fig. 3.3 is $\partial N_m/\partial n_C$ = 1 for all modes and for both polarizations at cutoff film thicknesses while the optimum $\partial N_m/\partial d_A$ = 0.53 10^{-3} nm^{-1} is obtained for d_F = 155 nm for the TE polarized waveguide mode $m = 0$.

The adlayer sensitivity can be increased by adjusting the RIs of the waveguide by choosing n_F and n_S so that $(n_F - n_C)$ and $(n_C - n_S)$ both are as high as possible. The cover RI sensitivity approaches one for all waveguide modes at cutoff film thickness and cannot be increased to a higher value for the reverse symmetry dielectric waveguide configuration.

Compared to the normal symmetry dielectric waveguide, the maximum achievable sensitivity of the reverse symmetry waveguide sensor for the mode order $m = 0$ for a substrate of $n_S = 1.517$ and $n_S = 1$, respectively with $n_F = 1.59$ and $n_C = 1.33$ is 20-fold and 6-fold higher for the cover and adlayer sensitivity, respectively.

Can this configuration be realized?

For biosensing the cover medium will typically comprise an aqueous solution containing the biological substances to be detected, but also detection of air borne bacterial pathogens is a possible application. This means that to obtain a waveguide sensor with reverse symmetry the substrate RI should be lower than that of water for aqueous samples or the substrate should be air ($n_S = 1$) for detection of objects contained in air.

How to realize the reverse configuration in practice is not obvious as solid materials with a RI below 1.33 are rarely found and also considering the issue of mechanical stability of the thin waveguide film if a non-solid material is used e.g. air (as used in the above calculations).

One material to use for the substrate is teflon with a RI of 1.3,[51] however using a n_S close to n_C will require a very thin waveguide film to be operated as a single mode waveguide, d_F $\approx$ 30 nm for a teflon substrate, polystyrene film and water for the cover medium. Fabricating a film this thin can complicate the fabrication process and the further chemical treatment of the surface for specific binding. Another possibility is to use a nanoporous material which is a solid material filled with air bubbles smaller than the wavelength of the light used in the setup. Reverse symmetry waveguides with a substrate of porous silica ($n_S = 1.2$) have been thoroughly described in references [29, 52, 53, 50], implemented and successfully used for cover RI measurements, bacteria and cell detection.[29, 53, 50]

However, the simplest possible reverse symmetry waveguide would be to use a simple glass plate as a waveguide sensor; air substrate and the glass plate as the waveguide film. I wanted to in-

vestigate this sensor configuration for both the theoretical sensitivity and the practical aspects of applying this configuration as a sensor, involving the fabrication, setup and experiments.

The use of air for the substrate is a possible configuration for the sensor, but to ensure the mechanical stability the waveguide film has to have a certain thickness to avoid bending when the cover medium is applied, resulting in a multimode waveguide. For a single mode waveguide with air as substrate the film should have a thickness around 150 nm for a film of RI 1.59 for highly sensitive measurements.

3.1 Free standing multimode waveguide sensor

Both the normal and the reverse symmetry waveguide sensors can be used in multimode operation, where several waveguide modes can be excited in the waveguide film. However, contrary to the normal symmetry, dielectric waveguide sensor the reverse symmetry waveguide sensor has the advantage that the maximum number of modes that can be excited in the waveguide film is quite sensitive to the RI of the cover medium.

In Fig. 3.4 the maximum number of waveguide modes vs. n_C is calculated and shown as the highest order mode vs. n_C for the reverse symmetry multimode waveguide with air substrate (solid line) and for the normal symmetry waveguide with the RIs of the commercially available OW2400[34] waveguide sensor (dashed line) both with a 50 μm thick waveguide film.

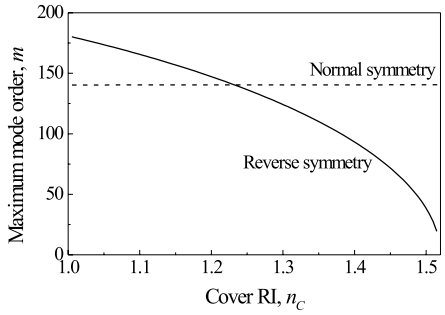

Figure 3.4. Calculated highest order mode vs. n_C for a reverse symmetry (solid line) waveguide sensor and for a normal symmetry (dashed line) waveguide sensor for TE polarized light with wavelength λ = 632.8 nm. The parameters used are: n_F = 1.52, d_F = 50 μm and n_S = 1 for the reverse symmetry waveguide and for the normal symmetry waveguide n_F = 1.77 d_F = 50 μm and n_S = 1.53.

From Fig. 3.4 it is seen that the number of waveguide modes supported in the normal symmetry waveguide are practically independent on n_C, whereas the number of modes excited in the reverse symmetry waveguide show a strong dependence on n_C. The curves calculated for TM polarized light are basically coincident with the curves for TE polarized light.

What is the sensing principle for the freestanding multimode waveguide sensor?

For a multimode waveguide several waveguide modes can be excited, each for a different resonant angle, θ_m of the light incident at the film interfaces with the cover and substrate, where the θ_m's are above the critical angle, $\theta_{Critical}$ as illustrated in Fig. 3.5.

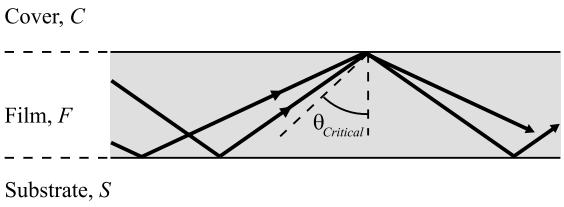

Figure 3.5. Multimode operation of a planar waveguide.

The sensing principle for the multimode reverse symmetry waveguide is similar to that of the single mode. Light is coupled into the waveguide at the end facet of the waveguide film over a range of angles and the outcoupled light at the other end facet of the waveguide film is measured with a photo detector, thus a sensorgram of intensity vs. angle is measured. The resulting sensorgram comprises a curve with several peaks in the intensity, one for each waveguide mode m excited in the waveguide at the waveguide mode angle θ_m. In Fig. 3.6 the sensorgrams from a 4 μm thick free standing waveguide are illustrated for cover media $n_C = 1.33$ and $n_C = 1.36$, where modes $m = 0 - 10$ can be excited.

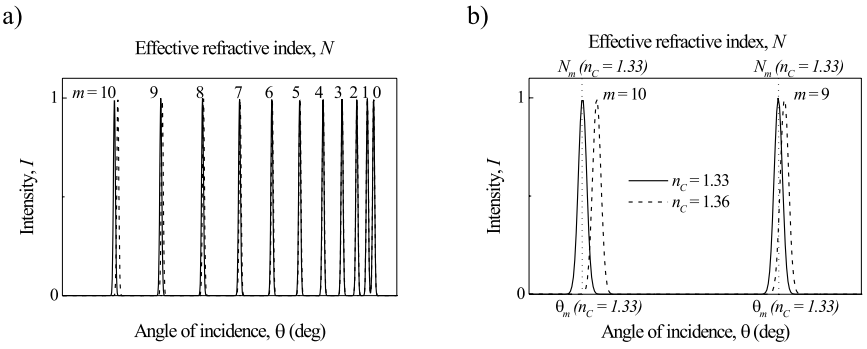

Figure 3.6. Illustration of sensorgrams from a multimode waveguide for two values of the cover medium RI, n_C = 1.33 and n_C = 1.36, for TE polarized light. (b) Detailed section of the sensorgrams. The parameters used are: n_S = 1, n_F = 1.59, d_F = 4 μm, n_C = 1.33 and n_C = 1.36.

A change in the cover medium RI n_C will give a different phase change of the reflected light at the cover/film interface $\phi_{F,C}$ and thus the incident angle θ_m for which the wavefronts are in phase and constructive interference occurs will change. Thus, the basic sensing principle of the multimode reverse symmetry waveguide is like for the single mode waveguide to detect a change in position of a given waveguide mode due to a change in n_C. However, for the multimode waveguide several

modes can be excited, which all change in angular position due to a change in n_C. From the sensorgrams from a multimode free standing waveguide in Fig. 3.6 it is seen that for $n_C = 1.33$ and $n_C = 1.36$ 11 modes can be excited in the waveguide for which the inter-mode distance increases with the mode order and that the change in angular position due to a change in n_C also increases with mode order.

The highest order mode experiences the largest shift in angular position and are thus the most sensitive to a change in the cover medium or in the adlayer, this is also seen from the sensitivities calculated in Fig. 3.3 for a given d_F. This is due to the fact that N_m of the highest order mode is close to n_C (Fig. 3.2) and thus is the waveguide mode with the highest penetration depth in the cover (Fig. 3.1). For optimum sensing of a change in the cover medium the sensing principle will thus be to detect the change in position of the highest order waveguide mode. In addition it is important to mention that the maximum number of waveguide modes that can be excited in the waveguide changes when n_C is changed which is seen from Fig. 3.4.

Besides our group only Qi et al have presented a freestanding waveguide also made from a simple glass plate. Qi et al present a prism coupled freestanding waveguide applied for cover RI measurements.[54] They limit the detection range to a range of RIs within which the number of waveguide modes does not change and use the highest order mode as sensing probe. Instead of detecting the change in position of the given mode due to a change in n_C they measure the intensity of the guided light at a fixed angle, resulting in a limited detection range for that specific sensor configuration of 1.5x10^{-3} RIU (refractive index units) for aqueous solutions.

Contrary, we have suggested to use the number of modes as the sensing feature to obtain a sensor for broad range detection, however resulting in a lower sensitivity to that of Qi et al. Using the number of modes as the sensing feature enables the sensor to be used as a refractometer for measuring the absolute RI of both gases and liquids.

How sensitive is the freestanding multimode waveguide sensor?

The sensitivity of the sensor depends on which sensing probe is applied. Qi et al[54] states a sensitivity of 3x10^{-5} RIU when using the intensity of the highest order mode as the sensing probe. Using the number of modes as the sensing feature for broad range detection results in a sensitivity that changes with n_C, where the sensitivity is reduced for low n_C values. The inter-mode distance is the parameter that determines the sensitivity and from Figs. 3.4 and 3.6 it is seen that the inter-mode distance is high for low cover RIs and decreases for high cover RIs and thus the sensitivity increases with n_C.

In Fig. 3.7 the resolution Δn_C of the freestanding waveguide sensor is calculated for waveguides of thickness 52 μm, 100 μm, 200 μm and 400 μm. The resolution Δn_C is given by the change in n_C that cases a change in number of modes of one waveguide mode.

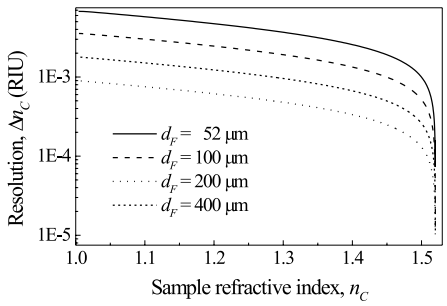

Figure 3.7. Calculated resolution vs. cover RI for the freestanding multimode waveguide sensor with 4 different film thicknesses for TE polarized light with wavelength λ = 632.8 nm and RIs n_S = 1, n_F = 1.59.

From Fig. 3.7 it is seen that the resolution of a 52 μm thick waveguide varies from 7x10^{-3} RIU at n_C = 1 down to 5x10^{-5} RIU at $n_C = n_F$. However, by increasing the film thickness the resolution can be increased due to more excited modes in the waveguide within the same detection range or by choosing a waveguide film with a RI close to the cover RI which decreases the number of modes and the detection range and hence approaches the single mode operation. A higher RI of the waveguide film increases the detection range but decreases the resolution for a cover medium RI around RI of water. A combination of the sensing method presented by Qi et al and the mode-counting sensing method predicts a sensor with a broad detection range and high sensitivity.

It is also seen from Fig. 3.7 that the sensitivity basically increases linearly with n_C from n_C = 1 to n_C = 1.45, which simplifies the processing of the signal.

3.2 Experiments

In connection with this work I have fabricated and used a freestanding multimode waveguide sensor for RI measurements and used the detection of the number of modes excited in the waveguide as the sensing feature.

What is the configuration of this sensor?

The freestanding multimode waveguide sensor simply consists of a glass plate with a thickness of 52 μm onto which the cover medium is applied. The light is coupled into the waveguide by use of a incoupling grating for which the 1.st diffraction order is coupled into the waveguide film.[18]

The incoupling grating is moulded in a 40 nm thin polystyrene (PS) film on the glass plate, see Fig 3.8 for illustration.

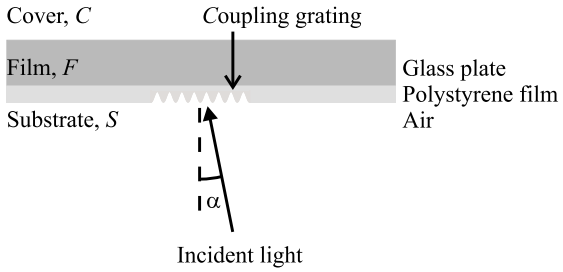

Figure 3.8. The fabricated freestanding multimode waveguide configuration.

The light is coupled into the waveguide by illuminating the coupling grating in Fig. 3.8 from below at a range of angles, α.

How is the sensor fabricated?

The waveguide is fabricated by applying a 40 nm thin PS film on a cleaned 52 μm glass plate and imprinting the grating in the polystyrene film. In Fig. 3.9 the glass plate used for the waveguide film is shown at the end of a vacuum tweezers. The glass plate is 8 x 8 mm^2, 52 μm thick and has a RI of 1.52.

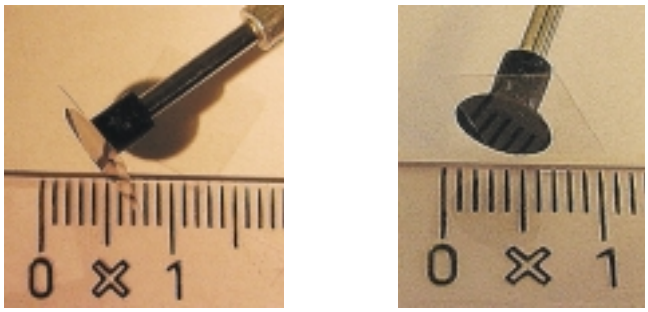

Figure 3.9. Photographs of the 52 μm thin glass plate used as the waveguide film of the freestanding multimode waveguide. The glass plate is at the end of the vacuum tweezers.

In general, thin polymer films with a uniform thickness can be fabricated by spin coating a polymer solution onto a substrate with a smooth horizontal surface. However, for this waveguide it is not feasible to spin coat the PS film directly on the 52 μm thin glass plate because the vacuum applied to the substrate during spin coating will make the thin glass plate bend. Instead, I fabricated the thin PS film by spin coating the dissolved PS [Mw: 1410000, Mw/Mn: 1.05 from Polymer Source Inc., Canada] onto a thicker glass plate and transferred it to the thin glass plate by dip-floating, the steps in this process are illustrated in Fig. 3.10.

The thin PS film is first spin coated on a 5x5 cm^2 glass plate of 1 mm thickness from a toluene solution of the PS (Concentration: 0.5 g PS / 50 mL toluene) at a spinning speed of 2000 rpm

for 20 s, illustrated in Fig. 3.10(a). During spin coating the toluene partly evaporates and the PS film has a density that makes it possible to transfer it to the glass waveguide by dip-floating. The film is cut into 2 x 2 cm^2 pieces on the 5 x 5 cm^2 glass plates by a sharp knife (not shown in the figure) and subsequently the glass plate is gently pushed through an air/water interface of a water bath (Fig. 3.10(b)). Because the PS is hydrophobic the water enters between the glass and the thin polystyrene film resulting in a freely floating PS film on the water surface (Fig. 3.10(c)). The floating film can now be deposited onto the glass waveguide by holding the waveguide with a vacuum tweezers and pressing it down on top of the floating PS film and into the water (Fig. 3.10(d)) and removing it from the water bath in one motion keeping the PS-covered surface of the glass waveguide in the forward motion direction.

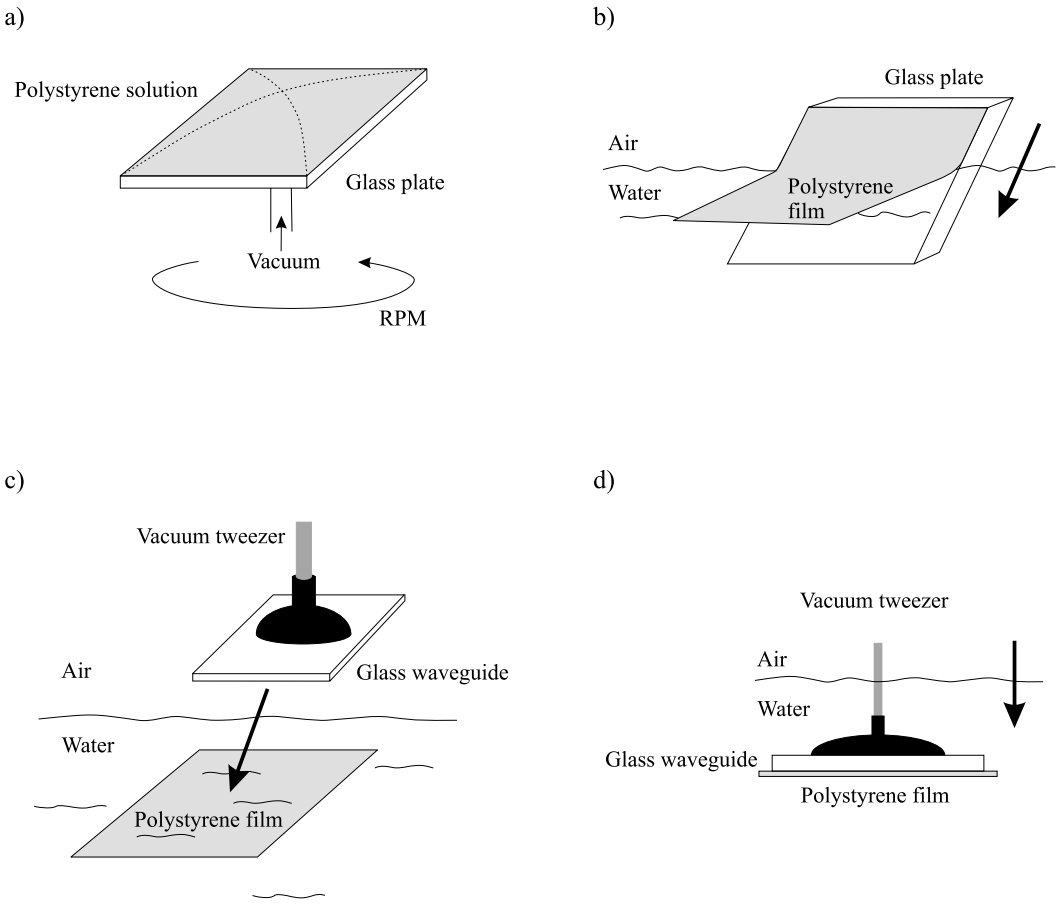

Figure 3.10. Procedure for the deposition of the PS film onto the glass waveguide. (a) Spin coating of the 40 nm thin PS film on a 5 x 5 cm^2 glass plate. (b) Dip-floating of the PS film. (c) Free floating PS film on the surface of a water bath. (d) Deposition of the PS film onto the glass waveguide.

The waveguide structure is subsequently left in an oven at 110°C for 30 min to dry and to remove the remaining toluene in the film.

The thickness of the film is measured on a separate film transferred to another 1 mm thick glass plate by dip-floating, following the same procedure as describe above. Mechanically removing parts of the film enables 2D measurements of the film thickness using a surface profiliator (Dektak V 200-Si, Veeco).

The coupling grating in the PS film is imprinted in the film by hot-embossing using a Poly-(Dimethylsiloxane) (PDMS) stamp [PDMS from Dow Corning, Sylgaard 184]. The grating is 2 mm wide perpendicular to the grating lines, with a grating period Λ = 481 nm and depth of $\sim$ 25 nm.

In Fig. 3.11(a) the fabrication of the stamp used for imprint of the grating is illustrated along with the process of imprinting the grating in the film, illustrated in Fig. 3.11(b).

The PDMS grating stamp is fabricated by use of a grating master. The grating master is fabricated holographically in photoresist using a He-Cd laser (λ = 441.6 nm).[52] A PDMS layer $\sim$ 1 mm thick is poured onto the grating master and heat cured at 80°C for 24 h. After removal from the oven and left to cool down the moulded PDMS can easily be peeled off and used for printing of gratings in the waveguide structure.

AFM images of the photoresist grating master and the PDMS grating stamp in Fig. 3.12 (a) and (b), respectively, show that the PDMS replica is a perfect image of the original master which indicates that the PDMS stamp is intact when it is peeled off the grating master and that the grating master can be reused

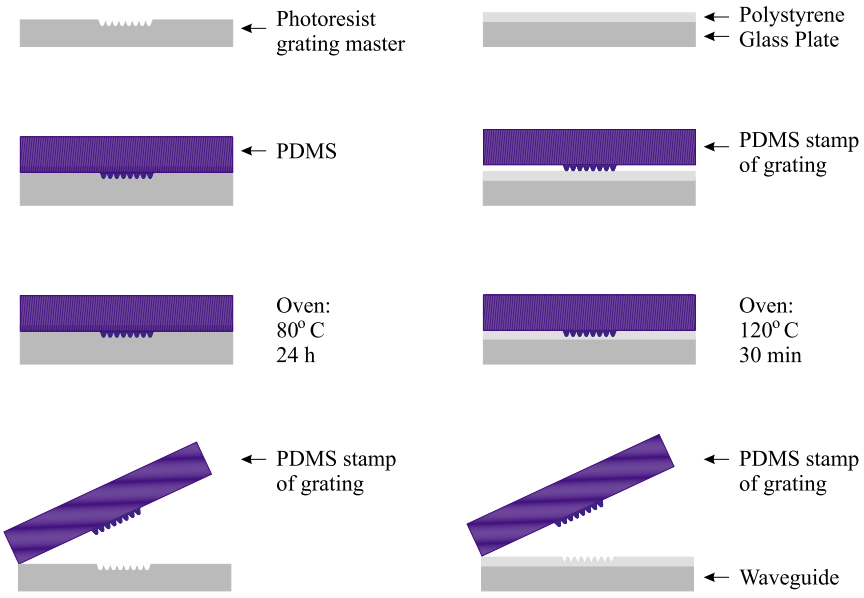

Figure 3.11. (a) Illustration of the steps involved in the fabrication of (a) the PDMS grating stamp and (b) the coupling grating in the PS film of the waveguide.

For imprint of the coupling grating in the thin polystyrene layer on the waveguide the elastic PDMS grating stamp is placed on top of the polystyrene film of the PS/glass waveguide structure. With the stamp placed on the PS film the waveguide structure is heated in an oven at 120°C which is above the glass transition temperature of PS. The structure is heated for 30 min after which it is removed from the oven and left to cool down, subsequently the stamp can be peeled of the structure leaving a print of the grating in the PS film and the waveguide is ready for use, see Fig. 3.11(b).

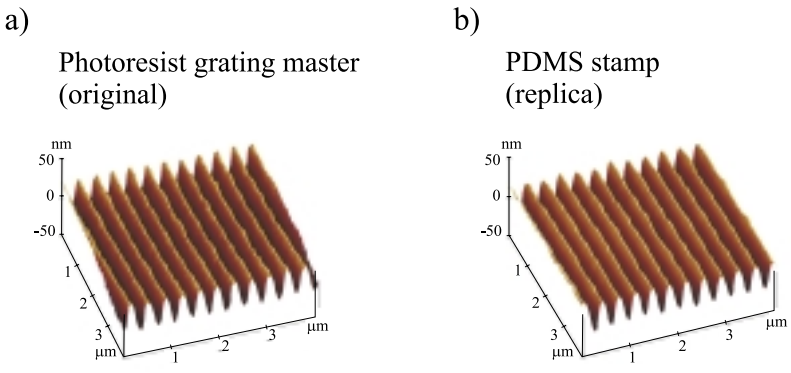

Figure 3.12. AFM images of the grating master (a) and the PDMS stamp (b). The grating period Λ = 481 nm and the depth of the grating is approximately 25 nm.

What experimental setup is used for the sensor?

The waveguide is placed on a holder with the incoupling grating downwards and a He-Ne laser illuminates the grating from below, see Fig. 3.13. The holder of the waveguide sensor is made such that the holder influences the sensor substrate of air as little as possible. A cuvette with in- and outlet tubes is placed on top of the waveguide. Via the in- and outlet tubes in the cuvette it is possible by use of a peristaltic pump to continuously change the cover solution without having to

dismount the setup. Photographs of the waveguide holder and the cuvette is shown in Fig. 3.14 (a) and (b), respectively.

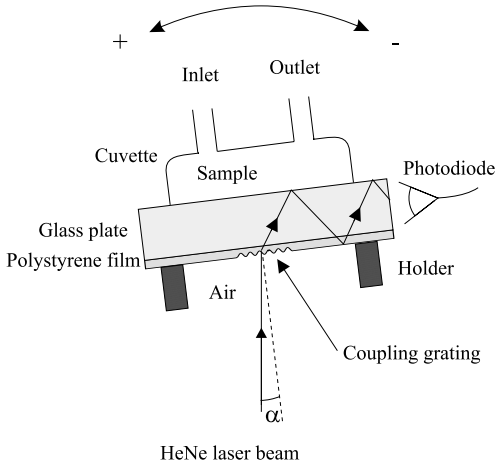

Figure 3.13. Experimental setup for the freestanding multimode waveguide sensor.

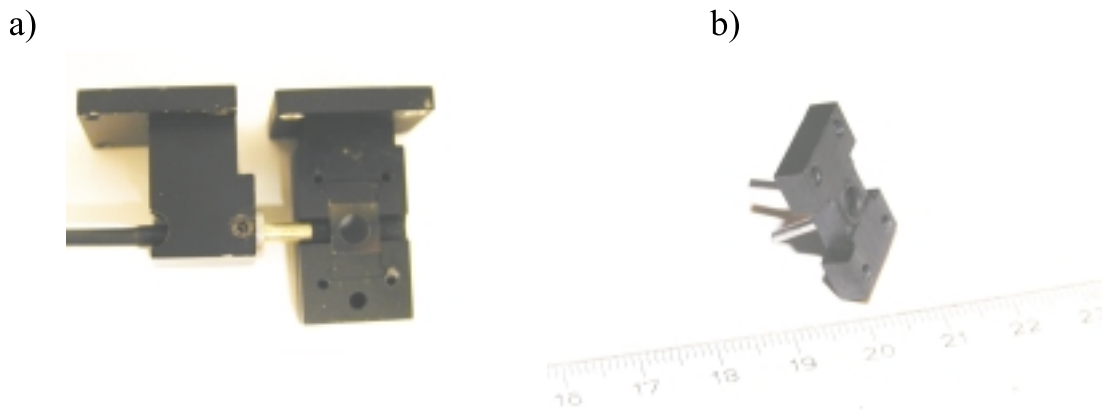

Figure 3.14. Photograph of the holder (a) and cuvette (b) for the multimode waveguide sensor.

At the end facet of the glass plate a detector is placed to measure the intensity of the guided modes. The whole setup is placed on a high precision goniometer to vary the angle of incidence, α of the He-Ne laser light to measure the intensity of the emitted light vs. angle of incidence.

At the specific mode coupling angle α_m for the effective RI of the waveguide mode m, N_m, the given waveguide mode is excited and for a grating coupled waveguide the specific mode coupling angles are given by the grating equation:

$$N_m = \sin(\alpha_m) + \lambda/\Lambda, \tag{3.1}$$

where λ is the vacuum wavelength of the light and Λ is the grating period.

From Fig. 3.2 it is known that for the highest order mode $N_m \cong n_C$ thus applying Eq. (3.1) to the highest order mode the grating equation can be expressed as:

$$n_C = \sin(\alpha_{m,max}) + \lambda/\Lambda, \tag{3.2}$$

where $\alpha_{m,max}$ is the coupling angle of the highest order mode. Thus, simply by measuring $\alpha_{m,max}$, the absolute cover RI can be determined from Eq. (3.2).

What measurements are conducted?

An experiment with the following NaSCN-water solutions has been carried out: Pure water (n_C = 1.331), 5% w/w NaSCN (n_C = 1.342) and 10% w/w NaSCN (n_C = 1.354) [Table values from reference [55]]. The experimental setup used in the experiment is shown in Fig. 3.13 and the cover solution in the cuvette is changed in the order: Pure water, 5% w/w NaSCN, pure water, 10% w/w NaSCN and pure water (w/w: weight by weight).

The measured sensorgrams for the three different cover solutions are shown in Fig. 3.15.

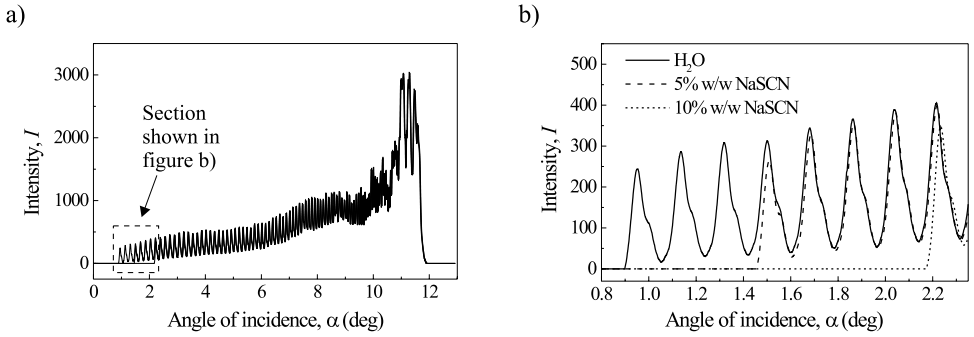

Figure 3.15. Sensorgrams for samples of pure water, 5% w/w NaSCN solution and 10% w/w NaSCN solution (a). (b) Detailed section of the sensorgram of the highest order modes for coupling angles α = 0.8 deg to α = 2.3 deg. The light source is a He-Ne laser of λ = 632.8 nm and with mixed TE and TM polarized light.

A number of peaks are observed in the sensorgrams measured for each solution and an increase in the intensity is observed with increasing angle. Each peak corresponds to a waveguide mode and calculations show that the inter-mode distance of the modes increases with the mode number resulting in a clear mode separation at small angles of incidence and an overlap of the individual modes at larger angles, see Fig. 3.4 and thus an increase in the intensity.

From the detailed section of the sensorgrams for coupling angles α = 0.8 deg to α = 2.3 deg (Fig. 3.15(b)) it is seen that the resonant angle of the highest order mode possible to excite in the waveguide changes with n_C. However, this is not due to a change in position of the individual modes but occurs due to the maximum number of modes possible to excite in the waveguide changes de-

pending on n_C. Calculations of the number of modes that can be excited in the waveguide result in: 121 for pure water, 118 for 5% w/w NaSCN and 114 for 10% w/w NaSCN shown in Fig. 3.16. This shows agreement with the measurements where the number of modes disappearing is 3 and 7 respectively when changing the cover solution from pure water to 5% w/w NaSCN and from pure water to 10% w/w NaSCN.

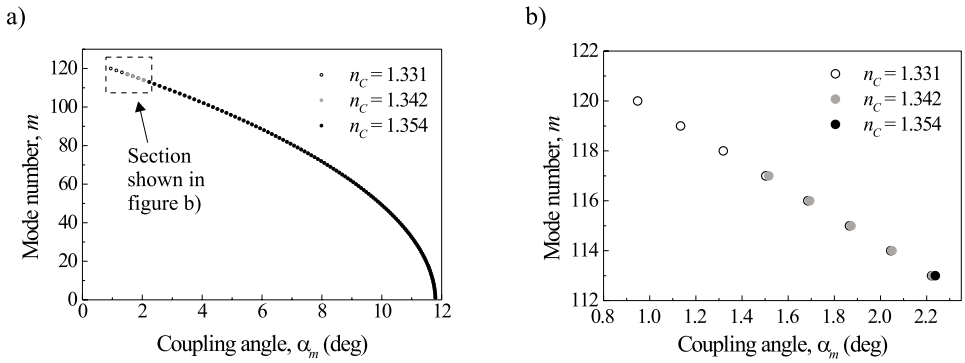

Figure 3.16. Calculated highest order TE modes vs. coupling angle for the present waveguide with a cover RI of the liquids used in the experiments (a). (b) Detailed section of the calculations for coupling angles 0.8 deg to 2.35 deg.

The measured coupling angle for the highest order mode in each spectrum recorded during the experiment is shown in Fig. 3.17. The corresponding n_C from Eq. (3.2) is shown and gives following readings: n_C = 1.332 for pure water, n_C = 1.342 for 5% w/w NaSCN and n_C = 1.355 for 10% w/w NaSCN which gives an accuracy of 0.001 compared to the above mentioned table values. The measured angle of incidence for the highest order mode shows that the single measurements are reproducible when reapplying pure water after the NaSCN-water solutions.

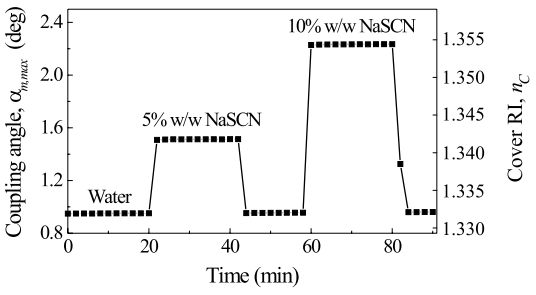

Figure 3.17. Measured coupling angle and corresponding n_C of the highest order mode vs. time for cover media of pure water, 5% w/w NaSCN solution, pure water, 10% w/w NaSCN solution and pure water.

For the freestanding waveguide it is possible to measure the RI of media between the RI of the substrate and the film ranging from gases to very dense liquids thus contrary to Qi et al we have

shown that this configuration can be used as a broad range refractometer. The freestanding waveguide is probably the most simple waveguide configuration, as it basically only consists of a glass plate. The demonstrated fabrication involves dip-floating of the thin polystyrene film for the grating, however the waveguide including the coupling grating has the possibility of being fabricated in one process in one material i.e. by polymer injection moulding or by etching of the grating directly in the waveguide.

3.3 Discussion

The reverse symmetry waveguide sensor is an evanescent field sensor with a penetration depth of the evanescent field in the cover medium of infinity at the cutoff film thickness and a high cover RI sensitivity $\partial N_m / \partial n_C$ = 1.

Reverse symmetry waveguides are suitable for both multimode and singlemode sensors. A thorough study of the singlemode sensor has been presented in the literature, which shows that a large evanescent field can be obtained in the cover medium. Results from measurements with the singlemode reverse symmetry waveguide sensor for detection of whole cells and bacteria on the sensor surface show very good results.

A freestanding, multimode, grating coupled waveguide sensor was presented for broad-range absolute refractive index measurements. Using the number of excited waveguide modes for detection the sensor gives an accuracy of absolute refractive index of 0.001 and a dynamic range of n_C between 1 and 1.52. One other group (Qi et al) has suggested the same waveguide configuration but using prism-coupling and used for a very limited detection range. The freestanding multimode waveguide is the most basic configuration of dielectric waveguides as the waveguide only consists of a simple glass plate. This sensor shows possibility of a fairly easy fabrication involving a single material and a fabrication process involving a single step.

Chapter 4

Metal-clad dip-type waveguide sensors - Theory

The metal clad dip-type waveguide was presented by the group of Salamon et al for various biosensing purposes.[56, 57] The sensor was presented as a coupled plasmon-waveguide resonator (CPWR) and has been applied for measurements of lipid bilayer with resulting characterization of the thickness, the RI and the extinction coefficient of the lipid bilayer and for measurements of the optical anisotropy in lipid bilayer membranes.[56, 58]

Other measurements performed by the Salamon group with the sensor have also included interactions between membrane-associated proteins and enzymes with lipids including integral and surface proteins in lipid bilayers,[59]–[63] and receptor-ligand interactions.[64]–[68]

However, in connection with the experiments the groups have presented two different configurations of the sensor but no theoretical study of the sensor.

Generally, no thorough theoretical study of this waveguide sensor has been presented in the literature. Due to the results obtained by Salamon et al with this sensor on various biological adlayers we found it interesting to make a thorough study of this waveguide structure for optimization of the sensor for a given detection purpose as it shows potential for detection of micronscale objects.

In this chapter the MCWG is presented for sensing purposes by explaining the sensing principle and a thorough study of the parameters in the structure comprising the MCWG is presented for optimization of the MCWG sensor. As one result of the study we have shown that the term coupled-plasmon waveguide resonator used by Salamon et al for the structure is actually incorrect. The structure does support waveguide modes and the sensing feature of the dip-type MCWG is exactly the excitation af waveguide modes in a dielectric layer of the structure.

What is the structure of a metal-clad waveguide?

A MCWG is a planar four-layered waveguide structure comprising a substrate S, a thin metal-cladding M, a dielectric waveguide film F and a cover medium C, with refractive indices and layer thicknesses n_I and d_I, respectively, see Fig. 4.1(a). The structure of the MCWG is thus similar to the conventional dielectric waveguide sensor but with an extra layer of metal introduced

between the substrate and the waveguide film. The MCWG can also be compared to the structure of an SPR-sensor. The difference between the two structures is that a waveguide film is added on top of the metal-coating for the MCWG structure. A photograph of a MCWG is shown in Fig. 4.1(b)

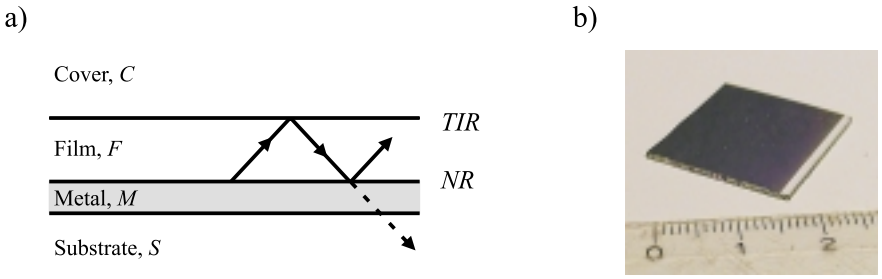

Figure 4.1. (a) Basic MCWG configuration with illustration of light guided in the waveguide film by total internal reflection (TIR) at the film/cover boundary and normal metallic reflection at the film/metal boundary. (b) Photograph of a fabricated MCWG.

What is the sensing principle?

Similar to the dielectric waveguide, light can be guided in the waveguide film of the MCWG. However, contrary to the dielectric waveguides, where the guided light experiences total internal reflection at both the film/cover- and the film/substrate-boundary the guided light in the MCWG is only totally internally reflected at the film/cover-boundary, while at the film/metal-boundary a normal reflectance (NR) of the light occurs where the light is partly transmitted into the metal-cladding and the substrate and partly reflected back into the waveguide film at the film/metal interface, illustrated in Fig. 4.1(a).

A waveguide mode arises when the reflected beams in the waveguide film experience constructive interference. Due to the reflection of the guided light in the waveguide film back into the film at both boundaries it is thus possible to excite a waveguide mode in the MCWG. As for the dielectric waveguides a waveguide mode arises when the wavefronts of the propagating light in the waveguide film are in phase, see Fig. 2.3. From the ray-tracing approach also used for the dielectric waveguide sensor a mode equation for the MCWG can be expressed as $2\pi m = \phi_{\Delta S} + \phi_{F,C} + \phi_{F,M,S}$, where the expressions for $\phi_{\Delta S}$ and $\phi_{F,C}$ are given in Eqs. (2.3) and (2.5). The phase shift of the light reflected at the film/metal/substrate boundary, $\phi_{F,M,S}$, is given by:[18, 19]

$$\phi_{F,M,S} = 2\tan^{-1}\left[i\left(\frac{1-r_{FM}}{1+r_{FM}}\right)\left(\frac{1-r_{MS}\exp[i2k_{z,M}d_M]}{1+r_{MS}\exp[i2k_{z,M}d_M]}\right)\right], \tag{4.1}$$

where r_{IJ} is the amplitude reflection coefficient between layers I and J.

The basic sensing principle of the MCWG is the same as for the dielectric waveguide: A change in n_C results in a change in $\phi_{F,C}$ which results in a change in $\phi_{\Delta S}$ for which a waveguide mode is excited. However, the operation of the MCWG is somewhat different from the dielectric waveguide sensors due to the metal cladding. MCWG sensors are operated in reflection mode, in which the waveguide structure is illuminated from below and the reflected intensity is measured. In Fig. 4.2 the operation of a MCWG-sensor is illustrated, when operated in reflection mode and prism-coupling of the light is used.

The MCWG is placed onto a prism with index-matched oil or the MCWG and the prism are incorporated in one unit by deposition of the metal layer and waveguide film directly onto the prism in which case the prism becomes the substrate. A cuvette is placed on top of the MCWG leaving an area of the sensor surface open for the cover medium, see Fig. 4.2(a). The cuvette has an inlet- and an outlet tube making it possible to change the cover medium. The MCWG is illuminated through the prism at an angle θ_S. The whole setup is placed on a rotation stage to vary the angle of incidence.

The measured reflectance vs. angle θ_S results in a sensorgram where a dip in reflectance occurs at the angle θ_m, where a waveguide mode is excited. The position of the dip in the sensorgram changes for a change in the cover medium RI, which is seen from Fig. 4.2(b) where the sensorgrams for a change in cover RI from n_{C1} to n_{C2} ($n_{C1} < n_{C2}$) for incident TE and TM polarized light are shown. The sensorgram can also be expressed as the reflectance vs. N, where $N = n_S \sin(\theta_S)$.

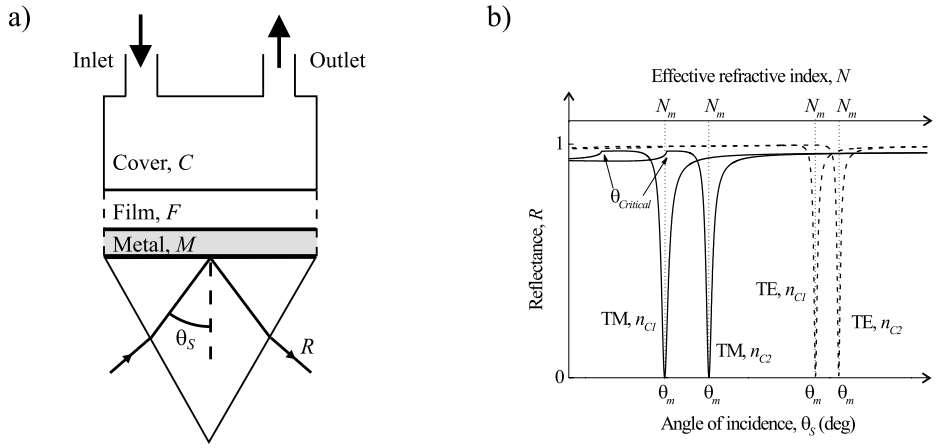

Figure 4.2. Operation of a prism-coupled MCWG sensor in reflection-mode. (a) The cover medium is applied to a cuvette on top of the MCWG. (b) The sensorgram from the MCWG for TE and TM polarized light when n_C is changed from n_{C1} = 1.33 to n_{C2} = 1.35. The RIs for the MCWGs are n_S = 1.517, n_M = 0.065 + i4 (silver), n_F = 1.59 and the thicknesses are d_F = 340 nm and d_M = 56 nm for TM polarized light and d_F = 250 nm and d_M = 43 nm for TE polarized light.

The sensorgrams, shown in Fig. 4.2(b) each show a dip in reflectance at the resonance angles of the TE and TM waveguide modes at N_m. Similar to the dielectric waveguides it is possible to excite waveguide modes in the MCWG with both TE and TM polarized light. It is seen that the reflectance increases as the angle of incidence is increased up to the critical angle $\theta_{Critical}$ which is given by $\sin^{-1}(n_C/n_S)$. The critical angle is the angle at which the light changes from being transmitted at the film/cover boundary to being totally internal reflected at this boundary, and thus at this angle $N = n_C$.

How can N_m be calculated for the MCWG?

Similar to the case of the dielectric waveguide, a waveguide mode equation for the metal-cladded structure can be derived from Maxwell's equations and the boundary conditions. Furthermore, for the prism-coupled MCWG the total reflectance can be calculated from Fresnell's reflection laws. The MCWG structure is a four-layer structure while the dielectric waveguide structures described in chapters 2 and 3 are three-layer structures and thus the waveguide equation Eq. (2.2) and the equation describing the Fresnell reflection of a layered structure Eq. (4.7) has to be expanded to include a four-layer waveguide structure and a possible adlayer.

The waveguide mode equation for the MCWG is derived similar to the waveguide mode equation for the dielectric waveguide from the solution ansatz Ω for the electromagnetic field in the four-layered structure based on the fields in the individual layers represented by plane waves with amplitudes A_I and B_I (I = C, M, F, C) for the up- and down-going waves, respectively, see Fig. 4.3.

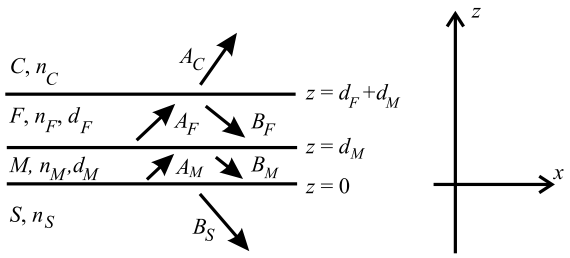

Figure 4.3. The amplitudes of electromagnetic field in a four-layered structure with a waveguide film of thickness d_F and metal layer thickness of d_M organized along the z-axis.

The solution ansatz Ω for the four-layered structure is given by:

$$\Omega = \left[\begin{array}{ll} B_S \exp[-ik_{z,S}z] \exp[ik_x x - i\omega t) & \text{(in the substrate)} \\ (A_M \exp[ik_{z,M}z] + B_F \exp[-ik_{z,M}z]) \exp[ik_x x - i\omega t) & \text{(in the metal),} \\ (A_F \exp[ik_{z,F}z] + B_F \exp[-ik_{z,F}z]) \exp[ik_x x - i\omega t) & \text{(in the film),} \\ A_C \exp[ik_{z,C}z] \exp[ik_x x - i\omega t) & \text{(in the cover)} \end{array} \right], \quad (4.2)$$

Applying the boundary conditions for the TE and TM polarized light six equations for each polarization are obtained and can be written in the form:

$$\mathbf{A}_\rho \psi = \mathbf{0}, \tag{4.3}$$

where ψ = (B_S, A_M, B_M, A_F, B_F, A_C) and $\mathbf{A}_\rho$ is given by:

$$\mathbf{A}_\rho = \begin{bmatrix} e^{i[\gamma_{CM}+\gamma_{CF}]} & -e^{i[\gamma_{FM}+\gamma_{FF}]} & -e^{-i[\gamma_{FM}+\gamma_{FF}]} & 0 & 0 & 0 \\ \frac{k_C}{n_C^{2\rho}} e^{i[\gamma_{CM}+\gamma_{CF}]} & -\frac{k_F}{n_F^{2\rho}} e^{i[\gamma_{FM}+\gamma_{FF}]} & \frac{k_F}{n_F^{2\rho}} e^{-i[\gamma_{FM}+\gamma_{FF}]} & 0 & 0 & 0 \\ 0 & e^{[i\gamma_{FM}]} & e^{[-i\gamma_{FM}]} & -e^{[i\gamma_{MM}]} & -e^{[-i\gamma_{MM}]} & 0 \\ 0 & \frac{k_F}{n_F^{2\rho}} e^{[i\gamma_{FM}]} & -\frac{k_F}{n_F^{2\rho}} e^{[-i\gamma_{FM}]} & -\frac{k_M}{n_M^{2\rho}} e^{[i\gamma_{MM}]} & \frac{k_M}{n_M^{2\rho}} e^{[-i\gamma_{MM}]} & 0 \\ 0 & 0 & 0 & 1 & 1 & -1 \\ 0 & 0 & 0 & \frac{k_M}{n_M^{2\rho}} & -\frac{k_M}{n_M^{2\rho}} & \frac{k_S}{n_S^{2\rho}} \end{bmatrix}, \tag{4.4}$$

where $\gamma_{IJ} = k_{z,I} d_J$ and $k_{z,I}$ is written as k_I.

The determinant of $\mathbf{A}_\rho$ is set equal to zero to obtain non-trivial solutions. The resulting equation is exactly identical to the one found from the ray-tracing approach and is restated here:

$$\begin{aligned} 2\pi m &= \phi_{\Delta S} + \phi_{F,C} + \phi_{F,M,S}, \\ \phi_{\Delta S} &= 2 k_{z,F} d_F, \\ \phi_{F,C} &= 2 \tan^{-1} \left[i \left(\frac{n_F}{n_C} \right)^{2\rho} \left(\frac{k_{z,C}}{k_{z,F}} \right) \right], \\ \phi_{F,M,S} &= 2 \tan^{-1} \left[i \left(\frac{1 - r_{FM}}{1 + r_{FM}} \right) \left(\frac{1 - r_{MS} \exp[i 2 k_{z,M} d_M]}{1 + r_{MS} \exp[i 2 k_{z,M} d_M]} \right) \right], \\ k_{z,I} &= \pm k \sqrt{n_I^2 - N_m^2}. \end{aligned} \tag{4.5}$$

From the mode equation above (Eq. (4.5)) $N_m = N'_m + iN''_m$ due to the complex value of the RI of the metal $n_M^2 = \epsilon_M = \epsilon'_M + i\epsilon''_M$. In Fig. 4.4 N'_m vs. film thickness is calculated for a silver- and a gold-MCWG, for TE and TM polarized light and for $m = 0 - 2$.

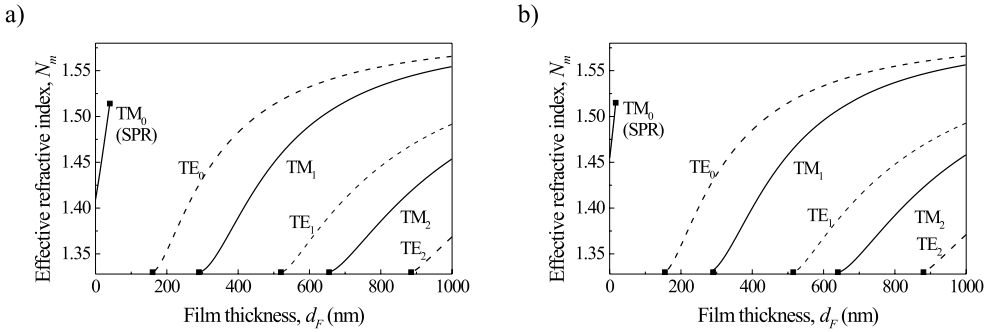

Figure 4.4. Calculated N'_m for a MCWG with silver cladding(a) and with gold cladding(b) for TE and TM polarized light. The parameters used are: n_S = 1.517, n_F = 1.59, n_C = 1.33, n_M = 0.065 + i4 (silver) and n_M = 0.15 + i3.2 (gold). The metal thicknesses of the waveguide structures are: d_M = 56 (TM, silver), d_M = 43 (TE, silver), d_M = 52 (TM, gold) and d_M = 40 (TE, gold). The squares indicate the film cutoff thicknesses for the different modes.

For the waveguide modes the value of N'_m is in the range between n_C and n_F, starting at n_C and increasing towards n_F for increasing film thickness. The film thickness at which $N_m = n_C$ is the cutoff film thickness indicated with squares in Fig. 4.4. The TM_0 mode which is the SPR-mode can be excited for very thin film thicknesses for both the silver- and gold-MCWG.

The mode equation for the four-layer MCWG structure can be extended to include an adlayer on the sensor surface by including the following expression to the 4-layer waveguide mode equation in Eq. (4.5):[19]

$$\phi_{d_A} = k\sqrt{n_F^2 - N_m^2}\left[d_A\left(\frac{n_A^2 - n_C^2}{n_F^2 - n_C^2}\right)\left(\frac{\left(\frac{N_m}{n_C}\right)^2 + \left(\frac{N_m}{n_A}\right)^2 - 1}{\left(\frac{N_m}{n_C}\right)^2 + \left(\frac{N_m}{n_F}\right)^2 - 1}\right)^{\rho}\right], \tag{4.6}$$

N_m can be determined indirectly from the position of the dip in the reflectance spectrum comprising a sensorgram measured from the MCWG sensor configuration. In general, the total reflectance from a layered structure can be calculated using Fresnell's reflection laws. For a three-layered structure of layers 1, 2 and 3 for which the lower(1) and upper(3) media are considered semi-infinite the reflectance is given by:[69]

$$R_{123} = |r_{123}|^2 = |\frac{r_{12}+r_{23}\exp[i2k_{z,2}d_2]}{1+r_{12}r_{23}\exp[i2k_{z,2}d_2]}|^2,$$
$$r_{IJ} = \frac{n_J^{2\rho}k_{z,I}-n_I^{2\rho}k_{z,J}}{n_J^{2\rho}k_{z,I}+n_I^{2\rho}k_{z,J}}, \quad k_{z,I} = k\sqrt{n_I^2 - N^2}, \quad k = \frac{2\pi}{\lambda}. \tag{4.7}$$

Here, r_{IJ} is the amplitude reflection coefficient between layers I and J, $k_{z,I}$ the normal wavevector component along z in medium I, n_I the RI of medium I, λ the light wavelength in vacuum and ρ is the polarization index that equals 0 for TE and 1 for TM polarized light

The reflectance from a four-layered structure can be calculated by expanding Eq. (4.7) to include a fourth layer. Replacing the reflection coefficient between layers 2 and 3 r_{23} by the reflection coefficient r_{234} and by using the appropriate indices for the layers, the reflectance from the four-layer MCWG structure is given by:

$$R_{SMFC} = |r_{SMFC}|^2 = \left|\frac{r_{SM} + r_{MFC}\exp[i2k_{z,M}d_M]}{1 + r_{SM}r_{MFC}\exp[i2k_{z,M}d_M]}\right|^2, \tag{4.8}$$

where r_{MFC} has the same form as r_{123} in Eq. (4.7) with appropriate indices. Hence, by continuing this recursive procedure the reflectance for an arbitrary number of layers can be found, thus an adlayer can be included by adding an additional layer in Eq. (4.8). The sensorgrams in Fig. 4.2 are calculated from Eq. (4.8).

Based on Eq. (4.8) the Fresnell reflectance of a MCWG with a silver cladding is plotted in Fig. 4.5 versus N for two film thicknesses d_F = 0 nm and d_F = 350 nm.

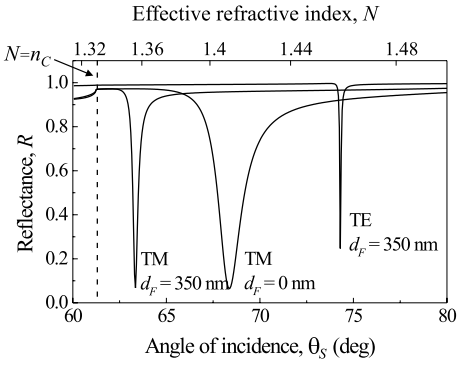

Figure 4.5. Calculated Fresnell reflectance for TE and TM polarized light (λ = 632.8 nm) from a MCWG with silver cladding. The refractive indices and thicknesses used are: n_S = 1.517, n_C = 1.33, n_M = 0.065 + i4 (silver), d_M = 50 nm, d_F = 0 nm and 350 nm.

In the absence of a film and for TM polarized light a dip in reflectance appears, this configuration is the SPR-configuration and thus the dip represents the SPR-mode. On the contrary, no reflectance dip appears for the TE polarized light in the absence of a film. However, applying a 350 nm

thick film on top of the metal layer, a much sharper dip is obtained for the TM polarized light and moreover, when the film is applied a very sharp dip appears for the TE polarized case too. The positions of the reflectance dips in N correspond to the mode resonances calculated from Eq. (4.5) for the following parameters:

d_F	m	ρ	N_m	comment
0	0	0 (TE)	-	-
0	0	1 (TM)	1.41	SPR mode
350 nm	0	0 (TE)	1.46	TE Waveguide mode
350 nm	1	1 (TM)	1.36	TM Waveguide mode

Table 4.1. Parameters for the waveguide modes mentioned in connection with Fig. 4.5

The modes arising when the 350 nm film is applied are waveguide modes TM($m = 1$) and TE($m = 0$). A SPR mode arises for the MCWG structure in the absence of a film when TM polarized light is incident on the structure. The waveguide modes are much sharper than the SPR-mode which is usually an advantage for determining the exact resonant angle.

Surface plasmons are TM waves which propagate along a metal/dielectric interface and surface plasmons can only be excited by TM polarized light incident on the interface. The propagating electromagnetic field at the metal/dielectric boundary is evanescent in both the dielectric and the metal layer.

In the MCWG-structure the metal/film boundary do support a surface plasmon for certain film RIs and this implies that a SPR-mode is generated here. However, the SPR-mode has a penetration depth limited to a few hundred nanometers and due to the waveguide film the SPR will only sense the RI of the waveguide film, when the film thickness is larger than the SPR penetration depth, hence the SPR-mode cannot be used for sensing purposes in the MCWG-structure. Thus, the term coupled-plasmon waveguide resonator used by Salamon et al for the structure is actually incorrect as the structure do support waveguide modes and the sensing feature of the dip-type MCWG is exactly the excitation af waveguide modes in a dielectric layer of the structure.

Why is the MCWG interesting for sensing purposes?

From Fig. 4.4 it is seen that $N_m = n_C$ at cutoff film thickness, which results in an infinite penetration depth in the cover for this film thickness as $d_{P,C}$ = Im[$k_{z,C}^{-1}$] = $k^{-1}\sqrt{N_m^2 - n_C^2}^{-1}$. The waveguide character of the MCWG gives the possibility of tuning the cover penetration depth by adjusting the film thickness, which is also seen from the expression for $d_{P,C}$ which decreases with N_m and from Fig. 4.4 it is seen that N_m' increases with d_F.

Which parameters are important for designing the dip-type MCWG?

When designing the MCWG sensor it is important to consider the purpose of the sensor; Should it be used for adlayer measurements or RI measurements? Moreover, the MCWG-chip includes three different materials, the substrate, the film and the metal cladding, where the RI of all three layers and the thicknesses of the film and the metal cladding influence on the optimum design for a specific sensing purpose. In the following the SPR-mode is also included for comparison of the sensitivity of the MCWG sensor.

For MCWGs several metals can be used for the metal-cladding, however for this configuration we have limited the study to include silver and gold claddings. The use of other metals will be discussed in the next chapter. For future reference to specify which metal is used for the cladding the metal symbol will be added to the MCWG-abbreviation, e.g. a MCWG with a silver cladding will be referred to as Ag-MCWG and with gold cladding Au-MCWG. The dielectric constants used for the metals are taken from reference [55]: ϵ_M (Au) = -10.22 + i0.96 and ϵ_M (Ag) = -16 + i0.52.

To explore the sensorgrams and the influence of the different layers of the MCWG a contour plot of the reflectance versus angle of incidence and metal thickness is calculated in Fig. 4.6 for five

different values of the film thickness. The contour plots are calculated from Eq. (4.8) for a Ag- and a Au-MCWG with both TE and TM polarized light.

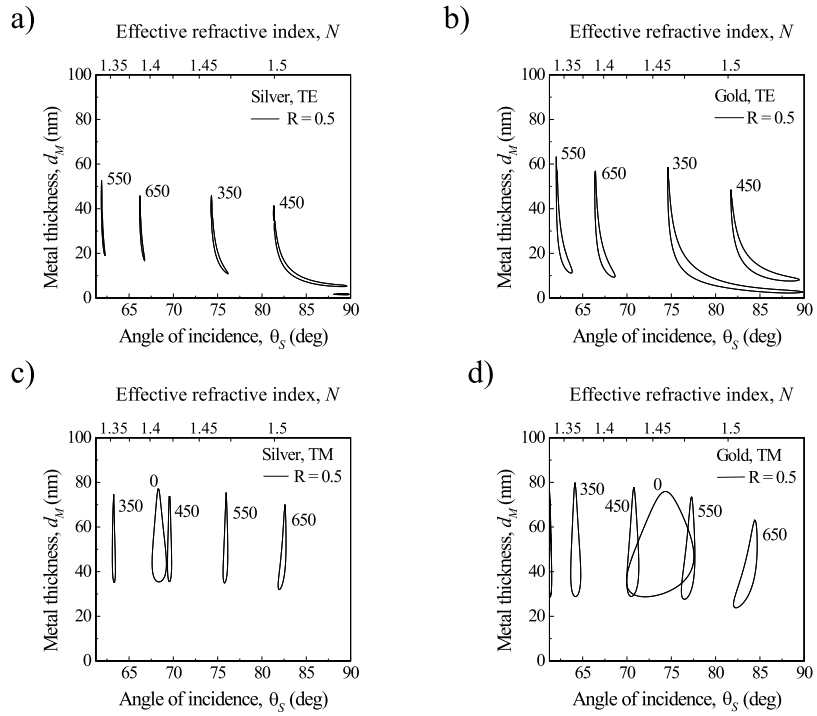

Figure 4.6. Contour plots of reflectance from Ag- and Au-MCWGs with a polystyrene film (n_F = 1.59), a glass substrate (n_S = 1.517) and a cover medium of n_C = 1.33. The contour lines represent reflectance, R = 0.5 and the numbers at the contours represent the film thickness in nanometers. The contours appearing for d_F = 0 represent SPR dips. (a) silver-cladding, TE-polarization, (b) gold-cladding, TE-polarization, (c) silver-cladding, TM-polarization and (d) gold-cladding, TM-polarization.

In Fig. 4.6 no contour line for $d_F = 0$ (SPR-configuration) appears for TE polarized light due to the characteristics of the surface plasmon.

From Figs. 4.6(c) and (d) (TM-polarization) it is seen that the angular position of the dip shifts nearly linearly with film thickness from d_F = 350 nm to d_F = 650 nm. From Figs. 4.6(a) and (b) (TE-polarization) the angular position of the dip shifts for an increase of d_F = 350 nm to d_F = 450 nm and again for d_F = 550 nm increased to d_F = 650 nm. The metal thickness does not affect the angular position much, but rather shows an optimum in terms of depth of the dip at around 30 nm for the TE-polarization and around 50 nm for the TM-polarization for both silver and gold claddings. In comparison, the contours for the SPR dips (d_F = 0) are plotted in the case of TM polarized light, showing broad dips and a dependence on d_M similar to that of the waveguide dips.

For the following study of optimization of the MCWG sensor the four-layer waveguide equation in Eq. (4.5) is used from which N_m is found, where $N_m = N_m' + iN_m''$ due to the complex dielectric

function of the metal. In that connection it is interesting to compare the solutions of the Fresnell reflection and the solutions from the mode equation in Eq. (4.5).

In Fig. 4.7 N_m' calculated from Eq. (4.5) is plotted (squares) together with the contour lines from Fig. 4.6. It is seen that the reflection dips appear when N of the incident light equals N_m' of the mode resonance. Here, the same independence of the metal thickness is observed. It is also seen, that N_m' approaches asymptotically a constant value when d_M exceeds 30-40 nm. This constant value is identical to the solution for N_m' obtained for the three-layer waveguide structure when the metal-layer is considered infinit. These solutions are illustrated by the dashed lines in Fig. 4.7.

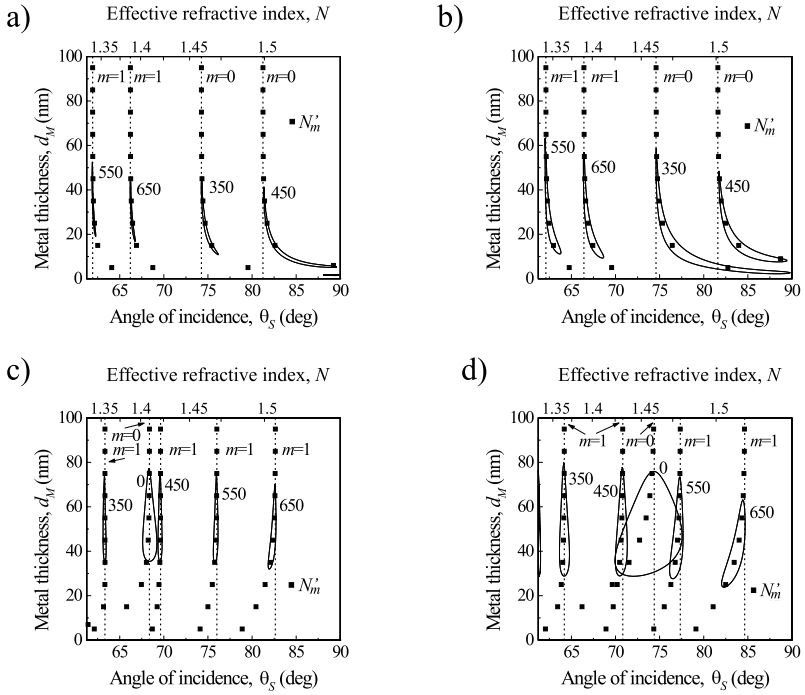

Figure 4.7. Calculated N_m' values (filled squares) for varying metal thickness of Ag- and Au-MCWGs obtained from the four-layer mode equation, Eq. (4.5). The contours are taken from Fig. 4.6 and the N_m' values represented by dotted lines are calculated from the three-layer mode equation, Eq. (2.2) for waveguides with metal-substrate and mode order m. (a) silver-cladding, TE-polarization, (b) gold-cladding, TE-polarization, (c) silver-cladding, TM-polarization and (d) gold-cladding, TM-polarization.

From Fig. 4.7 it appears that for the four-layer MCWG the three- and four-layer waveguide equations and the position of the dip in reflectance calculated from the Fresnell reflection results in the same solution for N_m' when d_M exceeds 30-40 nm. This means that the substrate has practically no influence on the electromagnetic field in the waveguide above that metal thickness. As a result, when optimizing the MCWG sensor geometry the three-layer expressions for the cover RI sensitivity and adlayer sensitivity in Eqs. (2.11) and (2.14) derived by Tiefenthaler and Lukosz can be used for these metal thicknesses, though keeping in mind the complex nature of N_m:

$$\frac{\partial N'_m}{\delta n_C} = \mathrm{RE}\left[\frac{n_C}{N_m}\frac{n_F^2 - N^2}{n_F^2 - n_C^2}\frac{d_C}{d_S + d_F + d_C}\left(2\frac{N^2}{n_C^2} - 1\right)\right], \quad (4.9)$$

$$\frac{\partial N'_m}{\delta d_A} = \mathrm{RE}\left[\frac{n_F^2 - N^2}{N(d_S + d_F + d_C)}\frac{n_A^2 - n_C^2}{n_F^2 - n_C^2}\left(\frac{(N/n_C)^2 + (N/n_A)^2 - 1}{(N/n_C)^2 + (N/n_F)^2 - 1}\right)^{\rho}\right]. \quad (4.10)$$

Furthermore, it is seen from Fig. 4.7 that the angular shift in dip position in Fig. 4.6(a) and (b) due to a change in d_F from 450 nm to 550 nm occurs because the waveguide mode TE_1 is excited when d_F is increased.

Is the type of metal and metal thickness not important?

The choice of metal and the thickness of the metal layer is important for the shape of the reflectance dip. In Fig. 4.8 calculated sensorgrams from Ag-MCWGs (a) and Au-MCWGs (b) with three different thicknesses of the metal cladding are shown.

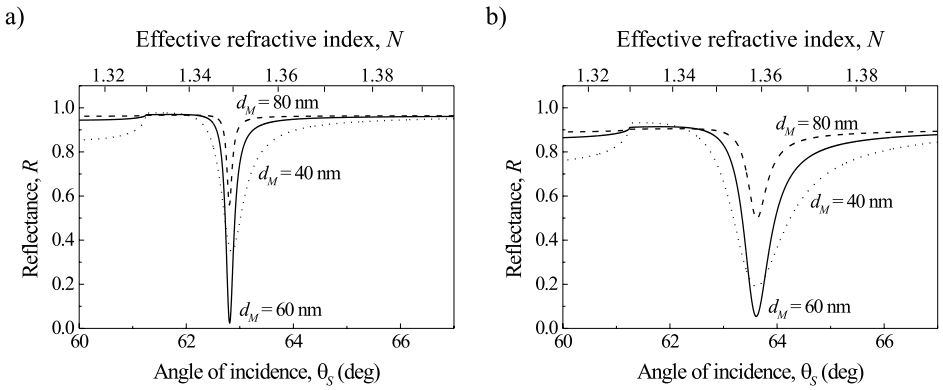

Figure 4.8. Reflectance spectra from Ag-MCWGs (a) and Au-MCWGs (b) with three different metal thicknesses d_M = 40 nm, 60 nm and 80 nm using TM polarized light. The parameters used are: n_S = 1.517, n_C = 1.33, n_F = 1.59, d_F = 350 nm, n_M = 0.065 + i4 (silver) and n_M = 0.15 + i3.2 (gold).

For both the Ag-MCWG and the Au-MCWG the position of the reflectance dip does not change with metal thickness, but the shape of the dip changes. At a metal thickness of 60 nm the reflectance approaches zero, when increasing d_M the minimum reflectance increases but the shape of the dip is more or less the same - the full-width-half-max (FWHM) is practically the same. Decreasing d_M also increases the minimum reflectance and the dip becomes broader (the FWHM increases). Thus the most notable dip in the sensorgram is obtained for the metal thickness resulting in a reflectance of zero and this thickness can be defined as the optimum metal thickness. Furthermore, it is seen from the sensorgrams that the reflectance dip from a Au-MCWG is broader than the dip for the Ag-MCWG.

From the literature it is known[18, 70] that the imaginary part of the metal permittivity ϵ''_M is responsible for the losses in MCWGs and thus it can be expected that sharp resonances (sharp dips) arise for MCWGs with small values of ϵ''_M and that the dips become less sharp when ϵ''_M is increased which is the case observed in Fig. 4.8, where ϵ''_M (Au) > ϵ''_M (Ag).

To explore the previous result of applying the three-layer mode equation to the MCWG-structure the reflectance minimum of a silver and gold MCWG is plotted versus film and metal thickness for 3 film RIs (a) 1.45, (b) 1.59 and (c) 1.75, see Fig. 4.9. The resonances are referred to as TM-SPR-AG for resonant mode excited with TM polarized light, surface resonance mode and silver cladding. WG refer to the waveguide modes.

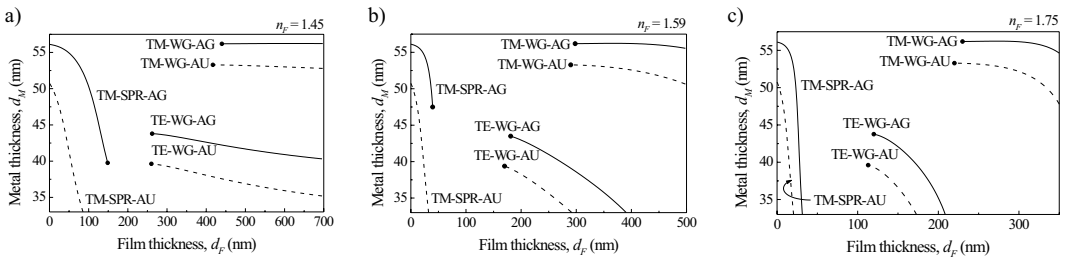

Figure 4.9. Calculated optimum metal thickness for a given film thickness where the Fresnell reflection is a minimum. The waveguide consists of a glass substrate (S), a metal layer (M), a waveguide film (F) and cover (C) with refractive indices: n_S = 1.517, n_M = 0.065+i4 (silver), n_M = 0.15+i0.32 (gold), n_C = 1.33 and three RIs of the waveguide film (a) n_F = 1.45, (b) n_F = 1.59 and (c) n_F = 1.75.

It is seen that the optimum metal thickness for the SPR-modes drops rapidly with the film thickness, whereas the waveguide modes exhibit a weaker dependence. Another interesting feature is that the optimum metal thicknesses at cutoff are independent on the film RI. This reconfirms the use of the three-layer mode equation for sensitivity calculations.

What is the influence of the WG-film?

The thickness of the waveguide film has a big influence on the angular position of the resonant dip as seen from Fig. 4.7. Moreover, it is seen from Fig. 4.9 that both the RI and thickness of the waveguide film influence the waveguide modes of the MCWGs. It is seen that the cutoff film thickness, which is the thinnest film at which a given mode can be excited in the waveguide, changes with n_F. Decreasing n_F increases the cutoff thickness, and the RI of the waveguide film can be said to squeeze the sensorgram in angles.

The influence of the waveguide film thickness on the sensitivity is explored in Fig. 4.10 where the cover RI sensitivities and adlayer sensitivities calculated from Eqs. (4.9) and (4.10) are plotted against film thickness for both TE and TM polarized light, for SPR and waveguide modes, and for silver and gold substrates. From Fig. 4.10(a) it is seen that the maximum cover RI sensitivities of 1 for the MCWG are achieved at the cut-off film thickness and decrease with increasing film

thickness. The maximum adlayer sensitivity for the MCWG is on the other hand obtained at a film thickness around 50 nm thicker than the cut-off film thickness; this is in line with sensitivities calculated for the reverse symmetry waveguide.

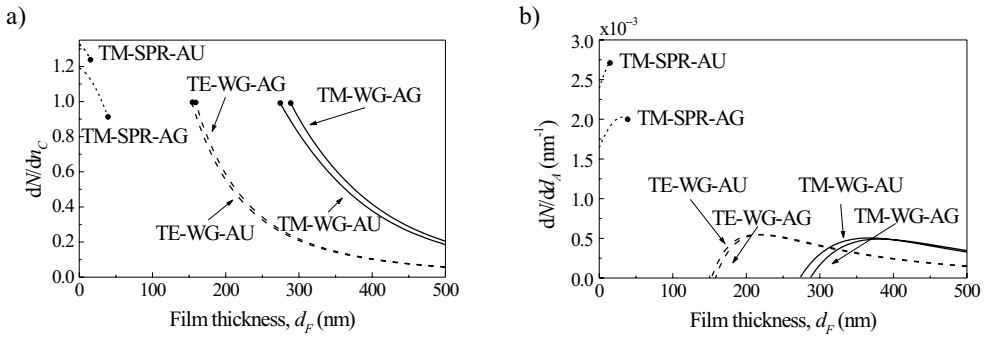

Figure 4.10. Calculated cover RI sensitivities $\partial N/\partial n_C$ (a) and adlayer sensitivities $\partial N/\partial d_A$ (b) for silver and gold substrate MCWG using following parameters: n_S = 1.517, n_M = 0.065+i4 (silver), n_M = 0.15+i0.32 (gold), n_C = 1.33, n_F = 1.59 and for the adlayer in (b) n_A = 1.5.

However, it is seen from Fig. 4.10(a) that a cover index sensitivity of up to 1.3 can be achieved for the TM-SPR-AU mode without film, which is slightly above the maximum waveguide sensitivities of 1. Similarly, in Fig. 4.10(b) it is seen that the maximum adlayer sensitivity is obtained for the TM-SPR-AU mode showing 4-5 times higher sensitivity than the maximum MCWG mode sensitivities. Interestingly, the highest sensitivities for the SPR modes are found when a very thin film of 20-40 nm is applied.

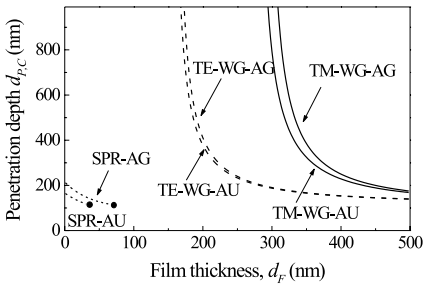

Figure 4.11. Calculated cover penetration depth for silver and gold substrate MCWG using the same parameters as in Fig. 4.10.

In Fig. 4.11 the penetration depth of the evanescent field in the cover $\mathrm{Im}[k_{z,C}]^{-1}$, is calculated versus film thickness. It is seen that the penetration depths of the waveguide modes are infinite at the cutoff points, thus the calculated penetration depths offer a logical explanation for the adlayer

and cover RI sensitivities. For a high penetration depth of the evanescent field a thin adlayer will not contribute significantly to the average sensed RI of the cover medium. Increasing the film thickness and thus decreasing the penetration depth results in increased influence of the adlayer on the sensed cover medium.

The penetration depth of the waveguide modes are quite different from the SPR modes, where the penetration depths are limited to a depth of 200 nm. This means that the MCWGs are well suited for the detection of larger biological objects such as bacteria and eukaryotic cells. These features are similar to those of the reverse symmetry waveguide.

The findings in Fig. 4.10 are nicely confirmed in Fig. 4.12, where pairs of reflectance curves illustrate the shifts in dip position due to small changes in n_C and d_A, respectively. Indeed, the shifts of the SPR modes exceed those of the WG modes. However, Fig. 4.12 also reveal another important sensor issue, namely that the width of the dips are much larger for the SPR modes compared with the waveguide dips [note: different angular scales]. This feature is just as important in optimizing the waveguide sensor. Finally, as described earlier also the depth of the dip which is dependent on the metal thickness is an important parameter.

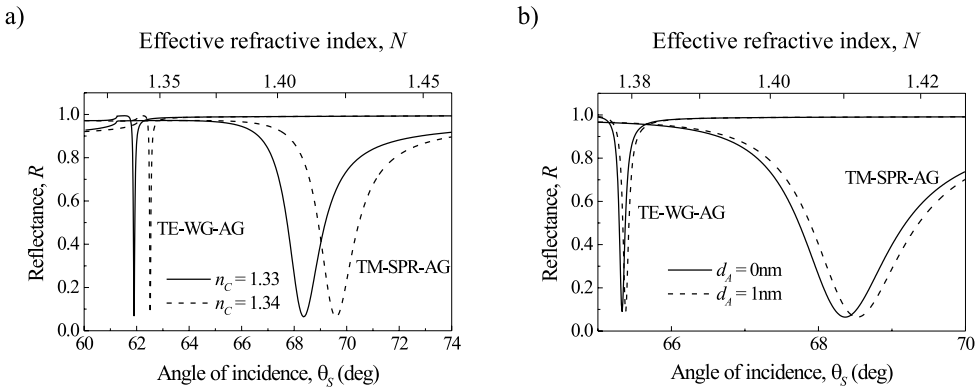

Figure 4.12. Calculated Fresnell reflectance off a 50 nm Ag-MCWG for the TM-SPR and the TE-WG mode to illustrated the change in angular position of the reflectance dip due to a change in n_C (a) and d_A (b) [note: different angular scales]. The parameters used are the same as for the Ag-MCWG in Fig. 4.10 but with a substrate of n_S = 1.517. For the adlayer n_A = 1.5, d_A = 0 nm and d_A = 1 nm are used.

Based on Fig. 4.12, we now plot new sensitivity curves, this time normalized by the FWHM of the reflectance dip and for every film thickness ensuring that the optimum metal thickness from Fig. 4.9 is used. The results are shown in Figs. 4.13 and 4.14 representing the normalized cover-RI and adlayer sensitivities, respectively. What is found is that both the normalized cover-RI sensitivity and adlayer sensitivity for the waveguide modes are highest at cutoff film thickness and for the

SPR modes the sensitivities are largest when no film is applied. This is contrary to the adlayer sensitivities calculated in Fig. 4.10(b), where the FWHM of the dips were not considered.

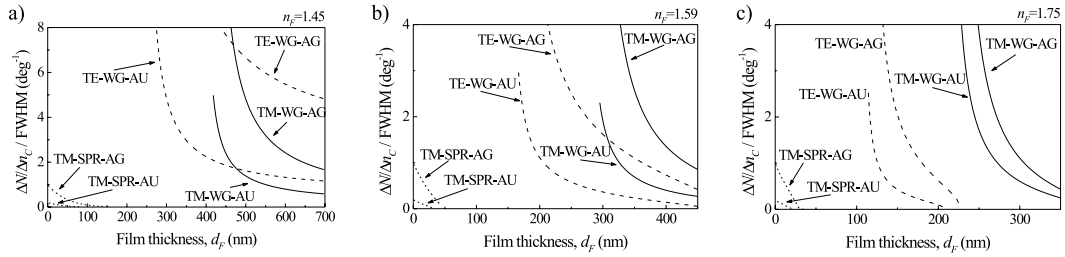

Figure 4.13. Calculated normalized cover RI sensitivity for silver and gold cladded waveguides with three different RIs of the film using the Fresnell reflection coefficients taking into consideration the FWHM of the dips. The RIs used are: n_S = 1.517, n_C = 1.33, n_M = 0.065 + i4 (silver) and n_M 0.15+i3.2 (gold).

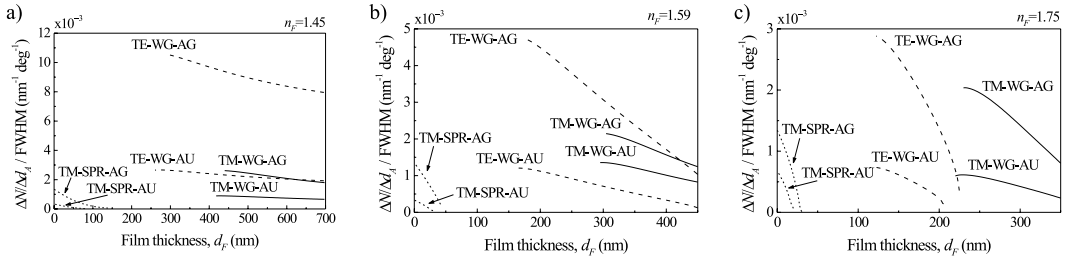

Figure 4.14. Calculated normalized adlayer sensitivity for silver and gold cladded waveguides with three different RIs of the film using the Fresnell reflection coefficients taking into consideration the FWHM of the dips. The RIs used are: n_S = 1.517, n_C = 1.33, n_M = 0.065 + i4 (silver) and n_M 0.15+i3.2 (gold).

Generally, it is possible to achieve both a higher normalized cover RI and adlayer sensitivity for the waveguide modes than for the SPR modes. In Figs. 4.13 and 4.14 it is seen, that the normalized sensitivity of the waveguide modes are highly dependent on the film RI, in the case of low film RI the normalized cover-RI sensitivity of the waveguide modes are higher than that of the SPR modes over a wide range of film thicknesses, while for high RI film the normalized cover RI sensitivity of the waveguide modes decreases very rapidly and falls below that of the SPR modes when the film thickness is 30-40 nm above cutoff thickness (for n_F = 1.75). For the normalized adlayer sensitivity for low film RI the waveguide modes have a higher sensitivity than the SPR modes over the entire range of film thickness shown in Fig. 4.14(a). Increasing the film RI the normalized sensitivity of the waveguide modes at cutoff film thickness decreases and approaches the sensitivity of the SPR modes.

To obtain both a large normalized cover-RI and adlayer sensitivity for the waveguide modes a low RI film should be chosen. In this case the normalized sensitivity of the waveguide modes can be improved 10 times compared to that of the SPR.

When the light is only reflected at one boundary, is it possible to have a waveguide mode?

A waveguide mode is characterized by constructive interference in the waveguide film of the reflected light at the boundaries back into the film resulting in a profile of the guided field with at least one maximum in field intensity in the film. Thus a waveguide mode can arise even with light being normally reflected, these waveguide modes are referred to as leaky waveguide modes. For the MCWG the profile of the electromagnetic field can be calculated in line with the procedure for calculating the mode profile for the dielectric waveguide. However, for the MCWG the incident light is applied in the substrate and thus the solution ansatz Ω for the four-layer MCWG in Eq. (4.4) is extended to include an incident field in the substrate with amplitude $A_S = 1$.

$$\begin{bmatrix} e^{i[\gamma_{CM}+\gamma_{CF}]} & -e^{i[\gamma_{FM}+\gamma_{FF}]} & -e^{-i[\gamma_{FM}+\gamma_{FF}]} & 0 & 0 & 0 \\ \frac{k_C}{n_C^{2\rho}} e^{i[\gamma_{CM}+\gamma_{CF}]} & -\frac{k_F}{n_F^{2\rho}} e^{i[\gamma_{FM}+\gamma_{FF}]} & \frac{k_F}{n_F^{2\rho}} e^{-i[\gamma_{FM}+\gamma_{FF}]} & 0 & 0 & 0 \\ 0 & e^{[i\gamma_{FM}]} & e^{[-i\gamma_{FM}]} & -e^{[i\gamma_{MM}]} & -e^{[-i\gamma_{MM}]} & 0 \\ 0 & \frac{k_F}{n_F^{2\rho}} e^{[i\gamma_{FM}]} & -\frac{k_F}{n_F^{2\rho}} e^{[-i\gamma_{FM}]} & -\frac{k_M}{n_M^{2\rho}} e^{[i\gamma_{MM}]} & \frac{k_M}{n_M^{2\rho}} e^{[-i\gamma_{MM}]} & 0 \\ 0 & 0 & 0 & 1 & 1 & -1 \\ 0 & 0 & 0 & \frac{k_M}{n_M^{2\rho}} & -\frac{k_M}{n_M^{2\rho}} & \frac{k_S}{n_S^{2\rho}} \end{bmatrix} \times \begin{bmatrix} A_C \\ A_F \\ B_F \\ A_M \\ B_M \\ B_S \end{bmatrix} = \begin{bmatrix} 0 \\ 0 \\ 0 \\ 0 \\ 1 \\ \frac{k_S}{n_S^{2\rho}} \end{bmatrix}, \tag{4.11}$$

where $\gamma_{IJ} = k_{z,I} d_J$ and $k_{z,I}$ is written as k_I.

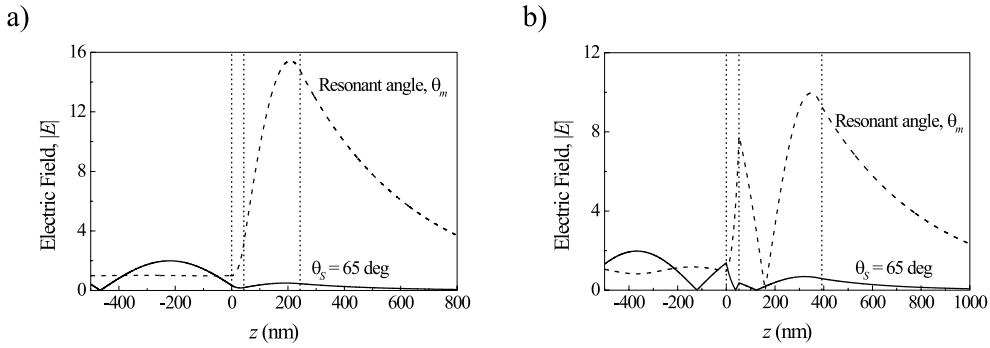

Figure 4.15. Profile of the electromagnetic field propagating in a Ag-MCWG at resonant angle (solid line) and at an angle off resonance θ_S = 65 deg (dashed line) for TE (a) and TM (b) polarized light. The parameters used are: n_S = 1.517, n_M = 0.065 + i4, n_F = 1.59 and n_C = 1.33. The film and metal thicknesses of the configurations are: (a) d_M = 43 nm, d_F = 200 nm and (b) d_M = 56 nm, d_F = 340 nm.

The mode profile in Fig. 4.15(a) for TE polarized light at resonant angle θ_m shows that a waveguide mode is obtained in the waveguide film and a large evanescent field extends into the cover. The field is strongly damped through the metal layer, resulting in a field amplitude in the substrate basically equal to one which is the field amplitude of the incident light and thus a reflectance from the structure that is basically zero. For an angle of the incident light off resonance angle θ_S = 65 deg, for which the reflectance from the sensorgram is close to one, the field profile in the structure is calculated showing a field amplitude in the substrate changing from 0 to 2 due to interference of the incident light and reflected light at the substrate/metal interface showing that the major part of the incident field with amplitude one is reflected back into the substrate at the substrate/metal interface. A small part of the light is transmitted to the film where a small evanescent field arises in the cover due to TIR.

For the TM polarized case in Fig. 4.15(b) the electromagnetic field is also calculated at resonant angle and at an angle off resonance θ_S = 65 deg. For the TM polarized light $m = 1$ for the film thickness, d_F = 340 nm and a field with two max amplitudes arises in line with the field amplitude for m = 1 in a dielectric waveguide. As for the TE polarized case a large evanescent field arises in the cover and the field in the metal layer is strongly damped through the metal layer away from the film/metal interface through the metal resulting in a small part of the field leaking into the substrate and a reflectance from the substrate/metal interface which is basically zero. At the angle off resonance the major part of the incident light is reflected and as seen from the TE polarized case, the part of the light transmitted into the metal is strongly damped through the metal but with a part of the field coupling to the metal/film boundary and into the film resulting in a small evanescent field extending into the cover medium.

Is the detection range limited?

The detection range of the dip-MCWG is limited due to the change in critical angle $\theta_{Critical}$, which changes with n_C. The change in $\theta_{Critical}$ is larger than the change in the dip position which the result that when n_C is increased to a given value a waveguide mode can no longer be excited. In Fig. 4.16 the reflectance curves from a Ag-MCWG with a film thickness larger than the cutoff film thickness is plotted for changes in n_C from 1.33 up to 1.41.

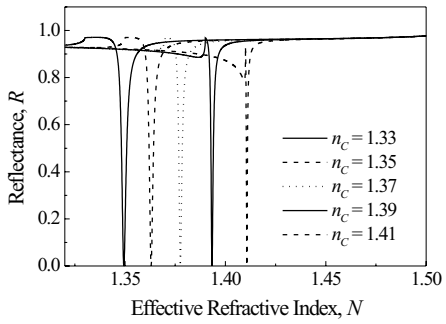

Figure 4.16. Sensorgrams from a Ag-MCWG with five different cover RIs with incident TM polarized light and λ = 632.8 nm. The parameters used are: n_S = 1.517, n_M = 0.065 + i4, d_M = 56 nm, n_F = 1.59, d_F = 340 nm and cover RIs n_C = 1.33, 1.35, 1.37, 1.39 and 1.41.

From Fig. 4.16 it is seen that for n_C = 1.41 the critical angle and the resonant dip are barely separated and the limiting parameter of the detection range is the thickness of the waveguide film. However, it should be remembered that the penetration depth (Fig. 4.11) changes depending on d_F and thus a trade off between detection range and $d_{P,C}$ exists when designing the MCWG.

Can the sensor be used for detection of both gasses and aqueous solutions?

The fields of application for the dip-type MCWG include measurements of gases as well as aqueous solutions by adjusting the film thickness. In that connection it should be noted that the upper detection limit is given by n_S. In Fig. 4.17 the cover penetration depth is calculated vs. n_C for five different film thicknesses for a Ag-MCWG with incident TE (a) and TM (b) polarized light,

where no waveguide mode can be excited for TE polarized light for a configuration with d_F = 0 nm.

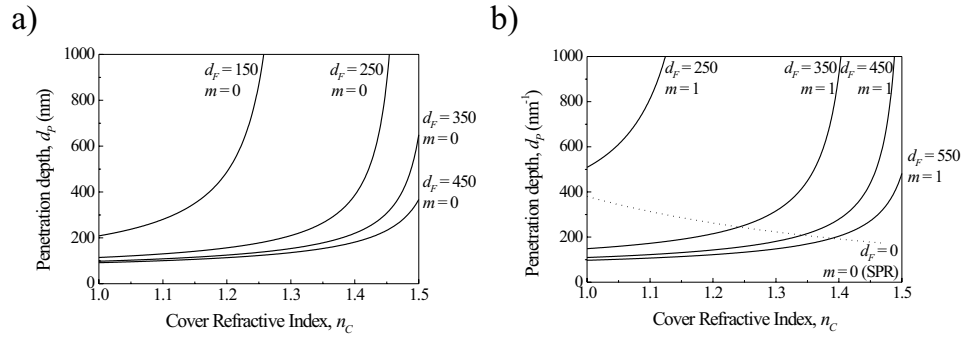

Figure 4.17. Cover penetration depth for a Ag-MCWG with five different film thicknesses vs. n_C for incident TE (a) and TM (b) polarized light with λ = 632 nm. The parameters used are: n_S = 1.517, n_M = 0.065 + i4 (Ag), n_F = 1.59 and metal thicknesses d_M = 43 nm (a) and d_M = 56 nm (b).

From Fig. 4.17 it is seen that the penetration depth increases with n_C. This is due to the different rates of increase of the angular position of the critical angle and of θ_m. The position of the critical angle changes with the highest rate of the two, resulting in the cutoff film thickness being increased. Thus the film thickness should be chosen according to the RI of the cover medium to be measured and in consideration of the purpose of the measurements. The penetration depth should be increased for detection of micronscale biological objects and for RI measurements of solutions, while for thin adlayers the penetration depth should be limited to the adlayer thickness.

The cover RI and adlayer sensitivities are calculated vs. n_C in Figs. 4.18 and 4.19, respectively for the same MCWG configurations as used for the $d_{P,C}$ calculations shown in Fig. 4.17 and for TE and TM polarization.

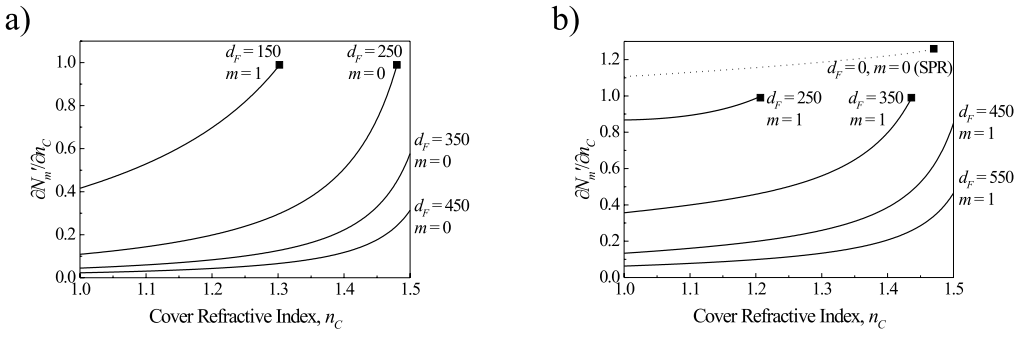

Figure 4.18. Cover RI sensitivity for a Ag-MCWG with five different film thicknesses vs. n_C for incident TE (a) and TM (b) polarized light with λ = 632 nm. The parameters used are: n_S = 1.517, n_M = 0.065 + i4, n_F = 1.59 and metal thicknesses d_M = 43 nm (a) and d_M = 56 nm (b).

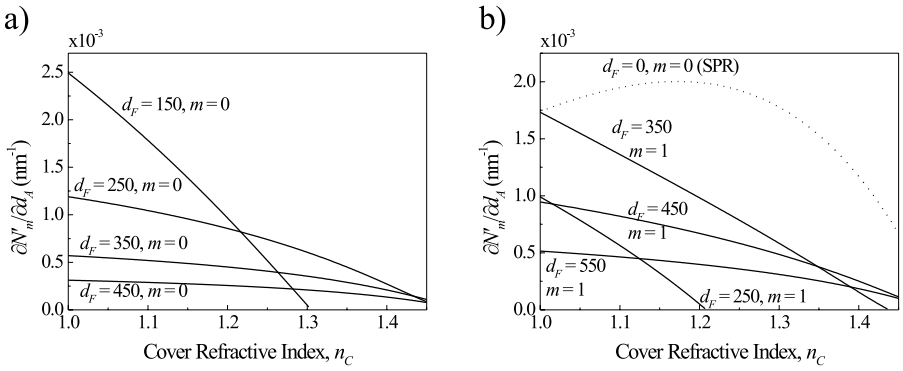

Figure 4.19. Adlayer sensitivity for a Ag-MCWG with five different film thicknesses vs. n_C for incident TE (a) and TM (b) polarized light with λ = 632 nm. The parameters used are: n_S = 1.517, n_M = 0.065 + i4, n_F = 1.59, metal thicknesses d_M = 43 nm (a)andd_M = 56 nm (b) and for the adlayer (b) n_A = 1.5 and d_A = 1 nm have been used.

The sensitivities in Figs. 4.18 and 4.19 are not normalized with the FWHM but they illustrate that the optimum film thickness of the MCWG configuration differs for adlayer and cover RI measurements. An increase in the film thickness expands the detection range with a cover RI sensitivity $\partial N_m/\partial n_C$ = 1 for the maximum n_C of the detection range and decreasing sensitivity with decreasing n_C. Contrary, the adlayer sensitivity $\partial N_m/\partial d_A$ = 0 for the maximum n_C of the detection range and increases with decreasing n_C. Due to the change in penetration depth with n_C the adlayer has the maximum influence on N_m for small values of n_C due to the smaller penetration depth.

For which detection purposes are the application of the MCWG an advantage?

The advantage of the MCWG is that an infinite cover penetration depth can be achieved at the cutoff film thickness and thus the sensor becomes suitable for detection of micronscale biological objects as cells and bacteria. However, the cover penetration depth can be tuned by adjusting the film thickness and thus the MCWG can also be applied for measurements of thinner adlayer thicknesses, with a normalized adlayer sensitivity of the MCWG that exceeds the normalized adlayer sensitivity of the SPR sensor.

4.1 Discussion

The sensor properties of the dip-MCWG can be optimized in terms of achieving the largest shift in the reflectance dip vs. FWHM of the dip. To achieve this, it is not sufficient to consider the usual sensitivity parameters (cover RI sensitivity) and (adlayer sensitivity), as these do not take into account the shape of the sensorgram (dip shape). Instead, our optimization procedure is based

simply on Fresnell's reflection law for the four-layer structure (substrate-metal-film-cover) from which the dip-angle-change per dip-width to the change in cover-RI or adlayer thickness can be deduced directly.

If the dip shape is not taken into account, the surface-plasmon resonance (SPR) sensor (equivalent to MCWG sensor without dielectric film) generally exhibits the largest sensitivity, but taking into account the width of the dip, there is a clear benefit of applying a waveguide film on top of the metal layer, simply because of the much narrower waveguide dip. These benefits apply to refractometry applications (cover RI measurements) as well as adlayer detection.

With respect to adlayer detection, which is the most interesting for biosensing applications, the main experiences gained from our investigations of optimized sensitivity can be summarized as follows:

- The film RI should be as low as possible.
- The optimum film thickness is close to the mode's cutoff thickness.
- Silver cladding is preferable to gold-cladding, mainly due to a narrower dip.
- The optimum metal layer thickness does not depend on the film RI. For a light wavelength of 632.8 nm and optimum film thickness they are 56, 53, 44, and 40 nm for TM-silver, TM-gold, TE-silver, and TE-gold modes, respectively.
- The dependence on substrate RI is practically non-existing, because at optimum metal thicknesses the mode's evanescent field is vanishing in the substrate.
- As opposed to SPR detection, the dip-MCWG detection has the possibility of utilizing both TE and TM polarized light, however, the largest adlayer sensitivity is obtained for TE polarized light.
- For a film RI of 1.45 the sensitivity improvement compared with Ag-SPR sensing is approximately a factor of 6.

The dip-type MCWG can be tuned to obtain either a low or a high penetration depth by adjusting the film parameters and thus the sensor can be used for measurements on both thin adlayer and micronscale objects. The sensor can be operated in multimode operation or supporting both a TE- and TM-mode resulting in modes with different penetration depths in the cover, giving a sensor that can measure at different depths in the cover medium. Thus the MCWG has the same advantages as the reverse symmetry dielectric waveguide. Contrarily, for the SPR sensor it is not possible to tune the penetration depth, which basically is fixed over the whole detection range and does not change significantly between a silver- and a gold-cladding.

It should finally be noted that the MCWG offers an additional advantage to the SPR-device as the waveguide film provides a chemical and mechanical shield to the metal layer.

Chapter 5

Metal-clad peak-type waveguide sensors - Theory

Metal-clad waveguides (MCWGs) were introduced in the previous chapter. MCWGs can be configured in two ways related to two different modes of operation: A dip-type operation which was described in the previous chapter (dip-type MCWG) and a peak-type operation (peak-type MCWG) which is introduced in this chapter.

The peak-type MCWG was introduced in the literature in 2003 by Zourob et al [27] as a metal clad leaky waveguide sensor (MCLW) for chemical and biosensing applications. The group has used this sensor for detection of protein layers and bacteria on the sensor surface and applied the sensor for RI-measurements of aqueous solutions,[27, 28, 71, 72] and shown the sensor's potential for detection of micronscale objects on the sensor surface.

However, the group has only presented a few configurations of the sensor and no theoretical study of the impact of the various parameters involved in the sensor configuration has been made. Due to the fact that the sensor has potential for detection of micronscale objects, we have conducted a thorough study of the sensor configuration with the aim of optimizing the sensor for deep-probe measurements. In this chapter the sensor operation will be presented along with a thorough discussion of the parameters influencing the sensor performance.

The basic properties described for the dip-type MCWG also apply for the peak-type MCWG and thus references to the previous chapter will occur frequently.

What is the configuration of the peak-type MCWG?

The configuration of the peak-type MCWG is the same as for the dip-type MCWG comprising a four-layer planar structure of a substrate (S), a metal layer (M), a waveguide film (F), and a cover medium (C), see Fig. 5.1(a). However, the metal to be used for the metal layer should (I) have a dielectric constant ($\epsilon_M = \epsilon'_M + i\epsilon''_M$) for which the imaginary part ϵ''_M has a high value and (II) the metal thickness should be about an order of magnitude smaller.

What is the sensing principle?

The peak-type MCWG is operated in reflection mode and a prism-coupled setup illustrated in Fig. 5.1(a) is used, exactly like the setup used for the dip-type MCWG. However, the measured sensorgram of reflectance vs. angle θ_S or N shows a peak in reflectance. In Fig. 5.1(b) the sensorgrams from a peak-type MCWG are shown for cover medium RIs of n_C = 1.33 and n_C = 1.35.

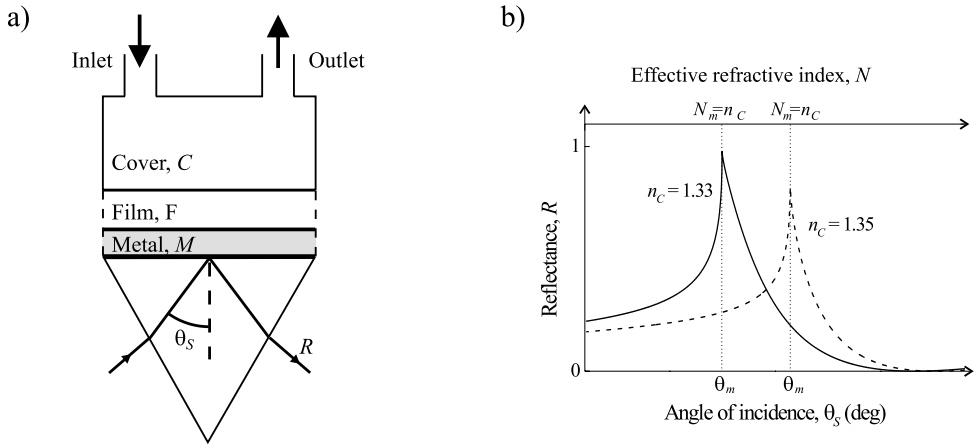

Figure 5.1. Operation of a prism-coupled peak-type MCWG sensor in reflection-mode. The sensor is placed on the prism and a cover medium is applied to a cuvette on top of the MCWG. (b) The sensorgrams from the peak-type MCWG for TE polarized light ($\lambda = 632.8$ nm) when n_C is changed from 1.33 to 1.35. The materials used are: Glass substrate (n_S = 1.517), titanium for the metal layer (n_M = 2.11 + i2.88, d_M = 5 nm) and a SiO_2 waveguide film (n_F = 1.47, d_F = 240 nm).

The angle and the effective RI N for which the peak arises will be referred to as θ_m and N_m, in line with the notation used for the previous sensors. From the sensorgrams it is seen that the angular position of the peak θ_m or the value of N_m for which the peak is observed changes when n_C is changed. The sensing principle for the peak-type MCWG is thus to detect the change in peak position and thus, contrary to the dip-type MCWG where the sensing feature is a dip the sensing feature for this MCWG is a peak, hence the illustrative names of the two types of sensors.

Why does the peak in reflectance appear?

The peak in reflectance is positioned exactly at the critical angle $\theta_{Critical} = \arcsin(n_C/n_S)$, and the peak arises due to two phenomena occurring: from the low angle side the reflectance increases to 1 at $N = n_C$ (critical angle) due to TIR, whereas from the high angle side a broad resonance drags the reflectance down to zero. Together this leaves a peak at $\theta_S = \theta_{Critical}$.

In Fig. 5.2 the calculated reflectance profile for a purely dielectric three-layer structure is shown (squares, $d_M = 0$). The structure comprises a glass substrate, a silica film and an aqueous cover medium and TIR appears at the film/cover interface when the effective refractive index exceeds the cover RI. Introduction of a 5 nm thin titanium layer with dielectric constant $\epsilon_M = 2.11 + i2.88$ between the substrate and film changes the reflectance profile from the structure remarkably. The

TIR line is replaced by a significant, broad dip in the reflectance. The dip in reflectance above the critical angle arises due to excitation of a waveguide mode in the waveguide film.

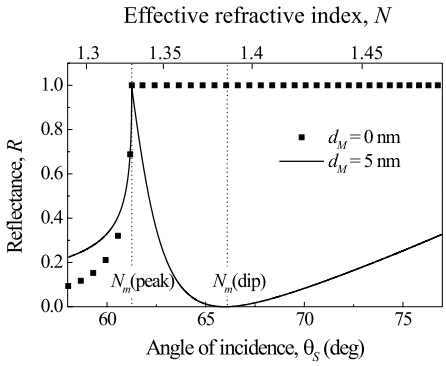

Figure 5.2. Calculated reflectance from a waveguide with and without a metal layer. The light is TE polarized, with wavelength λ = 632.8 nm. The waveguide parameters are: n_S = 1.517, n_M = 2.11 + i2.88, n_F = 1.47 and n_C = 1.33. The film and metal thicknesses are d_F = 240 nm and d_M = 5 nm.

From the literature it is known that the imaginary part of the metal permittivity ϵ''_M is responsible for the losses in MCWGs and thus it can be expected that sharp resonances (sharp dips) arise for MCWGs with small values of ϵ''_M and vice versa, which is also seen by comparison of the dips from a Ag-MCWG and the Ti-MCWG in Figs. 4.8 and 5.2, respectively.

Can the peak-type MCWG be analyzed in the same way as the dip-type?

For the peak-MCWG it is not possible to conduct a theoretical optimization of the sensor configuration in the same way as of the dip-type as the peak arising in the sensorgram is not a waveguide mode but instead is a result of a waveguide mode being excited in the waveguide film at an angle in the vicinity of the critical angle.

However, the parameters for the peak-type MCWG should be chosen according to which measurements the sensor is applied for and also to optimize the shape of the peak for better detection of the peak in the sensorgram for future automatic analysis of the sensorgram.

Even though there is a phenomenological difference in the sensing feature of the two types of MCWGs the reflectance from the peak-type MCWG can be calculated using the Fresnell reflection laws in the same ways as for the dip-type MCWG using Eq. 4.8.

What is the influence of the WG-film for this sensor?

The thickness of the waveguide film is important and should be above the cutoff film thickness in order for a waveguide mode to be excited. In Fig. 5.3 the sensorgrams from a Ti-MCWG are calculated for three different film RIs (a) and three different film thicknesses (b), respectively. The

influence of the waveguide film for the peak-MCWG is the same as for the dip-MCWG, increasing d_F or n_F increases the angular position of the resonant dip, as seen from Fig. 5.3. The important criteria for the waveguide film is that the thickness is chosen above cutoff film thickness but still thin enough to make sure that the critical angle appears within the range of the reflectance dip to obtain the distinct peak, which is seen in Fig. 5.3(a) for n_F = 1.51 and (b) for d_F = 280 nm, respectively, where the angular distance between the critical angle and the resonant angle of the excited waveguide becomes too large and thus a "soft" peak appears rather than the sharp peak observed for in the four other sensorgrams. The soft peak is not useful for the same sensing operation as the sharp peak as it is the position of the peak at the critical angle which is the sensing feature.

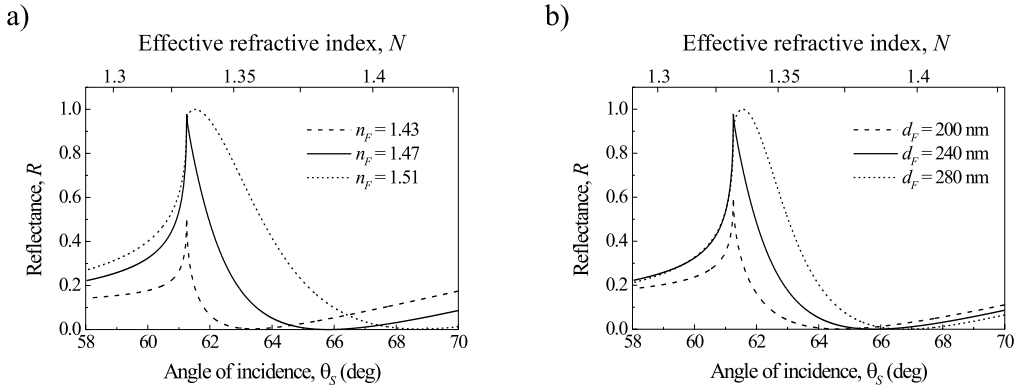

Figure 5.3. Sensorgrams from a Ti-MCWG for a three different film RIs n_F (a) and for three different film thicknesses d_F (b). The parameters used are: (a) n_S = 1.517, d_F = 240 nm, d_M = 5 nm, ϵ_M = 2.11 + i2.88, n_C = 1.33 and n_F = 1.43, 1.47 and 1.51, (b) n_S = 1.517, n_F = 1.47 nm, d_M = 5 nm, ϵ_M = 2.11 + i2.88, n_C = 1.33 and d_F = 200 nm, 240 nm and 280 nm. TE polarized light with λ = 632.8 nm is used.

What is the influence of the metal thickness?

The depth and width of the dip in reflectance due to excitation of a waveguide mode are dependent on the thickness of the metal layer d_M and the imaginary part of the dielectric constant of the metal ϵ''_M. This was already seen from the sensorgrams in Fig. 4.8 from a Ag- and Au-MCWG and by comparison with the reflectance from the Ti-MCWG in the previous figures. In Fig. 5.4

the reflectance from a Ti-MCWG with three different metal thicknesses d_M = 2nm, 5 nm and 10 nm, respectively, are shown.

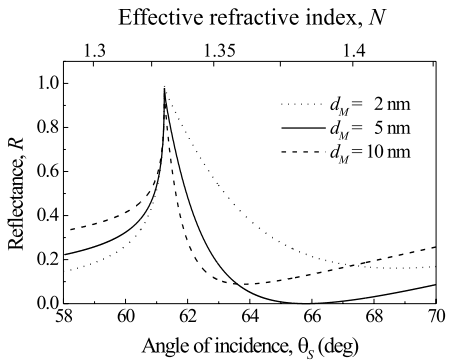

Figure 5.4. Reflectance spectra from a TI-MCWG with three different metal thicknesses. The parameters used are: n_S = 1.517, n_C = 1.33, n_F = 1.47, d_F = 240 nm, n_M = 2.11 + i2.88, d_M = 2 nm, 5 nm and 10 nm. TE polarized light with λ = 632.8 nm is used.

The position of the minimum reflectance from the Ti-MCWG is strongly influenced by the metal thickness, but similarly to the dip-type MCWG the reflectance minimum approaches zero for a given d_M (d_M = 5 nm for the configuration used in Fig. 5.2) but rises to a higher value when d_M is either increased or decreased from this value. However, the intensity and position of the peak in the reflectance spectra do not change, as the critical angle is only influenced by n_C and n_S

Similar to the dip-MCWG I define the optimum metal thickness for the peak-MCWG to be that thickness for which the reflectance dip is a minimum in order to obtain a relatively sharp peak in reflectance with a maximum difference in reflectance for the peak and dip.

To further explore the influence of the metal on the MCWGs the optimum metal thickness is plotted versus ϵ''_M in Fig. 5.5 for different metals using a waveguide film with n_F = 1.47, with a film thickness just above cutoff film thickness, which means that d_F is varied for each of the configurations in order to ensure that a waveguide mode is excited in the waveguide film at an

angle relative close to the critical angle. The optimum metal thickness is plotted for both TM- and TE-polarized light in Fig. 5.5(a) and Fig. 5.5(b), respectively.

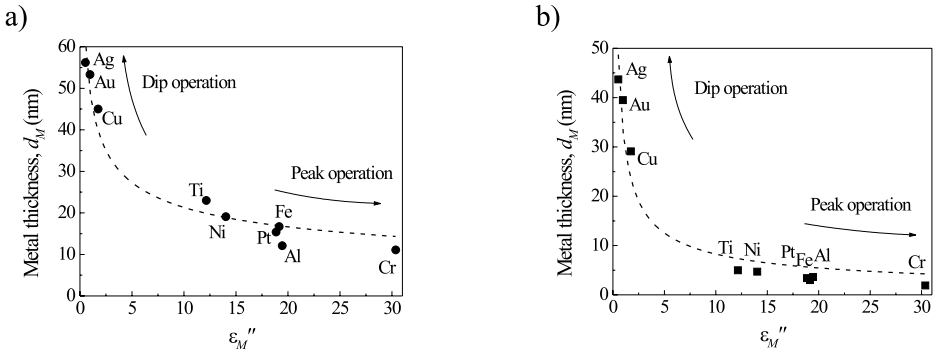

Figure 5.5. Calculated optimum metal thickness (giving zero dip reflectance) for the MCWG for different metals and with a waveguide film of n_F = 1.47 and d_F just above cutoff, (a) TM-polarized light and (b) TE-polarized light.

The parameters used for the different configurations are listed in table 5.1 below:

Metal	ϵ_M	d_F (TM)	d_F (TE)
Silver	-16 + i0.52	410 nm	251 nm
Gold	-10.22 + i0.96	390 nm	244 nm
Copper	-10.42 + i1.75	393 nm	241 nm
Titanium	-3.84 + i12.15	420 nm	254 nm
Nickel	-9.64 + i14.02	427 nm	248 nm
Platinum	-11.54 + i18.86	440 nm	252 nm
Iron	-3.17 + i19.15	446 nm	263 nm
Aluminum	-54.26 + i19.45	460 nm	253 nm
Chromium	-6.9 + i30.35	463 nm	264 nm

Table 5.1. Parameters used for calculations shown in Fig. 5.5

It is seen that the optimum metal thickness and the operation-mode of the MCWG is dependent on ϵ_M''. The optimum metal thickness in Fig. 5.5 approximately follows a line given by: $d_{M,Optimum} \propto (\epsilon_M'')^{-C}$ with $C \sim 2/3$ and $C \sim 1/3$ for TM- and TE-polarized light, respectively.

Is it possible to use the same chip for TE- and TM-polarization?

It is not possible to measure with both TE- and TM-polarized light with the same chip. First of all it would not contribute to further information as the critical angle is given by the substrate RI and

the cover RI, and thus the peak for both polarizations will be at the exact same angular position and the same shift due to a change in n_C will appear. Furthermore, it is seen from Fig. 5.5 that the optimum metal thicknesses for the two polarizations are greatly separated, but also the film thickness for which the peak arises are widely separated for the two polarizations, see the d_F in the table above. Thus the sensor can only be used for single mode operation like the SPR-sensor.

Is the detection range limited?

Similar to the dip-MCWG the detection range for the peak-MCWG is limited due to the change in angular position of the critical angle with n_C while the resonant dip changes with a lower rate. In Fig. 5.6 calculated sensorgrams are plotted for a Ti-MCWG for changes in n_C from 1.33 to 1.41 using a film thickness and film RI for which a peak with optimal reflectance is obtained for a cover RI n_C = 1.33.

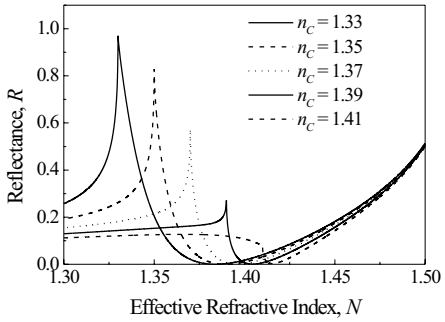

Figure 5.6. Sensorgrams from a Ti-MCWG for five different cover RIs n_C. The parameters used are: n_S = 1.517, d_F = 240 nm, d_M = 5 nm, ϵ_M = 2.11 + i2.88, n_C = 1.33, 1.35, 1.37, 1.39 and 1.41. TE polarized light with λ = 632.8 nm is used.

From Fig. 5.6 it is seen that the peak for this configuration disappears as the cover RI approaches 1.41. However, unlike the properties for the dip-MCWG the peak-MCWG maintains a cover RI sensitivity of 1 and an infinite penetration depth of the evanescent field in the cover over the entire detection range due to the peak position at the critical angle.

The detection range can be tuned by adjusting d_F for the detection area of n_C to for example include measurements on gas samples or by adjusting n_F, where an increase in n_F "squeezes" the angular spectrum resulting in a smaller detection range, because the position of the critical angle still changes with n_C while the resonant angle of the waveguide mode changes with an even smaller rate.

How sensitive is the peak-MCWG?

The sensitivity of the peak-MCWG cannot be calculated like for the dip-MCWG and is not dependent on the film thickness once the peak feature is supported. The sensitivity can be explained by considering the penetration depth of the evanescent field. The critical angle is given

by $\arcsin(n_C/n_S)$ and thus the peak is centered at $N = n_C$, this point represents the point at which the electromagnetic field in the cover is in transition from a normal propagating wave to an evanescent wave, meaning that the probing depth into the cover is infinite. Because the peak appears at $N = n_C$ the sensitivity $\partial N/\partial n_C$ is obviously 1 as seen from Fig. 5.6. Contrary to the high cover RI sensitivity the adlayer sensitivity $\partial N/\partial d_A$ is very low, approximately zero, owing to the infinitely large probing depth.

The mode profile of the electromagnetic field in the structure can be calculated as for the dip-type MCWG by use of Eq. (4.11) on page 65.

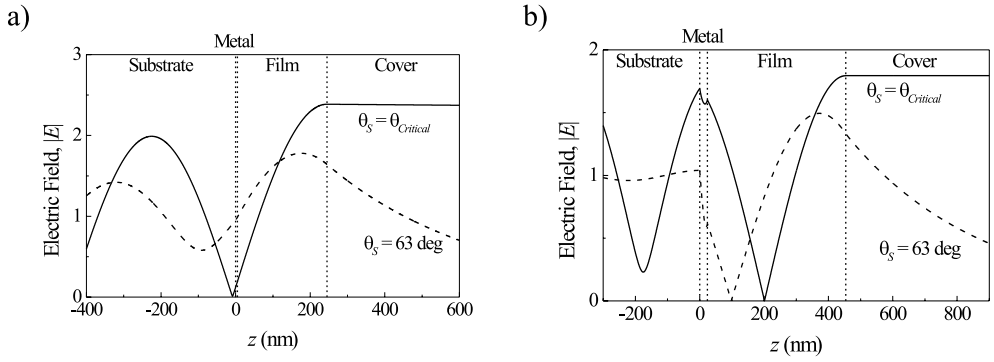

Figure 5.7. Profile of the electromagnetic field propagating in a Ti-MCWG at resonant angle (solid line) and at an angle off resonance θ_S = 63 deg (dashed line) for TE (a) and TM (b) polarized light. The parameters used are: n_S = 1.517, n_M = 2.11 + i2.88, n_F = 1.47 and n_C = 1.33. The film and metal thicknesses of the configurations are: (a) d_M = 5 nm, d_F = 240 nm and (b) d_M = 24 nm, d_F = 430 nm.

From the mode profiles in Fig. 5.7 it is seen that at resonant angle of the peak (solid lines) for both TE- and TM-polarized light an evanescent field in the cover medium arises which is infinite. For the TM polarization the field in the film shows one minimum in amplitude because the waveguide mode order $m = 1$ while for the TE polarized light no minimum of the field in the film is observed since $m = 0$ due to the character of the waveguide modes and the SPR-mode arising in metal/dielectric-structures. The mode profiles off resonant angle show a waveguide mode like field as the off resonance angle is taken above $\theta_{Critical}$ and thus approaches the resonant angle of the actual excited waveguide mode. At peak resonant angle θ_m the reflectance in the sensorgram shows the highest reflectance, which is also seen from the amplitudes of the field profiles in the substrate showing interference of the incident light of amplitude one and the reflected light at the metal/substrate boundary. The mode profiles at off resonant angle show smaller oscillations in the field in the substrate than for the mode profiles at resonant angle due to a greater part of the incident light being coupled into the waveguide film as the angle of incidence approaches the resonant angle of the waveguide mode, see for example the sensorgram in Fig. 5.3 where the reflectance vs. angle is illustrated.

In Fig. 5.8 five sensorgrams have been calculated for various examples of the existence of an adlayer in the sample to be measured in order to evaluate the adlayer sensitivity $\Delta N_m/\Delta d_A$ of the peak-type MCWG. One sensorgram is calculated for the absence of an adlayer (solid line) for comparison with sensorgrams calculated in case of an adlayer present of thickness d_A = 100 nm, where a sensorgram is calculated for four situations (I) an adlayer with RI n_A = 1.35 is positioned at the sensor surface d_P = 0 nm, (II) an adlayer with RI n_A = 1.4 positioned at the sensor surface d_P = 0 nm, (III) an adlayer with RI n_A = 1.35 positioned at the distance d_P = 100 nm from the sensor surface and (IV) an adlayer with RI n_A = 1.4 positioned at a distance from the sensor surface of d_P = 100 nm.

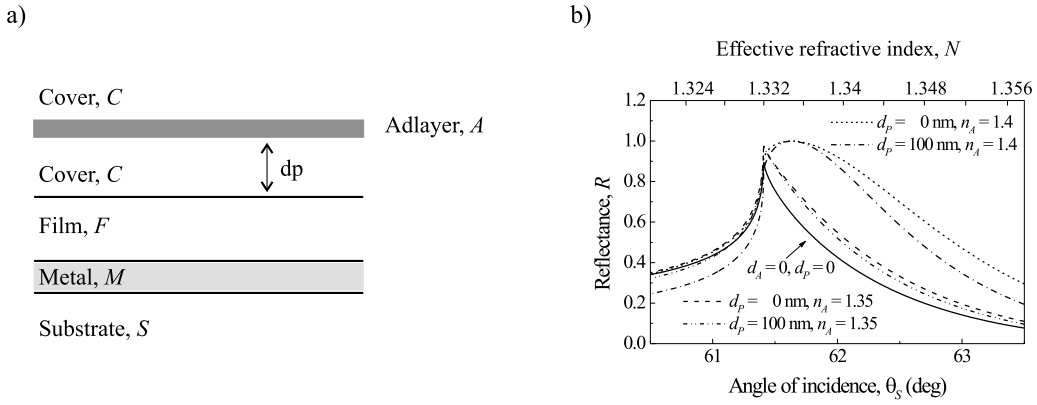

Figure 5.8. Sensorgrams from a Ti-MCWG for different adlayer cases. (a) Illustration of the MCWG and adlayer configuration. (b) The used parameters are: n_S = 1.517, n_M = 2.11 + i2.88, d_M = 5nm, n_F = 1.47, d_F = 230 nm and n_C = 1.332. The used adlayer parameters are: d_A = 0 nm and 100 nm, d_P = 0 nm and 100 nm and n_A = 1.35 and 1.4.

The position of the peak in the sensorgram for a uniform sample with no adlayer present in the sample is at $\theta_{Critical}$. Adding an adlayer of n_A on top of the sensor surface or in a distance of 100 nm from the sensor surface changes the reflectance from the sensor, as the resonant angle of the actual waveguide mode (dip) changes which is seen by an altered shape of the peak, however, no change in the peak position is observed due to no change in the critical angle. Adding an adlayer with n_A = 1.4 either at the sensor surface or at a distance of d_P = 100 nm from the sensor surface results in two sensorgrams different from the three others as a more round peak appears in both sensorgrams. The larger value of n_A results in a greater shift of the resonant angle of the waveguide mode while the critical angle is still unaffected by the adlayer as $\theta_{Critical} = \arcsin(n_C/n_S)$, and thus for this adlayer RI the peak does not arise in the sensorgram due to a range of detection for this MCWG configuration which is limited to not include these measurements. From the sensorgrams it appears that the adlayer sensitivity of the peak-type MCWG equals zero.

For which purposes is the peak-type MCWG interesting?

The peak-type MCWG is only interesting in connection with RI measurements of a uniform solution or solutions containing large objects that influence the average RI of the cover medium resulting in a change in the critical angle. This sensor has the great advantage, compared to the other waveguide configurations and the SPR sensor, that the cover RI sensitivity does not change with n_C but is one over the entire detection range, as seen from Fig. 5.6.

5.1 Interrogation mechanisms

Generally, optical sensors can be equally well applied in an angular or a wavelength interrogation setup. The previous study of both MCWG sensors has been based on an angular interrogation setup, where one wavelength has been used and the angle of incident light has been varied resulting in a sensorgram where the resonant angle of the resonant dip or peak, respectively, has been used as the sensing feature. In a wavelength interrogation setup the sensor structure is instead illuminated at a fixed angle with light spanning over a range of wavelengths resulting in a sensorgram of reflectance vs. wavelength when operated in reflection mode, where the sensing feature is a resonant wavelength λ_m.

Both the peak- and dip-type MCWG are prism-coupled and operated in reflection mode and thus potentially both the angular and wavelength interrogation should be applicable for the MCWGs. The angular interrogation and the wavelength interrogation setups are illustrated in Fig. 5.9 and 5.10, respectively, for both types of MCWG sensors. In the angular interrogation setup, illustrated in Fig. 5.9, the laser beam is focused at the substrate/metal-boundary of the MCWG, thus the light is incident over a small range of angles and reflected over the same angular range. At the resonant angle where the waveguide mode is excited a dip in reflectance is observed, illustrated by the black line in the reflected beam, and the reflected intensity can be recorded by a CCD array. The sensorgrams from the angular interrogation setup in Figs. 5.9(b) and 5.9(c) for the peak-type and dip-type MCWG, respectively are similar to the ones previously shown in connection with the MCWG presentation. The sensorgrams from both types of MCWGs are illustrated for a change

in cover RI from n_C = 1.33 to n_C = 1.34, and from both sensorgrams all the important features appear: The critical angle, the resonant angle and the width of the reflectance dip.

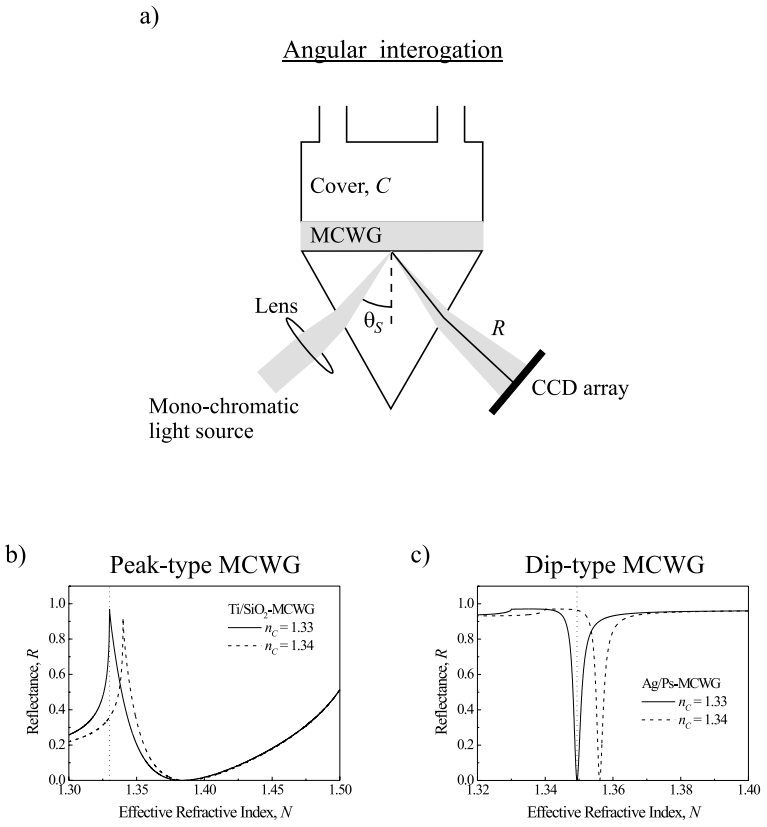

Figure 5.9. (a) Angular interrogation setup for the prism-coupled MCWG sensor. The sensorgrams for the peak- and dip-MCWG for the angular interrogation setup are shown in (b) and (c), respectively. The parameters of the MCWG configurations are: (b) n_S = 1.517, n_M = 2.11 + i2.88, d_M = 5 nm, n_F = 1.47, d_F = 240 nm, n_C = 1.33 and n_C = 1.34, and TE polarized light with λ = 632.8 nm has been used, (c) n_S = 1.517, n_M = 0.065 + i4, d_M = 56 nm, n_F = 1.59, d_F = 340 nm, n_C = 1.33 and n_C = 1.34, and TM polarized light with λ = 632.8 nm has been used.

For the wavelength interrogation setup, illustrated in Fig. 5.10(a) the MCWG is illuminated by a broadband light source at a fixed angle. In Fig. 5.10(b) and (c) the sensorgrams from a peak-

and dip-MCWG sensor, respectively, are shown for a fixed N = 1.33 (illustrated by dotted lines in Figs. 5.9(b) and (c)) when the cover RI is changed from n_C = 1.33 to n_C = 1.34.

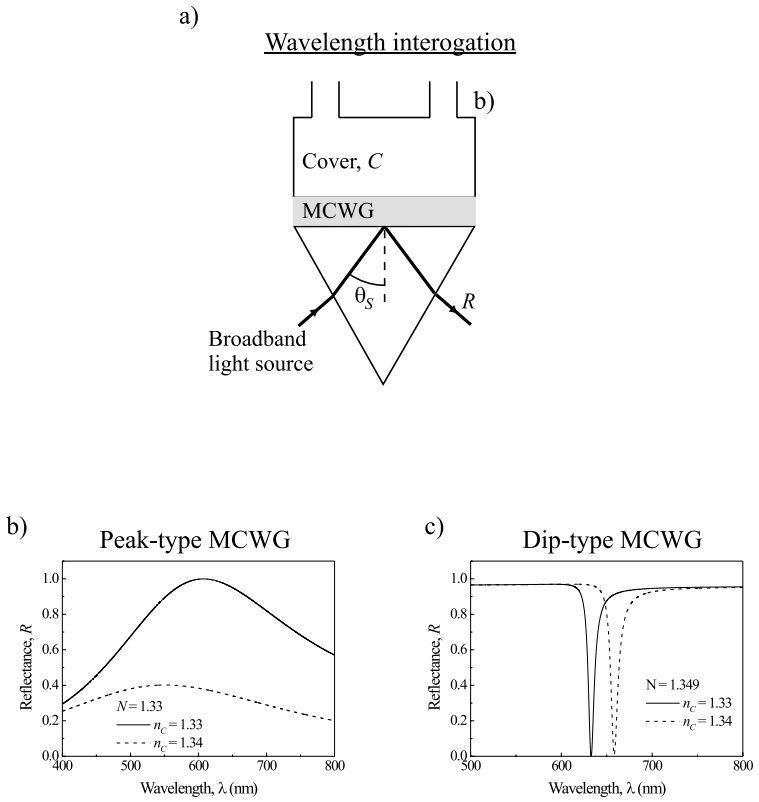

Figure 5.10. (a) Wavelength interrogation setup for the prism-coupled MCWG sensor. The sensorgrams for the peak- and dip-MCWG for the wavelength interrogation setup are shown in (b) and (c), respectively. The parameters of the MCWG configurations are: (b) n_S = 1.517, n_M = 2.11 + i2.88, d_M = 5 nm, n_F = 1.47, d_F = 240 nm, n_C = 1.33 and n_C = 1.34, and TE polarized light has been used at N_m = 1.33, (c) n_S = 1.517, n_M = 0.065 + i4, d_M = 56 nm, n_F = 1.59, d_F = 340 nm, n_C = 1.33 and n_C = 1.34, and TM polarized light at N_m = 1.33 has been used.

In Fig. 5.10(b) the sensorgrams from the peak-type sensor are shown for a fixed value of N = 1.33 which is N_m of the resonant peak for a cover medium with n_C = 1.33. A maximum reflectance in the sensorgrams appears which changes in wavelength position for a change in n_C. However, the sharp peak feature observed for the angular interrogation arising due to the critical angle does not appear in the sensorgrams, and as this sharp peak is the important feature for the peak-MCWG sensor the wavelength interrogation setup is not interesting in connection with this MCWG sensor.

The sensorgrams in Fig. 5.10(c) show the reflectance from a dip-MCWG versus wavelength where a similar spectrum to what is seen for the angular interrogation setup is observed, except that the critical angle does not appear, as this angle is given by the refractive indices and are not directly dependent on the wavelength. However, both the dip position and width of the dip appear versus

wavelength in the sensorgram with the result that the wavelength interrogation setup can easily be applied for the dip-type MCWG. As the critical angle does not influence the sensorgram, the detection range of the sensor can actually be expanded compared to when the sensor is used in an angular interrogation setup, since the parameter limiting the detection range is the critical angle.

5.2 Discussion

The peak-type MCWG has an infinite penetration depth of the evanescent field in the cover and can with advantage be used for broad range refractive index measurements. The cover RI sensitivity is constant over the entire detection range for changes in n_C with a high sensitivity of one, and the detection range is broad. However, the sensor is not useful for thin adlayer measurements, as the adlayer sensitivity is zero.

For actual measurements with the MCWG sensors the analysis of the experimental setup showed that only the angular interrogation setup is relevant for the peak-type MCWG. For the dip-type MCWG both the angular and the wavelength interrogation setup can be used and actually the wavelength setup indicates that the detection range can be expanded using this setup.

Chapter 6

Metal-clad waveguide sensors - Experiments

The peak- and the dip-type MCWGs can both support a large evanescent field in the cover medium and show potential for detection of micron-scale biological objects, and both sensors have been applied for biosensing by each of the groups that initially presented the sensors[27, 57]. However, no comparison of measurements with the two sensors have been presented. In connection with this work I have fabricated a silver dip-type and a titanium peak-type MCWG sensor and applied both sensors for RI measurements and cell detection.

For the measurements I have used a rotating retro-reflector setup with angular interrogation. The setup has been optimized to ensure that the same area of the sensor are used during the measurements over the rotation range.

The RI-measurement and detection of cells have been performed as time measurements and give the opportunity for comparison of the two sensors sensitivities when they are used for deep-probe sensing.

6.1 Fabrication

What MCWG-configurations have been used for experiments?

The peak-type configuration used for the measurements is a Ti/SiO_2 MCWG for TE-polarization with a 5 nm titanium cladding (n_M = 2.11 + i2.88) and a 230 nm SiO_2 film (n_F = 1.47) and the dip-type MCWG configuration is an Ag/PS MCWG for TM-polarized light with a metal cladding of 60 nm silver (n_M = 0.065 + i4.0) and a 330 nm thick polystyrene (PS) film (n_F = 1.59).

How are the MCWGs fabricated?

The fabrication process of both configurations is quite simple as it only involves two fabrication steps. The substrate for both configurations is a 1 mm thick glass plate (n_S = 1.517) of 2 x 2 cm. For the Ti/SiO_2 chip the titanium is evaporated onto the glass substrate in a vacuum chamber and afterwards the SiO_2 is deposited at 200 ^oC also in vacuum conditions.

For the Ag/PS chip, the silver layer is sputtered onto the glass substrate in a vacuum chamber and afterwards the PS film is spin coated directly on top of the silver coating. After spin coating, the chip is dried in a oven at 120 °C for 60 min. The fabrication of both MCWG-chips is conducted in a class 1000 clean room and between fabrication processes the chips are brought into normal atmospheric conditions.

Before metal deposition on the glass substrates the glass plates are run through a cleaning process to clean off oil and grease on the glass surface first and cleaning off other materials afterwards. The glass cleaning procedure is as follows:

Cleaning of glass substrates (at room temperature):

Soak the glass substrate in acetone for 3 min.

Rinse in ultra pure water.

Soak the glass substrate in ethanol for 3 min.

Rinse in ultra pure water.

Soak the glass substrate in chromosulfuric acid for 3 min.

Rinse in ultra pure water.

Rinse the glass substrate in KOH (10%) for a few seconds.

Rinse the glass substrate for 45 min in flowing ultra pure water.

Dry the glass plate at 120 ^{o}C for 2 hours.

Materials used:

Chromosulfuric acid (Chrom-(VI)-oxid) from Merck, Germany.

Potassium hydroxide (KOH) from Merck, Germany.

Metal deposition:

The titanium and silver claddings are deposited on the glass substrate by metal evaporation and sputtering, respectively. Both deposition techniques take place in vacuum conditions.

Metal evaporation is typically used for deposition of thin layers, as the amount of metal possible to evaporate is limited. The deposition rate can be set very low and thus the thickness of the layer can be accurately controlled. The thickness is typically measured during the evaporation process by a quartz crystal placed very close to the sample to be coated. By measuring the change in resonance frequency of the crystal the thickness of the deposited metal layer can be determined.

Metal evaporation is conducted by heating the material to be evaporated in a filament. The filament is either heated to above the melting point of the metal or the metal is heated to above the melting point by an electron beam which is focused on the source metal. The sample to be coated is placed close to the source metal and a thin metal film is deposited. The deposition rate can be controlled by increasing or lowering the temperature of the source metal.

The optimum thickness of the titanium layer for the peak-type MCWG is 5 nm and a variation of a few nanometers can change the reflectance spectrum from the sensor significantly as seen in Fig. 5.4 and thus the thickness should be controlled very accurately during the metal deposition. This is why metal evaporation is used for the titanium deposition.

Sputtering is typically used for thick metal film deposition. The deposition rate is typically faster for the sputtering technique than for the metal evaporation. Sputtering is accomplished by bombarding a source metal with energetic ions, which is typically Ar^+. When the ions hit the surface of the source metal atoms or clusters of atoms are knocked loose and transported to the substrate. As the metal deposition happens as single atoms or clusters of atoms the thickness is hard to control and the surface roughness can be higher with this method than for the evaporation.

The silver thickness used for the dip-type MCWG is around 60 nm, but the reflectance spectrum does not change significantly if the thickness varies with up to 5 nm. Thus sputtering is used for the silver deposition due to the thickness of the silver layer. The silver deposition on the glass plates has been conducted by the company Polyteknik.[73]

Film deposition:

For the Ag/PS-chip the PS film is deposited directly on top of the silver coating on the glass substrate by spin coating. The PS [Mw: 1410000, Mw/Mn: 1.05 from Polymer Source Inc., Canada] is dissolved in toluene and depending on the thickness of the PS film the velocity of the spinner or the concentration of the polymer solution is changed. To obtain a 330 nm PS film a concentration of 1.1 g PS / 50 mL toluene is used at a spinning velocity of 4100 rpm for 60 s.

During the spinning process the toluene is partly evaporated. However, to evaporate the remaining solvent the sample is baked at 120 °C for 60 min. The thicknesses of the polystyrene film have been controlled by measuring on a second chip made simultaneous to the one to be used for measurements. After baking and cooling of the sample parts of the film were removed mechanically thereby enabling 2D measurements of the film thickness using a surface profiliator (Dektak V 200-Si, Veeco).

SiO_2 deposition is typically achieved by a reaction of silane(SiH_4) and oxygen(O_2) at high temperatures (300 - 500 °C) in vacuum. The SiO_2 waveguide film of the peak-type MCWG is deposited onto the Ti-cladding, which during the deposition process is heated to 200 °C. The SiO_2 film is deposited at a rate of 40 nm/min. This film thickness has not be measured directly but indirectly by producing a number of Ti/SiO_2-chips where the deposition times have been varied and afterwards applying the chip in an experimental setup for RI measurements of water.

What considerations are important in connection with fabrication of MCWGs?

The fabrication of the MCWG should be conducted in dust-free surroundings. Dust can influence the quality of the resonant dips and on later measurements, as a dust particle on the sensor surface will be measured as a part of the sample. During fabrication dust in the polymer film can influence the surface quality of the spin coated polymer film and also dust in the film can influence the guided light due to scattering. For surface modification or cleaning of the sensor surface plasma treatments are often used, in that connection dust particles in the film can cause the plasma treatment meant for surface modifications to penetrate into the film and thus make holes or small roughnesses on the film surface.

The materials for the different layers of the MCWG-structure should be compatible with each other in order to obtain a good binding of the layers to avoid that the chip is ruined during use. The RI and biological properties of the waveguide film should be considered for the measurements wished to be conducted with the sensor. Certain polymers are easier to modify by surface chemistry than others to obtain the right properties. One more factor to consider when choosing materials is the fabrication; are the materials easy to deposit and with high quality? In this work these properties have not been the main issue and thus only a few different materials have been tested in the fabrication.

Have other configurations of the MCWG been considered?

A few other materials for the MCWGs have been considered and tested by fabricating chips with the following configurations: Ag/SiO_2, Ag/PMMA and Ti/PMMA [PMMA: poly(methyl methacrylate), Mn: 221800, Mw: 257300, Mw/Mn: 1.16 from Polymer Source Inc., Canada].

Polystyrene is a non-polar hydrophobic polymer which makes the surface difficult to modify for specific binding of biological objects, thus for the dip-type MCWG a PMMA and a SiO_2 film have been tested for waveguide films due to the ability to surface modify both films. The PMMA film was applied to the chip by spin coating like the PS film and various modification procedures were tested. Unfortunately, well-documented surface modification procedures often involves procedures involving a small degree of etching or dissolving of the surface material, which dissolved the silver layer on the chip. A method suggested by Fixe et al[74] was tested and could successfully be applied to the waveguide configuration without dissolving any of the materials comprising the MCWG. Tests with binding of fluorescent DNA and proteins did show successful binding of these objects to the PMMA surface and thus this configuration is a possibility. The configuration with SiO_2 is not useful as the SiO_2 film ruptured when fluid was applied onto the sensor surface, this could be due to surface tension between the SiO_2 layer and the silver.

The Ti/PMMA configuration was also successfully fabricated and used for RI measurements and due to the successful surface modification of the Ag/PMMA configuration this configuration may also be used for experiments if further explored. However, another possibility is to obtain polystyrene which is pre-modified[75] and can be used for specific binding purposes.

6.2 Experimental setup

Angular and wavelength interrogation was described in the previous chapter for both the peak- and the dip-type MCWG. The angular interrogation setup can be used for both configurations and a rotating setup has been used for experiments performed with both sensors. A setup referred to as the retro-reflector setup introduced in the literature by Innes[76] has been slightly modified and used for the setup. In that connection, care has been taken to ensure that the measurements are performed at the same area of the sensor surface during rotation.

What setup is used?

In Fig. 6.1 the experimental setup is illustrated. The sensor-setup (prism + MCWG-chip) is mounted on a high-precision goniometer with a rotation span of 13 deg for varying the angle of incidence. A fixed He-Ne laser illuminates the MCWG chip through the prism and the intensity of the reflected beam is measured by a fixed photodiode. In front of the photodiode is placed a lens with focal length of 3 cm and diameter of 1.5 cm. In the figure the rotation of the sensor-setup is illustrated for two positions of the prism and two light paths (black and gray lines) for each of the prism positions.

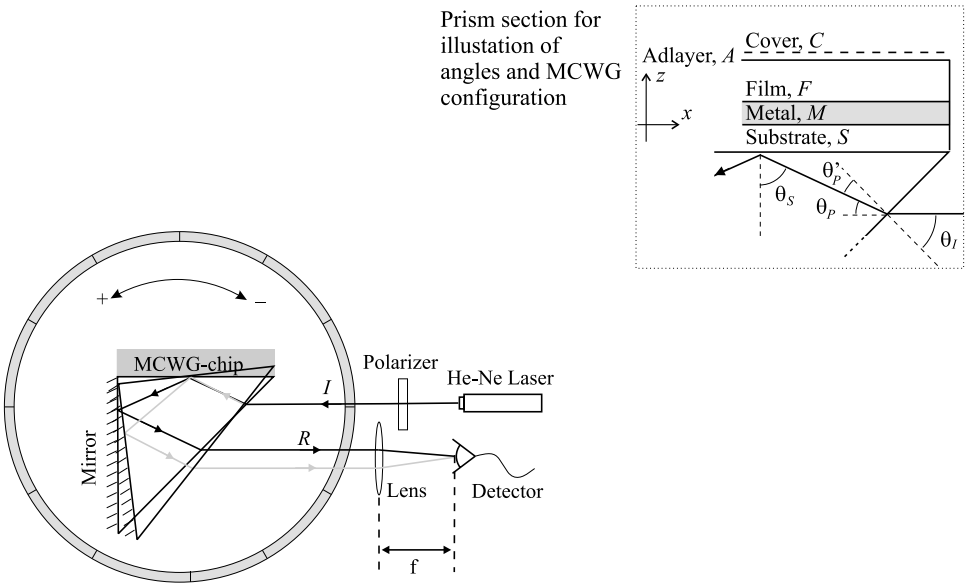

Figure 6.1. Experimental setup similar to the retro reflection arrangement introduced by Innes.[76] The insert illustrates the MCWG configuration and the angle of the light beam in the prism.

The light is coupled into the waveguide through a prism with a 90° angle with a size of 2×2 cm^2 of the prism plane onto which the MCWG-chip is placed. The prism and the substrate have the same RI and are brought into contact with each other through the use of index-matching fluid [Microscopy immersion oil with n = 1.515 - 1.517 ($C_{14}H_{12}O_2$) from Merck, Germany] to avoid reflections from that boundary. On the adjacent side of the prism the surface is coated with a 200

nm thick silver-layer acting as a mirror. The mirror is applied for two reasons, one is to extend the range of angles at which the setup can be operated and secondly to simplify the setup.

The prism configuration used simplifies the setup in the way that the beam incident on the sensor setup and the reflected beam will always be parallel, however, the distance of the reflected beam to the incident beam will change due to the change in angle of incidence at the prism θ_I, see insert in Fig. 6.1. The displacement in reflected beams parallel to the incident beam are compensated by inserting a lens in front of the photo detector. The photo detector is placed in the focal point of the lens and thus ensuring that a fixed detector can be used. Normally, for experimental setups involving angular interrogation a change in angle of incident light γ results in an angular change of the reflected light of 2γ and thus a rotation of two parts of the setup are necessary.[77]

The relation between the illustrated angles and the effective refractive index of the waveguide, N are given by:

$$\begin{aligned} \theta_I &= \arcsin[n_S \sin(\theta'_P)], \\ \theta'_P &= 45 - \theta_P, \\ \theta_S &= 90 - \theta_P, \\ N &= n_S \sin(\theta_S). \end{aligned} \tag{6.1}$$

Photographs of the setup are shown in Figs. 6.2 and 6.3 where the photograph in Fig. 6.3 shows a closeup of the goniometer and the sensor setup.

A He-Ne laser with λ = 632.8 nm (not shown) is used in the setup and the light path through the setup follows the numbers in Fig. 6.2, where the light first passes through a semi reflecting mirror (1) in order to adjust the intensity of the incident beam. The beam is directed towards the prism by the mirrors (2 and 4) while passing through a polarizer (3). The prism, sensor-chip and cuvette are

mounted on the goniometer (5) and the reflected light passes through a lens (6) and the intensity is measured using a photo detector [Model 2001 from New Focus] (7).

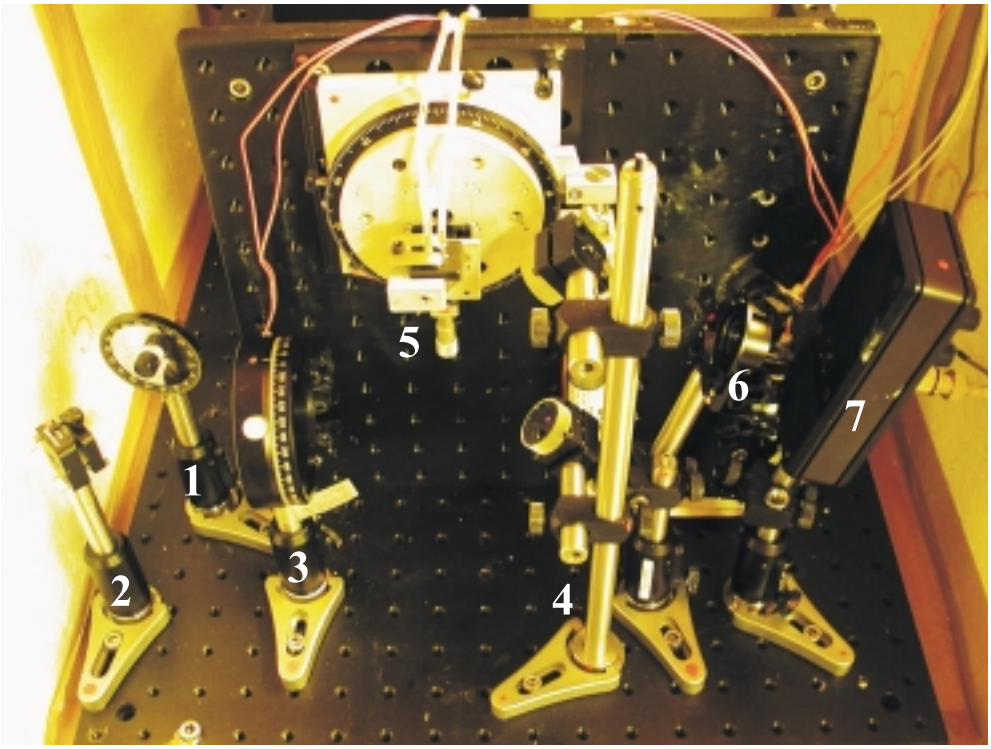

Figure 6.2. Photograph of the setup. The objects in the photograph are: (1) semi-reflecting mirror, (2) mirror, (3) polarizer, (4) setup with two mirrors, (5) holder where the prism, sensor-chip and cuvette are mounted and the in- and outlet tubes to the cuvette are mounted onto the cuvette, (6) focusing lens and (7) photo detector.

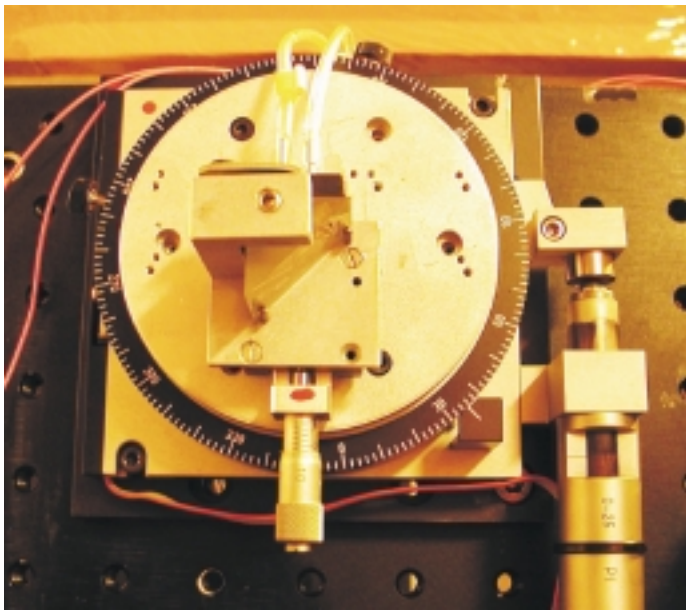

Figure 6.3. Photograph of goniometer on which the holder is mounted with the prism, sensor-chip, cuvette and the in- and outlet tubes connected to the cuvette.

The measurements are conducted by placing a cuvette on the sensor surface leaving an area of 3.5 mm x 5 mm of the sensor surface to be exposed to the sample solution. In Fig. 6.4 photographs of the prism and the cuvette are shown. The prism is coated with a 200 nm silver layer on the side that appears black on the photograph. The photograph of the cuvette shows the surface which is fixed on the sensor surface, where the dark ring in the photograph is an O-ring used to seal the cuvette on the sensor surface and the dark spots seen in the cuvette are the inlet and outlet tubes.

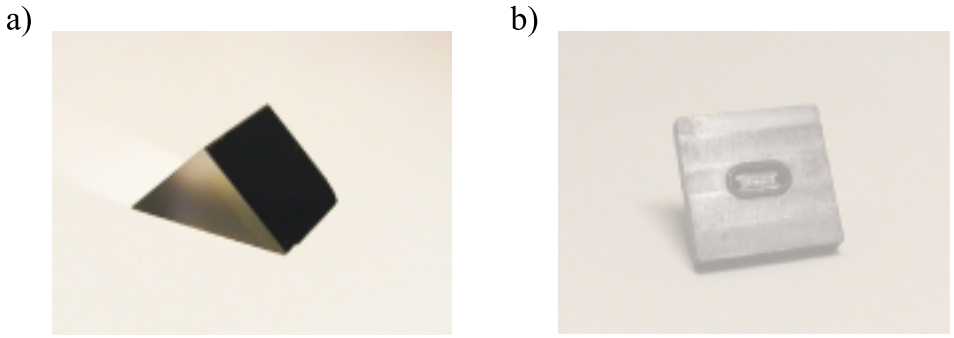

Figure 6.4. Photographs of (a) the prism with silver coating and (b) the cuvette used in the setup.

The exposed area on the waveguide surface to the sample is 5 mm in one of the directions. This size have been choosen to make sure that the beam is always incident within the exposed area. The position of the beam and the size of the beam are the reasons of this choise. Due to the use of a plane sided prism a change in the angle of incidence can result in a change of the position of the incident beam on the MCWG-chip. Due to the high angle of incidence of the light in the prism θ_S at around 65 deg for which the resonant angle arises (as seen from the sensorgrams in chapters 4 and 5) the incident beam on the prism is expanded in one direction when transmitted through the prism onto the prism/sensor interface.

Regarding the movement of the beam spot on the MCWG, for optimum measurements the spot should be at the exact same place during the measurements and thus during rotation of the setup we have to ensure that the measurements are conducted at the same conditions. The sensor-chip can have small variations in the film or metal thickness and in the quality at different places on the chip thus by ensuring measurements at the exact same place on the MCWG the influence of these variations are eliminated.

The optimum place of the incident beam on the prism to avoid or minimize movements of the spot on the MCWG during rotation is calculated in Fig. 6.6. In Fig. 6.5 the parameters appearing in the calculation of the optimum place for illumination of the prism is illustrated.

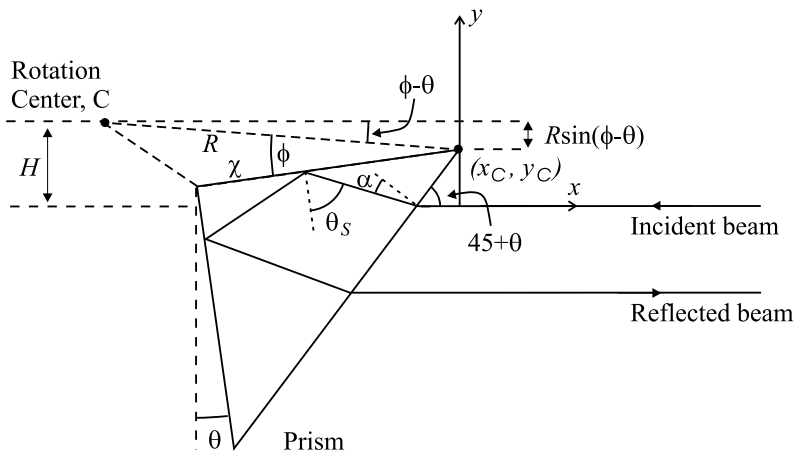

Figure 6.5. Illustration of angles and distances used for calculation of the position of the spot on the prism/sensor interface.

The parameters in Fig. 6.5 are:

C: The rotation center of the setup.

H: The distance in y-direction between the line of the incident beam and C.

R: the distance between C and (x_C, y_C).

χ: The distance from (x_C, y_C) to the position of the beam incident on the prism/sensor interface along the prism surface.

$R\sin(\phi - \theta)$: The distance in y-direction between (x_C, y_C) and C.

θ: The angle that the prism is rotated.

θ_S: The angle of incidence in the prism.

$45 + \theta$: The angle of the incident light in air at the air/prism boundary to the prism surface.

α: The angle of the light in the prism at the air/prism boundary.

ϕ: The angle between the line R and the x-axis.

The distances and the angles in Fig. 6.5 are given by:

$$
\begin{aligned}
y_c &= H - R\sin(\phi - \theta), \\
\sin[90 - (45 + \theta)] &= n_S \sin(\alpha), \\
\alpha &= \arcsin\left[\tfrac{\sin(45-\theta)}{n_S}\right], \\
\tfrac{\chi}{sin(90+\alpha)} &= \tfrac{y_c/\sin(45+\theta)}{\sin(45-\alpha)}, \\
N &= n_S \sin(45 + \alpha),
\end{aligned}
$$

from which it is found that for a spot position on the prism/sensor interface at the midpoint of the prism surface, χ = 10 mm in the case of a prism of side length = 20 mm, the light should be incident on the prism at a position given by: H = 2.2 mm and R = 6.8 mm.

For the above values of H and R the position of the spot on the prism/sensor interface can be calculated vs. angle of incidence on the prism θ_I. The calculated curve is shown in Fig. 6.6(a). In Fig. 6.6(b) the corresponding N is shown vs. θ_I.

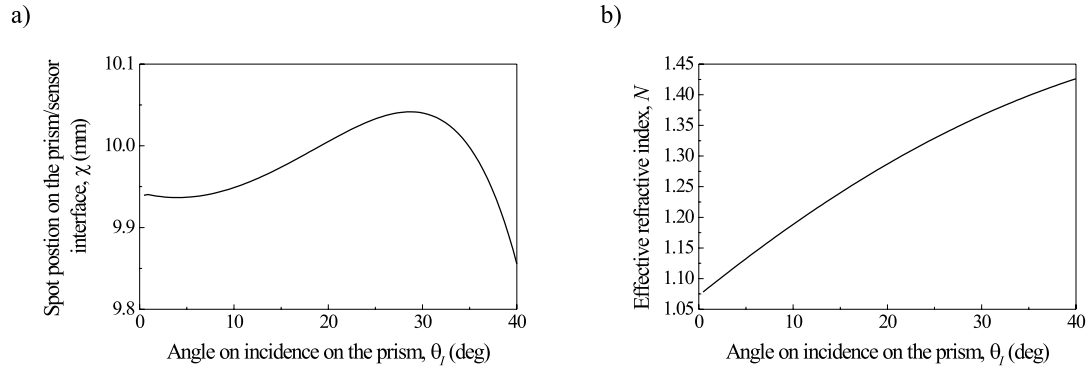

Figure 6.6. Calculated position of the spot from the beam at Prism/MCWG interface vs. the angle of incident light on the prism (a) and (b) curve of N vs. the angle of incident light on the prism.

From the calculated change in spot position on the prism/sensor interface it is seen that a rotation of 13 deg (the entire rotation range of the setup) basically does not influence the spot position if H and R are chosen properly. The interesting area to notice is for N around 1.35 for the dip-type and for N = 1.33 for the peak-type MCWG corresponding to $\theta_I \sim 26$ deg, for which the movement of the spot position is less than 0.1 mm, thus the retro reflector setup is very useful for rotational angular interrogation setup used for the MCWG sensors.

6.3 Deep-probe measurements

Two different measurements have been conducted: Cover RI-measurements and detection of unlabelled cells settling on the sensor surface. Both measurements are conducted with a peak-type and a dip-type sensor.

The reflectance curves for the two MCWGs fabricated for experiments are calculated in Fig. 6.7 for a change in cover medium from ultra pure water (n_C = 1.3325) to a 50% v/v PBS/water-solution (n_C = 1.333) which are the solutions used for the RI measurements (v/v: volume/volume).

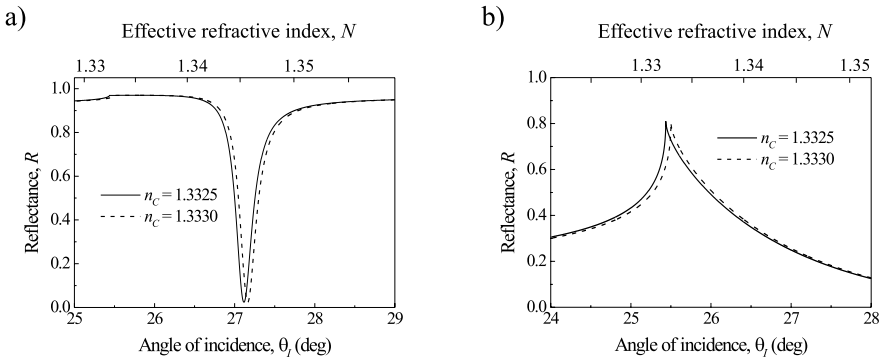

Figure 6.7. Calculated reflection curves for two sensor configurations, the dip-type MCWG (a) and the peak-type MCWG (b) for cover RIs n_C = 1.3325 and n_C = 1.333. The used parameters are: (a) n_S = 1.517, n_M = 0.065 + i4, d_M = 60 nm, n_F = 1.59 d_F = 330 nm and TM polarized light. (b) n_S = 1.517, n_M = 2.11 + i2.88, d_M = 5 nm, n_F = 1.47 d_F = 230 nm and TE polarized light.

The reflectance curves of the dip-type MCWG in Fig. 6.7(a) shows that the angular dip position changes 0.05 deg for the change in cover RI, which results in a cover RI sensitivity $\partial N_m/\partial n_C$ = 0.74. From Fig. 6.7(b) it is seen that for the peak-type MCWG the peak position in N_m equals n_C and thus the cover RI sensitivity $\partial N_m/\partial n_C$ = 1.

RI-measurements

The peak-type and dip-type MCWG have been used for RI-measurements, shown in Fig. 6.8.

For the RI-measurements the change in angular position of the dip and the peak have been measured when changing the cover medium from pure water (RI = 1.3325) to a 50% v/v PBS/water-

solution (RI=1.333) and back to pure water. The measurements are flow-measurements with a flow of 16 μL/min and a sensorgram measured every 44 sec.

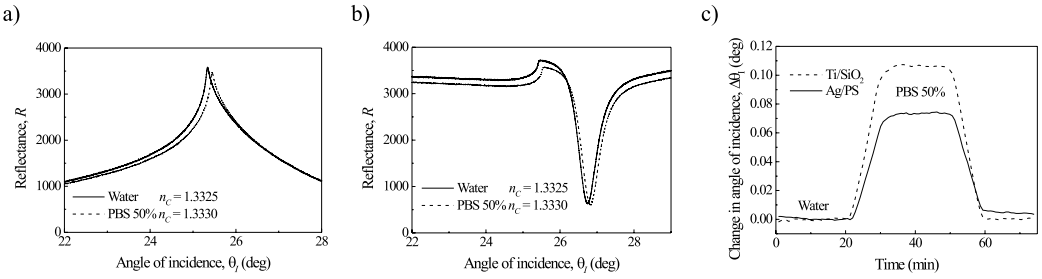

Figure 6.8. Measured sensorgrams with the peak-type MCWG (a) and the dip-type MCWG (b) for a change of cover medium from water to 50% v/v PBS/water solution. (c) Time measurements with the two sensors for the same cover media.

Fig. 6.8(a) and (b) show the sensorgrams for water and the 50 % v/v PBS/water-solution measured with the peak-type and dip-type MCWG-sensor, respectively. In Fig. 6.8(c) the time measurements with both sensors are shown, where the change in angular position of the peak and dip, respectively in reflectance vs. time is plotted. The curves have been smoothed over 10 adjacent points and results in angular changes of 1.05 and 0.75 deg for the Ti/SiO_2-sensor and the Ag/Ps-sensor, respectively. Hence, the peak-type MCWG gives a change in angular position which is 40 % larger than the angular change of the dip position from the Ag/PS-sensor. The angular change is not linear with N_m and thus, calculating the change in N_m for the dip-type and peak-type MCWG a slightly larger difference in the cover sensitivity is obtained, as the change in N_m of the peak-type MCWG is 43 % larger than for the dip-type MCWG. Comparing this change with the calculated changes in cover RI sensitivities shows a theoretical sensitivity for the peak-type MCWG which is 35 % higher than for the dip-type MCWG.

Cell detection

The two MCWG-sensors have also been used for detection of cells settling onto the sensor surface. These measurements are shown in Fig. 6.9 and 6.10, where Fig. 6.9(a) shows the angular change of the gravity point of the peak for a Ti/SiO_2 MCWG with a 5 nm thick titanium cladding and 230 nm SiO_2 film. The measurements are conducted in a cuvette without flow, where a CO_2 independent medium with RI = 1.332 is applied to the cuvette and after 65 min 80 μL of the cell-solution with a concentration of 100 cells/μL is added. The cells used are dead Hacat cells and they are in the same medium as first applied to the cuvette. Fig. 6.9(c) shows a microscope picture taken with an x10 objective of the surface coverage right after ending the measurements. The area shown is 460 x 400 μm^2 and the average surface coverage is 200 cells/mm^2. The position of the

gravity point of the peak shifts from 23.88 deg to 24.08 deg and then down to 24.05 deg where it seems to saturate resulting in ΔN_m = 0.00138. By smoothing the curve over 15 adjacent points the signal/noise ratio is 1160 resulting in a detection limit below 0.2 cells/mm^2. In Fig. 6.9(b) three sensorgrams are shown, taken respectively 40, 90 and 200 min after the measurement was started. The sensorgram recorded after 40 min shows a very sharp peak and is comparable to the calculated sensorgrams for the peak-type MCWG. However, after the cells are added to the cuvette the sensorgrams recorded after 90 and 200 min both show a more flattened peak. This flattening of the peak can be caused by the solution now consist of 2 materials, the medium and the cells, with 2 different RIs. This is also the reason for measuring the position of the gravity point of the peak rather than the peak position. Measurements of cells using a reverse symmetry waveguide sensor have shown similar effects, where the shape of the intensity peak from the waveguide mode changed remarkably as a broadening of the peak occurred due to an extra peak appearing in the spectrum.

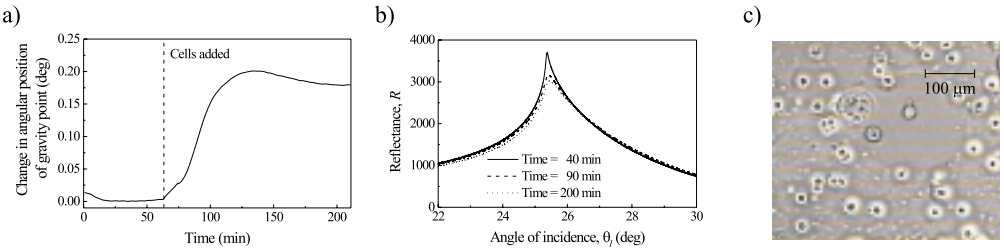

Figure 6.9. Detection with the Ti/SiO_2 peak-type MCWG of unlabelled Hacat cells settling onto the sensor surface. The MCWG configuration is: glass substrate, 5 nm thin titanium cladding, a 230 nm thick polymer film and TE-polarized light. (a) Change in angular position of the gravity point of the reflectance peak. (b) Sensorgrams recorded during the measurement after 40 min, 90 min and 200 min. (c) Microscope image of the exposed sensor surface immediately after the measurement was stopped.

The measurement with the dip-type MCWG, shown in Fig. 6.10 is similar to the one with the peak-type sensor. The medium is the same as the above-mentioned and same cell-concentration, but the cells used here are dead Fibroblast cells and only 60 μL of the cell-solution were added. A microscope image of the sensor surface is shown in Fig. 6.10(c) of an area of 610 x 460 μm^2. The average surface coverage is 260 cells/mm^2. From Fig. 6.10(a) an angular shift of 0.1 deg of the position of the gravity point of the dip corresponding to ΔN_m = 7.5 x 10^{-4} is measured. By smoothing the curve over 15 adjacent points the signal/noise ratio = 1140 and detection limit for this dip-type configuration is found to 0.23 cells/mm^2. In Fig. 6.9(b) three sensorgrams are shown, taken respectively 10, 40 and 150 min after the measurement was started. The sensorgram recorded after 10 min shows a sharp dip with low reflectance at the dip minimum and is comparable to the calculated sensorgrams for the dip-type MCWG. However, after the cells are added to the cuvette the minimum reflectance of the dips increases significantly, as seen in the sensorgrams recorded after 40 and 150 min. This can be caused by the same phenomenon as the flattening of the peaks

measured with the peak-type MCWG namely, that the solution now consists of both the medium and the cells with 2 different RIs. Again the position of the gravity point for the dip is measured rather than the position of the dip, as the dip is less distinct for the later recorded sensorgrams.

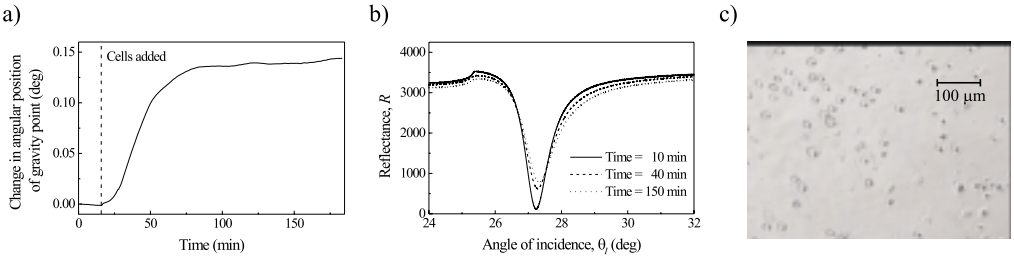

Figure 6.10. Detection with the Ag/PS dip-type MCWG of unlabelled Fibroblast cells settling onto the sensor surface. The MCWG configuration is: glass substrate, 60 nm silver cladding, a 330 nm thick polymer film and TM-polarized light. (a) Change in angular position of the gravity point of the reflectance dip. (b) Sensorgrams recorded during the measurement after 10 min, 40 min and 150 min. (c) Microscope image of the exposed sensor surface immediately after the measurement was stopped.

The detection limit for cells on the sensor surface for the peak-type sensor is a little lower than for the dip-type sensor. The lower detection limit arises due to a higher penetration depth of the evanescent field in the cover medium.

6.4 Discussion

The retro-reflector setup has proven very useful for wavelength interrogation measurements with the MCWG sensor. Illuminating the sensor at a given position on the prism it is ensured that the measurements are performed at basically the same spot during rotation of the sensor-setup.

RI measurements with both the peak- and the dip-type MCWG sensors show that the calculated difference in cover RI sensitivity for the peak-type and dip-type MCWG sensor is approximately 35 % which corresponds nicely with the sensitivity obtained from the cover RI measurements, where a change in angular position of the sensing probes for the peak-type compared to the dip-type shows a 40 % larger change in angular position or 43 % change in N_m.

Experiments for detection of cells settling on the sensor surface show that both the peak- and the dip-type MCWG sensor can successfully be applied for deep-probe sensing as a detection limit of 0.2 cells/mm^2 due to the signal-to-noise ratios is obtained for both sensors and thus unlabeled detection of a single cell at the sensor surfaces is possible.

Chapter 7

Conclusion

This thesis has been a study on planar waveguide sensors for deep-probe biosensing, where I have presented thorough studies on a reverse-symmetry waveguide sensor *the freestanding multimode waveguide* and metal-clad waveguide sensors, *the dip-type MCWG* and *the peak-type MCWG*. These sensors are all suitable for deep-probe sensing because a large evanescent field can be excited in the cover medium with infinite penetration depth.

The emphasis of the study of waveguide configurations has been on optimization of the sensitivity of the sensors for detection of micronsize biological objects like bacteria and whole cells.

In connection with the reverse-symmetry waveguide configuration I have shown reverse-symmetry operation of the simplest possible waveguide sensor, comprising a simple glass plate acting as the waveguide film, the freestanding multimode waveguide. A simple sensing principle was used for the sensor, where the maximum number of possible modes in the waveguide is counted, gives a reading of the absolute refractive index with an accuracy of 0.001 RI units. The interesting application for this sensor operation is broad range refractometry, where a detection range from n_C = 1 to n_C = 1.52 was achieved. The freestanding multimode waveguide sensor has only been presented by Qi et al, who applied a different sensing principle to the sensor resulting in a limited detection range of 1.5x10^{-3} RI units. Thus, using the mode-counting principle the detection range is extended with two orders of magnitude and includes the possibility of detection of gases.

Based on the simple configuration of the freestanding multimode waveguide, this sensor shows possibility of a fairly easy fabrication involving a single material and a a single process step.

Two types of MCWGs have been presented by Salamon et al and Zourob et al, the dip- and the peak-type MCWGs, however without any theoretical study of the sensors. We have shown that the basic principles of the sensor configurations are the same, they are both applicable for sensing purposes due to the excitation of waveguide modes in the waveguide film, however using different features for the sensing. Also, we have shown that the two operations of MCWG sensors depend on the metal used in the configuration. A dip-type MCWG is obtained by applying a metal with a low value of ϵ''_M and a peak-type MCWG is obtained by applying a metal with a large ϵ''_M, and

for a difference in the thickness of the metal cladding of about an order of magnitude for the two sensor types.

The sensor properties of the dip-MCWG can be optimized to achieve the largest shift in the reflectance dip relative to the FWHM of the dip. To achieve this, it is not sufficient to consider the usual sensitivity parameters (cover RI sensitivity and adlayer sensitivity), as these do not take the dip shape into account. Instead, our optimization procedure is based simply on Fresnell's reflection law for the four-layer structure (substrate-metal-film-cover) from which the dip-angle-change per dip-width to the change in cover-RI or adlayer thickness can be deduced directly.

If the dip shape is not taken into account, the surface-plasmon resonance (SPR) sensor (equivalent to MCWG sensor without dielectric film) generally exhibits the largest sensitivity, but taking into account the width of the dip, there is a clear benefit of applying a waveguide film on top of the metal layer, simply because of the much narrower waveguide dip. These benefits apply to both refractometry applications (cover RI detection) as well as adlayer detection.

With respect to adlayer detection, which is the most interesting for biosensing applications, the main experiences gained from our investigations of optimized sensitivity can be summarized as follows:

- The film RI should be as low as possible.
- The optimum film thickness is close to the mode's cutoff thickness.
- Silver cladding is preferable to gold-cladding, mainly due to a narrower dip.
- The optimum metal layer thickness does not depend on the film RI. For a light wavelength of 632.8 nm and optimum film thickness they are 56, 53, 44, and 40 nm for TM-silver, TM-gold, TE-silver, and TE-gold modes, respectively.
- The dependence on substrate RI is practically non-existing, because at optimum metal thicknesses the mode's evanescent field is vanishing in the substrate.
- As opposed to SPR detection, the dip-MCWG detection has the possibility of utilizing both TE and TM polarized light, however, the largest adlayer sensitivity is obtained for TE polarized light.
- For a film RI of 1.45 the sensitivity improvement compared with Ag-SPR sensing is approximately a factor of 6.

The dip-type MCWG can be tuned to obtain either a low or a high penetration depth by adjusting the film parameters and thus the sensor can be used for measurements on both thin adlayer and micronscale objects. The sensor can be operated in multimode operation or supporting both a TE- and TM-mode resulting in modes with different penetration depths in the cover, giving a

sensor that can measure at different depths in the cover medium. Thus the MCWG has the same advantages as the reverse symmetry dielectric waveguide. Contrary, for the SPR sensor it is not possible to tune the penetration depth, which basically is fixed to 160 nm over the whole detection range. The penetration depth of the SPR sensor does not change significantly when the metal is changed from gold to silver.

The peak-type MCWG has an infinite penetration depth of the evanescent field in the cover and can with advantage be used for broad range refractive index measurements, as the cover RI sensitivity is constant over the entire detection range for changes in n_C with a high cover RI sensitivity of 1 and a broad detection range. However, the sensor is not useful for thin adlayer measurements as the adlayer sensitivity is zero.

For actual measurements with the MCWG sensors the analysis of the experimental setup showed that only the angular interrogation setup is relevant for the peak-type MCWG. For the dip-type MCWG both the angular and the wavelength interrogation setup can be used and actually the wavelength setup indicates that the detection range can be expanded using this setup.

A retro reflector setup was build and analyzed for measurements with the MCWG sensors, where angular interrogation was used for both sensors. The setup simplifies normally used rotational setups and by analysis of the spot position of the prism/sensor interface it was shown that the setup can be used for precise measurements as basically the same area of the sensor is used over the rotation range.

Two MCWG sensors have been fabricated and applied for measurements using the retro reflector setup. RI-measurements and cell detection were performed, where the important deep-probe sensing application for detection of micronscale biological objects showed excellent results as a single cell on the sensor surface could be detected using either of the MCWG sensors, with detection limits well below 1 cell/mm^2.

RI measurements with the peak- and the dip-type MCWG sensors show a difference in cover RI sensitivity for the peak-type and dip-type MCWG sensor of approximately 40 % which corresponds nicely with the difference in calculated cover sensitivies of 35%.

Experiments for detection of cells settling on the sensor surface show that both the peak- and the dip-type MCWG sensor can be successfully applied for deep-probe sensing as a detection limit due to the signal-to-noise ratios of 0.2 cells/mm^2 is obtained for both sensors and thus direct detection of a single cell at the sensor surfaces is possible.

It should finally be noted that the MCWG offers an additional advantage to the SPR-device as the waveguide film provides a chemical and mechanical shield to the metal layer.

Bibliography

[1] I Abdel-Hamid, D Ivnitski, P Atanasov, and E Wilkins. Highly sensitive flow-injection immunoassay system for rapid detection of bacteria. *Anal. Chim. Acta*, 399:99–108, 1999.

[2] D. Ivnitski, I. Abdel-Hamid, P. Atanasov, and E. Wilkins. Review: Biosensors for detection of pathogenic bacteria. *Biosensors Bioelectron.*, 14:599–624, 1999.

[3] B.A. Forbes, D.F. Sahm, and A.S. Weissfeld. Diagnostic microbiology. *Mosby, Inc.*, 10th edition, 1998.

[4] Invitrogen Life Technologies. Product brochure for pcr and rt-pcr. *www.invitrogen.com*.

[5] J. Sperveslage, E. Stackebrandt, F.W. Lembke, and C. Koch. Detection of bacterial-contamination, including bacillus spores, in dry growth media and in milk by identification of their 16s rdna by polymerase chain-reaction. *J. Microbiol. Methods*, 26:219–224, 1996.

[6] J. Meng, S. Zhao, M.P. Doyle, S.E. Mitchell, and S. Kresovich. Polymerase chain reaction for detecting escherichia coli o157:h7. *Int. J. of Food Microbiology*, 32:103–113, 1996.

[7] C.A. Rowe-Taitt, J.W. Hazzard, K.E. Hoffman, J.J. Cras, J.P. Golden, and F.S. Ligler. Simultaneous detection of six biohazardous agents using a planar waveguide array biosensor. *Biosens. Bioelectronics*, 15:579–589, 2000.

[8] M.B. Medina. Binding of collagen i to escherichia coli o157:h7 and inhibition by carrageenans. *Int. J. of Food Microbiology*, 69:199–208, 2001.

[9] H.J. Watts, C.R. Lowe, and D.V. Pollardknight. Optical biosensor for monitoring microbial-cells. *Anal. Chem.*, 66:2465–2470, 1994.

[10] B.H. Schneider, J.G. Edwards, and N.F. Hartman. Hartman interferometer: versatile integrated optic sensor for label-free, real-time quantification of nucleic acids, proteins, and pathogens. *Clinical Chem.*, 43:1757–1763, 1997.

[11] A. Brandenburg and R. Henninger. Integrated optical young interferometer. *Appl. Opt.*, 25:5941–5947, 1994.

[12] R. G. Heideman, G. J. Veldhuis, E. W. H. Jager, and P. V. Lambeck. Fabrication and packaging of integrated chemo-optical sensors. *Sens. Actuators B*, 35–36:234–240, 1996.

[13] G. R. Quigley, R. D. Harris, and J. S. Wilkinson. Sensitivity enhancement og integrated optical sensors by use of thin high-index films. *Appl. Opt.*, 38:6036–6039, 1999.

[14] Ch. Stamm, R. Dangel, and W. Lukosz. Biosensing with the integrated-optical difference interferometer: dual-wavelength operation. *Opt. Commun.*, 153:347–359, 1998.

[15] B. Maisenhölder, H. P. Zappe, R. E. Kunz, P. Riel, M. Moser, and J. Edlinger. A gaas/algaas-based refractometer platform for integrated optical sensing applications. *Sens. Actuators B*, 38–39:324–329, 1997.

[16] W. Lukosz, Ch. Stamm, H. R. Moser, R. Ryf, and J. Dübendorfer. Difference interferometer with new phase-measurement method as integrated-optical refractometer, humidity sensor and biosensor. *Sens. Actuators B*, 38–39:316–323, 1997.

[17] Th. Schubert, N. Haase, H. Hück, and R. Gottfried-Gottfried. Refractive-index measurements using an integrated mach-zehnder interferometer. *Sens. Actuators A*, 60:108–112, 1997.

[18] P.K.Tien. Integrated optics and new wave phenomena in optical waveguides. *Rev. Mod. Phys*, 49:361–420, 1977.

[19] K.Tiefenthaler and W.Lukosz. Sensitivity of grating couplers as integrated-optical chemical sensors. *J. Opt. Soc. AM. B*, 6:209–220, 1989.

[20] K. Tiefenthaler and W. Lukosz. Integrated optical switches and gas sensors. *Opt. Lett.*, 10:137–139, 1984.

[21] H. Kogelnik and H.P. Weber. Rays, stored energy, and power flow in dielectric waveguides. *J. Opt. Society of america*, 64:174–185, 1974.

[22] R. Cush, J.M. Cronin, W.J. Stewart, C.H. Maule, J. Molloy, and N.J. Goddard. The resonant mirror: a novel optical biosensor for direct sensing of biomolecular interactions part i: Principle of operation and associated instrumentation. *Biosens. Bioelectronics*, 8:347–354, 1993.

[23] P.E. Buckle, R.J. Davies, T. Kinning, D. Yeung, P.R. Edwards, D. Pollard-Knight, and C.R. Lowe. The resonant mirror: a novel optical biosensor for direct sensing of biomolecular interactions part ii: Applications. *Biosens. Bioelectronics*, 8:355–363, 1993.

[24] W. Lukosz. Integrated optical chemical and direct biochemical sensors. *Sens. Actuators B*, 29:37–50, 1995.

[25] R.E. Kunz. Miniature integrated optical modules for chemical and biochemical sensing. *Sens. Actuators B*, 38–39:13–28, 1997.

[26] Zm. Qi, N. Matsuda, K. Itoh, M. Murabayashi, and C.R. Lavers. A design for improving the sensitivity of a mach-zehnder interferometer to chemical and biological measurands. *Sens. Actuators B*, 81:254–258, 2002.

[27] M. Zourob, S. Mohr, B.J.T. Brown, P.R. Fielden, M. McDonnell, and N.J. Goddard. The development of a metal clad waveguide sensor for the detection of particles. *Sens. Actuators B*, 90:296–307, 2003.

[28] M. Zourob, S. Mohr, P.R. Fielden, and N.J. Goddard. Small-volume refractive index and fluorescence sensor for micro total analytical system (μ-tas) applications. *Sens. Actuators B*, 94:304–312, 2003.

[29] R. Horváth, L.R. Lindvold, and N.B. Larsen. Fabrication of all-polymer freestanding waveguides. *J. Micromech. Microeng.*, 13:419–424, 2003.

[30] R. Kurrat. Adsorption of biomolecules on titanium oxide layers in biological model solutions. *PhD dissertation no 12891*, ETH Zurich, 1998.

[31] W. Lukosz and K. Tiefenthaler. Embossing technique for fabricating integrated optical-components in hard inorganic waveguiding materials. *Opt. Lett.*, 8:537–539, 1983.

[32] W. Lukosz, Ph.M. Nellen, Ch. Stamm, and P. Weiss. Output grating ouplers on planar waveguides as integrated optical chemical sensors. *Sens. Actuators B*, 1:585–588, 1990.

[33] Ph.M. Nellen and W. Lukosz. Integrated optical input grating couplers as chemo- and immunosensors. *Sens. Actuators B*, 1:592–596, 1990.

[34] HU MicroVacuum, Budapest. Ow 2400 sensor chip, owls sensor system. *www.microvacuum.com*.

[35] H. Raether. Surface plasma oscillations and their applications. *Physics of thin films*, 9:145–261, Academic, New York, 1977.

[36] B. Liedberg, C. Nylander, and I. Lundström. Surface plasmon resonance for gas detection and biosensning. *Sens. Actuators B*, 4:299–304, 1983.

[37] P.I. Nikitin, A.A. Beloglazov, M.V. Valeiko, J.A. Creighton, A.M. Smith, N.A.J.M. Sommerdijk, and J.D. Wright. Silicin-based surface plasmon resonance chemical sensors. *Sens. Actuators B*, 38–39:53–57, 1997.

[38] L. Lévesque and B.E. Paton. Detection of defects in multiple-layer structures by using surface plasmon resonance. *Appl. Optics*, 36:7199–7203, 1997.

[39] T. Akimoto, S. Sasaki, K. Ikebukuro, and I. Karube. Effect of incident angle of light on sensitivity and detection limit for layers af antibody with surface plasmon resonance spectroscopy. *Biosens. Bioelectronics*, 15:355–362, 2000.

[40] R.J. Green, R.A. Frazier, K.M. Shakesheff, M.C. Davies, C.J. Roberts, and S.J.B. Tendler. Review: Surface plasmon resonance analysis of dynamic biological interactions with biomaterials. *Biomaterials*, 21:1823–1835, 2000.

[41] Sweden Biacore International AB.

[42] N.J. Goddard, D. Pollard-Knight, and C.H. Maule. Real-time biomolecular interaction analysis using the resonant mirror sensor. *Analyst*, 119:583–588, 1994.

[43] N.J. Goddard, J. Hulme, C. Malins, K. Singh, and P.R. Fielden. Asymmetric anti-resonant reflecting optical waveguides (arrow) as chemical sensors. *Analyst*, 127:378–382, 2002.

[44] F. prieto, L.M. Lechuga, A. Calle, A. Llobera, and C. Dominguez. Optimized silicon antiresonant reflecting optical waveguides for sensing applications. *J. Lightwave tech.*, 19:75–83, 2001.

[45] R. Bernini, S. Campopiano, L. Zeni, and P.M. Sarro. Arrow optical waveguides based sensors. *Sens. Actuators*, 100:143–146, 2004.

[46] S. Sainov, V. Sainov, and G. Stoilov. Interferometer based on total internal reflection. *Appl. optics*, 34:2848–2852, 1995.

[47] A. Klotz, A. Brecht, and G. Gauglitz. Channel waveguide mode beat inteferometer. *Sens. Actuators B*, 38–39:310–315, 1997.

[48] A.V. Kabashin and P.I. Nikitin. Surface plasmon resonance interferometer for bio- and chemical-sensors. *Opt. Comm.*, 150:5–8, 1998.

[49] Farfield Sensors Ltd Manchester UK Farfield Sesnors Ltd., UK. Analight® bio200 sensor system. *www.farfield-sensors.co.uk*.

[50] R. Horváth, G. Fricsovszky, and E. Papp. Application of the optical waveguide lightmode spectroscopy to monitor lipid bilayer phase transition. *Biosens. Bioelectron.*, 18:415–428, 2003.

[51] DuPont.

[52] R. Horváth, L.R. Lindvold, and N.B. Larsen. Reverse-symmetry waveguides: Theory and fabrication. *Appl. Phys. B*, 74:383–393, 202.

[53] R. Horváth, H.C. Pedersen, and N.B. Larsen. Demonstration of reverse symmetry waveguide sensing in aqueous solutions. *App. Phys. Lett.*, 81:2166–2168, 2002.

[54] Z.M. Qi, N. Matsuda, J.H. Santos, A. Takatsu, and K. Kato. Prism-coupled multimode waveguide refractometer. *Opt. lett.*, 27:689–691, 2002.

[55] Robert C. Weast. Handbook of chemistry and physics. *CRC press, Inc., Florida*.

[56] G. Tollin Z. Salamon. Optical anisotropy in lipid bilayer membranes: Coupled plasmon-waveguide resonance measurements of molecular orientation, polarizability, and shape. *Biophys. J.*, 80:1557–1567, 2001.

[57] Z. Salamon, H.A. Macleod, and G. Tollin. Coupled plasmon-waveguide resonators: A new spectroscopic tool for probing proteolipid film structure and properties. *Biophys. J.*, 73:2791–2797, 1997.

[58] Z. Salamon and G. Tollin. Optical anisotropy in lipid bilayer membranes: coupled plasmon-waveguide resonance measurements of molecular orientation, polarizability, and shape. *Biophys. J.*, 80:1557–1567, 2001.

[59] Z. Salamon, D. Huang, W.A. Cramer, and G. Tollin. Coupled plasmon-waveguide resonance spectroscopy studies of the cytochrome b(6)f/plastocyanin system in supported lipid bilayer membranes. 75:1874–1885, 1998.

[60] Z. Salamon, M.I. Brown, and G. Tollin. Plasmon resonance spectroscopy: probing molecular interactions within membranes. *TIBS*, 24:213–219, 1999.

[61] Z. Salamon, G. Lindblom, L. Rilfors, K. Linde, and G. Tollin. Interaction of phosphatidylserine synthase from e-coli with lipid bilayers: Coupled plasmon-waveguide resonance spectroscopy studies. *Biophys. J.*, 78:1400–1412, 2000.

[62] Z. Salamon, G. Lindblom, and G. Tollin. Plasmon-waveguide resonance and impedance spectroscopy studies of the interaction between penetratin and supported lipid bilayer membranes. *Biophys. J*, 84:1796–1807, 2003.

[63] Z. Salamon and G. Tollin. Graphical analysis of mass and anisotropy changes observed by plasmon-waveguide resonance spectroscopy can provide useful insights into membrane protein function. *Biophys. J.*, 86.

[64] Z. Salamon, S. Cowell, E. Varga, H.I. Yamamura, V.J. Hruby, and G. Tollin. Plasmon resonance studies of agonist/antagonist binding to the human delta-opioid receptor: New structural insights into receptor-ligand interactions. *Biophys. J.*, 79:2463–2474, 2000.

[65] Z. Salamon, V.J. Hruby, G. Tollin, and S. Cowell. Binding of agonists, antagonists and inverse agonists to the human delta-opioid receptor produces distinctly different conformational states distinguishable by plasmon-waveguide resonance spectroscopy. *J. peptide Research*, 60, 2002.

[66] I.D. Alves, Z. Salamon, E. Varga, H.I. Yamamura, G. Tollin, and V.J. Hruby. Direct observation of g-protein binding to the human delta-opioid receptor using plasmon-waveguide resonance spectroscopy. *J. Biol. Chem.*, 278:48890–48897, 2003.

[67] S. Devanathan, Z.P. Yao, Z. Salamon, B. Kobilka, and G. Tollin. Plasmon-waveguide resonance studies of ligand binding to the human beta(2)-adrenergic receptor. *Biochemistry*, 43, 2004.

[68] G. Tollin, Z. Salamon, and V.J. Hruby. Techniques: Plasmon-waveguide resonance (pwr) spectroscopy as a tool to study ligand-gpcr interactions. *Trends in pharmacological sciences*.

[69] M. Born and E. Wolf. Principles of optics, electromagnetic theory of propagation, interference and diffraction of light. *Cambridge university press*, 7th edition:65, ISBN:0 521 642221.

[70] A. Otto and W. Sohler. Modification of the total reflection modes in a dielectric film by one metal boundary. *Opt. Commun.*, 3:254–258, 1971.

[71] M. Zourob and N.J. Goddard. Metal clad leaky waveguides for chemical and biosensing applications. *Biosens. Boielectronics*, 20:1718–1727, 2005.

[72] M. Zourob, S. Mohr, B.J.T. Brown, P.R. Fielden, M.B. McDonnell, and N.J. Goddard. An integrated metal clad leaky waveguide sensor for detection of bacteria. *Anal. Chemisty*, 77:232–242, 2005.

[73] Denmark Polyteknik.

[74] F. Fixe, M. Dufva, P. Telleman, and C.B.V. Christensen. Functionalization of poly(methyl methacrylate) (pmma) as a substrate for dna microarrays. *Nucleic Acids Res.*, 20:1679–1684, 1992.

[75] E.H. Ko and J. Suh. Artificial metalloproteases with broad substrate selectivity constructed on polystyrene. *Bull. Korean Chem. Soc.*, 25:1917–1923, 2004.

[76] R.A. Innes and J.R. Sambles. Optical characterisation of gold using surface plasmon-polaritons. *J. Phys. F: Met. Phys*, 17:277–287, 1987.

[77] K. Welford. Tutorial review: Surface plasmon-polaritons and the uses. *Opt. Quant. Electronics*, 23:1–27, 1991.

Mission

To promote an innovative and environmentally sustainable technological development within the areas of energy, industrial technology and bioproduction through research, innovation and advisory services.

Vision

Risø's research **shall extend the boundaries** for the understanding of nature's processes and interactions right down to the molecular nanoscale.

The results obtained shall **set new trends** for the development of sustainable technologies within the fields of energy, industrial technology and biotechnology.

The efforts made **shall benefit** Danish society and lead to the development of new multi-billion industries.